Cosmological Tests of Gravity with MGCAMB

by

Zhuangfei Wang

B.Sc., Peking University, 2019

Thesis Submitted in Partial Fulfillment of the
Requirements for the Degree of
Doctor of Philosophy

in the
Department of Physics
Faculty of Science

© Zhuangfei Wang 2024
SIMON FRASER UNIVERSITY
Summer 2024

Declaration of Committee

Name: **Zhuangfei Wang**

Degree: **Doctor of Philosophy**

Thesis title: **Cosmological Tests of Gravity with MGCAMB**

Committee: **Chair:** Levon Pogosian
Professor, Physics

Levon Pogosian
Supervisor
Professor, Physics

Andrei Frolov
Committee Member
Professor, Physics

Gopolang Mohlabeng
Committee Member
Assistant Professor, Physics

Malcolm Kennett
Examiner
Professor, Physics

Eleonora Di Valentino
External Examiner
Research Fellow, Mathematical and Physical Sciences
The University of Sheffield

Abstract

The discovery of the cosmic acceleration, along with the old cosmological constant problem and the still-unknown nature of dark matter, stimulated exploration of alternate theories of gravity. The interest in testing general relativity (GR) on cosmological scales is further fuelled by the opportunities offered by existing and forthcoming cosmological surveys. This thesis presents several original contributions to the actively developing area of cosmological tests of gravity.

First, we present a new version of Modified Growth with `CAMB` (`MGCAMB`), a widely used numerical tool for cosmological tests of gravity. New features include a parameterization allowing for a simultaneous reconstruction of phenomenological functions characterizing departures from the background expansion and departures in the linear growth of cosmic structures from the ΛCDM prediction. Other new features include the option to test models with a scalar field coupled only to dark matter, and the option to include dark energy perturbations when working with alternative background expansion histories. This version of MGCAMB comes with a Python wrapper to run it directly from the Python interface, making it easy to use with commonly used Monte-Carlo Markov Chain samplers.

Next, we show how cosmological observations could distinguish between a modification of gravity and additional dark matter interactions - a question that has not been quantitatively investigated before. We demonstrate that data from a next generation survey, such as the Square Kilometer Array, will make it possible to distinguish between the two possibilities through measurements of gravitational redshift.

Finally, we extend the framework in `MGCAMB` with a phenomenological model that can capture the nonlinear evolution of cosmic structures in a broad range of modified gravity theories. The extension employs the halo model reaction code `ReACT` used for modeling the nonlinear corrections in extensions of the ΛCDM model. We demonstrate that using this extension allows one to derive stronger constraints on modified gravity from the existing Dark Energy Survey data. The nonlinear extension will be of particular importance for the next generation of high resolution surveys such as Euclid and the Large Synoptic Survey Telescope.

List of Papers

The findings and results presented in this thesis are based on these works:

1. Zhuangfei Wang, Seyed Hamidreza Mirpoorian, Levon Pogosian, Alessandra Silvestri, and Gong-Bo Zhao, *New MGCAMB tests of gravity with CosmoMC and Cobaya*, JCAP, 08:038, 2023. Chapter 3 of the thesis is based on this publication. I contributed to the modelling of the CDM-only coupling model, implemented new models and features in the new code version `MGCAMB 2023`, upgraded MCMC sampler `MGCosmoMC` to the latest version of `CosmoMC`, wrote MCMC tool MGCobaya, and conducted the corresponding MCMC analyses on representative models as demonstrations.

2. Sveva Castello, Zhuangfei Wang, Lawrence Dam, Camille Bonvin, Levon Pogosian, *Disentangling modified gravity from a dark force with gravitational redshift*, arXiv:2404.09379 [astro-ph.CO]. Chapter 4 of the thesis is based on this paper. I completed the joint modelling of coupled quintessence (CQ) and Generalized Brans-Dicke (GBD) in `MGCAMB`, and generated modified power spectrum as the input for the calculation of correlation function multipoles. I also performed the MCMC analyses to disentangle CQ from GBD for some representative fiducial cases.

3. Zhuangfei Wang, Daniela Saadeh, Kazuya Koyama, Levon Pogosian, Benjamin Bose, Lanyang Yi, and Gong-Bo Zhao, *Extending MGCAMB tests of gravity to nonlinear scales*, arXiv:2406.09204 [astro-ph.CO]. Chapter 5 of the thesis is based on this paper. I upgraded the `MGCAMB` code by introducing the nonlinear extension for modified gravity theories, with the help of halo model reaction function. I also demonstrated the effect of the nonlinear extension by conducting MCMC analyses with `MGCobaya`.

4. Seyed Hamidreza Mirpoorian, Zhuangfei Wang, and Levon Pogosian, *On validity of the quasi-static approximation in scalar-tensor theories*, JCAP, 07:069, 2023. This publication is referenced in part of Chapter 3. I co-developed the formulation of the Einstein's equations and evolution equations of for scalar tensor theories, in both quasi-static approximation (QSA) and exact case.

Dedication

This thesis is dedicated to all my family, especially my parents, for their enduring love and unconditional support throughout my PhD journey.

Acknowledgements

I would like to express my heartfelt gratitude to my senior supervisor Levon Pogosian. He has been exceptionally supportive, understanding, and always helpful to me throughout my five years of PhD study.

I would also like to thank all my colleagues, for their helpful discussions and wonderful inspirations in science and work. Special thanks to all my friends I have made since coming to Canada, for their kind support and help in my everyday life.

Table of Contents

List of Tables

List of Figures

Chapter 1

Introduction

The study of modern cosmology, which experienced several decades of rapid growth following the breakthrough observations of cosmic microwave background (CMB) anisotropies by COBE satellite, is in the midst of a new golden era. The revolutionary discovery of gravitational waves (GW) from black hole binaries by the The Laser Interferometer Gravitational-Wave Observatory (LIGO) Collaboration in 2015 [1], followed by detection of GWs from a neutron star merger in 2017, ushered a new era of multi-messenger astronomy. Along with James Webb Space Telescope (JWST)[1] and a number of ongoing and forthcoming large scale cosmological surveys, such as the Dark Energy Survey (DES)[2], the Dark Energy Spectroscopic Instrument (DESI)[3] and the Large Synoptic Survey Telescope (LSST)[4], they are offering new opportunities for testing our cosmological model and searching for signatures of new physics.

The current cosmological model assumes co-existence of non-interacting cold dark matter (CDM) and normal matter, as well as a positive cosmological constant Λ that plays the role of dark energy (DE) responsible for the acceleration of the cosmic expansion first discovered from observations of Type Ia supernovae in 1998 [2]. While the ΛCDM model survived nearly three decades of intense scrutiny, and, overall, provides a good fit to the available cosmological data, it is seen as a placeholder model until the nature of DE and CDM is understood. Of particular concern is the "old" cosmological constant (CC) problem [3, 4] which refers to the so far unsuccessful attempts to explain why most of the vacuum energy density predicted by quantum field theory (QFT) does not seem to gravitate. The CC

---

[1]https://webb.nasa.gov/

[2]https://www.darkenergysurvey.org/

[3]https://www.desi.lbl.gov/

[4]https://www.lsst.org/

problem[5], coupled with the discovery of cosmic acceleration, are the primary motivations for exploring alternative theories of gravity and DE. Adding to this motivation is the yet unknown nature of dark matter.

In addition to the open questions about the physical nature of the two dark components, certain tensions between datasets, when interpreted in the context of the ΛCDM model, have emerged in recent years [5]. The most significant of them is the so-called Hubble tension, which is the disagreement between the value of the Hubble parameter measured "directly" by studying the rate at which distant galaxies are moving away from us, and the value predicted by the ΛCDM model with parameters that best fit the CMB observations. Such tensions could still be caused by yet unknown systematic errors, but could also be pointing to a potential missing ingredient in the cosmological model. Attempts to resolve the tensions also motivated significant work on theories of modified gravity, dark energy and interacting dark sectors.

1.1 Cosmological tests of gravity and MGCAMB

The field of cosmological tests of modified gravity has matured significantly over the past couple of decades. Studies evolved from the phenomenology of specific models, such as $f(R)$ [6, 7, 8, 9] and Dvali-Gabadadze-Porrati (DGP) [10, 11], to the development of general frameworks [12, 13, 14, 15, 16, 17, 18, 19] for studying broad classes of modified gravity theories, such as Horndeski [20, 21] and beyond [22, 23, 24, 25], along with the numerical tools for interpreting observations within these frameworks, such as `EFTCAMB` [26, 27, 28] and `hi_class` [29, 30].

Modified Growth with `CAMB` (`MGCAMB`), first introduced in 2008 [31] and significantly upgraded in 2011 [32], 2019 [33] and 2023 [34], is a patch for the popular Einstein-Boltzmann solver `CAMB` [35, 36], allowing one to compute cosmological observables in models with modified relations between the gravitational metric potentials and the matter density contrast. It has been used in conjunction with Monte-Carlo Markov Chain (MCMC) samplers, such as `CosmoMC` [37, 38] and `Cobaya` [37, 39, 40] to constrain modifications of gravity on cosmological scales [41, 42, 43].

The essential difference between `MGCAMB` (and similar software, like `MGCLASS` [44] and `ISiTGR` [45, 46, 47]) and codes like `EFTCAMB` and `hi_class` is that the latter are exact tools for testing scalar-tensor theories, albeit of most general type, while the former are purely phenomenological, helping constrain departures from GR that are more directly probed by large-scale structure surveys. In practice, one always has to choose a particular

---

[5]The "old" CC problem concerns the technically unnatural fine-tuning of Λ needed to cancel out the huge energy in the vacuum. The "new" CC problem, also known as the coincidence problem, appeared after the discovery of cosmic acceleration and asks why the constant DE density happens to be of the same order as the current matter density of the Universe.

parameterization and such choices are often driven by intuition gained from scalar-tensor theories. Thus, there is a good degree of synergy between theory-specific tools and `MGCAMB` when it comes to obtaining theoretical priors [48] on the phenomenological variables and the interpretation of the constraints [49]. A recent example of such a synergistic approach was the joint reconstruction [50, 51] of the two `MGCAMB` functions, μ and Σ, parameterizing the relations between the matter density contrast and the Newtonian and Weyl potentials, respectively, and the dark energy (DE) density fraction, Ω_X, with the help of a correlation prior derived from scalar-tensor theories.

1.2 Distinguishing a dark matter interaction from a modification of gravity

In the standard cosmological model, dark matter takes the form of a slow-moving ("cold"), non-interacting, non-baryonic species. Since such a particle has not been detected yet, several extensions to the simple CDM paradigm have been proposed. These include scenarios where dark matter interacts weakly with particles of the Standard Model [52, 53], with the dark sector (e.g. dark radiation) [54, 55], or through self-interactions via a fifth (non-gravitational) force [56, 57, 58, 59].

To test for gravity modifications and dark matter interactions, the standard approach is to employ measurements of the growth rate of cosmic structure obtained through redshift-space distortions (RSD) (see e.g. Refs. [60, 61, 62, 63]). Since gravity governs the way cosmic structure evolves with time, deviations from GR generically modify the growth rate, which is achieved by involving a deviation in the Poisson equation and thus affecting the evolution of all cosmic components. Similarly, the growth rate would also be affected by any new force acting on the dark matter particles, namely, a fifth force would only modify the Euler equation for dark matter, as this would have an impact on structure formation. Current analyses are testing these two scenarios separately. The community working on gravity modifications usually assumes that dark matter is a cold non-interacting particle and uses the growth rate of structure to test theories beyond GR, see e.g. Ref. [64]. By contrast, the community working on non-standard dark matter models typically assumes the validity of GR and uses the growth rate to constrain the strength of dark matter interactions [65, 66, 67]. As we do not know which scenario (if any) is correct, it is important to ask whether it is possible to test for both kinds of modifications at the same time and disentangle them from one another.

1.3 Extending cosmological tests of gravity to nonlinear scales

Until now, the parameterization in `MGCAMB` can only be used to constrain departures of the evolution of cosmological perturbations from GR within the range of validity of linear

perturbation theory. On the other hand, a significant portion of the information contained in the data from large scale structure (LSS) surveys is in the correlations over scales $\lesssim 10$ Mpc, where the growth of cosmic structures turns nonlinear [68, 69, 70, 71]. While in the Λ Cold Dark Matter (ΛCDM) model the nonlinear corrections can be accurately calculated using the Halofit model [72, 73], with the latest version of `CAMB` adopting HMcode 2020 [74], Halofit cannot be used for MG models. Due to this limitation, when using `MGCAMB` with Cobaya or CosmoMC, a linear cut was required to remove the part of the data that could not be reliably modelled by linear theory [33]. In this thesis, we overcome this limitation by adding to `MGCAMB` a capability to compute observables on nonlinear scales.

1.4 Overview of the thesis

The aim of this thesis is to employ the computational tool `MGCAMB` to do cosmological tests of gravity in order to explore some new scenarios in modified gravity theories as well as the particular properties of dark matter introduced by the existence of a fifth force, with the help of new models and features in the code. The thesis is organized as follows. In Chapter 2, we will generally review the framework of the standard cosmological model in the presence of the Friedmann-Lemaître-Robertson-Walker (FLRW) universe. Specifically, we will start by showing how the isotropic and homogeneous universe on large scales is governed by GR in detail, and also discuss the framework of linear pertubation theory, and how different matter components evolve along with the cosmic background acceleration. We then introduce some major cosmological observables that are commonly used in modern studies of large scale structure in cosmology before making the extension to modified gravity theories, where their phenomenological signature is nicely interpreted with the help of `MGCAMB`.

In Chapter 3, we present a new version of `MGCAMB` (2023) as an upgrade. The added features include new models, such as a scalar field coupled only to dark matter in the quasi-static approximation, the option to include DE perturbations when working with $w \neq -1$ backgrounds, and a new binned parameterization allowing for a simultaneous reconstruction of μ, Σ and Ω_X as functions of redshift. We will describe all new features in detail and demonstrate their use in a few representative examples in this chapter.

In Chapter 4, we employ `MGCAMB` to produce synthetic data of redshift space distortions (RSD) with the gravitational redshift based on the specifications of Square Kilometer Array Phase 2 (SKA2), along with the weak gravitational lensing (WL) and Cosmic Microwave Background (CMB) data, based on which we perform a MCMC analysis to successfully break the degeneracy between modified gravity model and dark fifth force, with the generalized Brans-Dicke (GBD) type symmetron, and the symmetron form of coupled quintessence (CQ) as the representative examples implemented in `MGCAMB`, respectively. We also demonstrate the range of validity of the disentanglement between the two models by varing the coupling

strength of the symmetron model, and also the Compton wavelength, *i.e.* the scales of the modification effects.

In [75, 76, 77], a halo-model-based approach for modelling the effect of nonlinearities in modified gravity theories, *the halo model reaction* (HMR), was introduced and used to test DGP and $f(R)$ gravity models at percent-level accuracy. The HMR approach was also compared to N-body simulations in phenomenological extensions of GR in [78, 79] showing good agreement. Recently, HMR was applied in the Stage-IV cosmic shear forecast study [80] that adopted the linear parametrization of MG proposed in [81, 82, 83]. However, until now, the HMR approach has not been applied to cosmological tests of gravity using the μ-Σ parametrization used, for example, in the DES analysis [43]. In Chapter 5, we implement the HMR as an option in `MGCAMB`, making it possible to use LSS data on nonlinear scales. As we show, this results in stronger constraints on μ and Σ even after marginalizing over the additional HMR parameters.

Chapter 2

Cosmological Observables

In this chapter, we introduce the relevant components of the standard model of cosmology in the framework of GR and the main cosmological observables extracted from the data from cosmological surveys and commonly used for testing gravity. We also describe the framework for testing alternative gravity models in the framework of `MGCAMB`.

2.1 Friedmann-Lemaître-Robertson-Walker Cosmology

In the standard model of cosmology, the Friedmann-Lemaître-Robertson-Walker (FLRW) metric establishes the fundamental geometry of an isotropic, homogeneous and expanding universe. Specifically, the invariant line element ds in a FLRW universe can be written in spherical coordinates as

$$ds^2 = a(\tau)^2 \left[-d\tau^2 + \frac{dr^2}{1 - \tilde{k}r^2} + r^2 d\Omega^2 \right], \tag{2.1}$$

where $d\Omega^2 = d\theta^2 + \sin^2\theta\, d\phi^2$, $\tilde{k}$ is the spatial curvature constant, which is taken to belong to the set $\{-1, 0, +1\}$, corresponding to a open, flat, or closed universe, respectively, $a(\tau)$ is the scale factor, and τ is the conformal time, which is related to the physical time t via: $d\tau = dt/a(t)$. Also we use the unit of $c = 1$.

In the work presented in this thesis, we will assume a flat spacetime, with $\tilde{k} = 0$, since it is observationally favoured and is also predicted by inflation, which is the leading paradigm for setting the initial conditions in the early universe. Therefore, we will work with a flat FLRW metric in which the line element is

$$ds^2 = a^2(\tau) \left[-d\tau^2 + dx^i dx_i \right]. \tag{2.2}$$

In addition to the background evolution, we will be interested in the dynamics of small perturbations that describe the large-scale structure in the universe. The choice of the coordinates when perturbing the metric around the FLRW background is not unique, and

6

the value of the perturbations in a given physical quantity, such as the matter density or the metric, will in general be different in different coordinate system. For example, one could choose the time coordinate to be associated with the hypersurface of constant dark matter density. In that frame, the dark matter perturbation would vanish. While this example may not be very practical, as the equations for the other variables would become rather complicated, eliminating the freedom to change the perturbations through a coordinate transformation, or "fixing the gauge", is a necessity as not doing so can lead to unphysical solutions. In practice, the gauge is fixed by setting certain variables, or their combinations, to zero.

The perturbed FLRW metric can be written as

$$g_{\mu\nu} = a^2(\gamma_{\mu\nu} + h_{\mu\nu}), \tag{2.3}$$

where $a^2\gamma_{\mu\nu}$ is the background metric and $a^2 h_{\mu\nu}$ is the perturbation. The tensor $h_{\mu\nu}$ can be decomposed into scalar, vector, and vector modes. A "scalar mode" perturbation is characterized by a scalar function or a gradient of a scalar function. "Vector modes" and "tensor modes" are, respectively, perturbations that are constructed out of divergence-free vectors and divergence- and trace-free tensors, respectively. In this thesis, we will only be interested in scalar mode perturbations.

In Fourier space, for a given Fourier mode k, a general scalar mode perturbation can be written as [84, 85]

$$h_{00} = -2A, \ h_{0i} = -B\hat{k}_i, \ h_{ij} = 2H_L\delta_{ij} + 2H_T\left(-\hat{k}_i\hat{k}_j + \frac{1}{3}\delta_{ij}\right), \tag{2.4}$$

where $\hat{\mathbf{k}} = \mathbf{k}/k$ and A, B, H_L and H_T are scalar functions of k and τ.

One can set two out of these four functions to zero by a coordinate transformation. To see how this happens, consider an infinitesimal change of coordinates as follows,

$$x^\mu \to \tilde{x}^\mu = x^\mu + \xi^\mu(x^\alpha), \tag{2.5}$$

where $\xi^\mu = (\xi^0, \xi^i)$ is an infinitesimally small parameter. A physical property, represented by a scalar quantity $\Gamma(x^\mu)$, should have the same value in any coordinate system, including $\tilde{x}^\mu$, such that $\Gamma(x^\mu) = \tilde{\Gamma}(\tilde{x}^\mu)$. Propagating the perturbation to linear order, one can write:

$$\Gamma(x^\mu) = \Gamma^0(\tau) + \delta\Gamma(x^\mu), \quad \tilde{\Gamma}(\tilde{x}^\mu) = \Gamma^0(\tilde{\tau}) + \delta\tilde{\Gamma}(\tilde{x}^\mu). \tag{2.6}$$

Considering the coordinate transformation, we have:

$$\tilde{\Gamma}(\tilde{x}^\mu) = \Gamma^0(\tau) + \frac{d\Gamma^0}{d\tau}\xi^0 + \delta\Gamma(x^\mu) + \xi^\mu\partial_\mu\Gamma^0(\tau), \tag{2.7}$$

where the last term on the right side is $O(2)$ and can be omitted at linear order. Hence, the perturbation transforms as:

$$\delta\tilde{\Gamma} = \delta\Gamma - \frac{d\Gamma^0}{d\tau}\xi^0 \ . \tag{2.8}$$

One can then choose a ξ^0 to make $\delta\tilde{\Gamma} = 0$. Additionally, the spatial components of ξ^μ have a gradient-free (vector mode) and curl-free (scalar mode) parts,

$$\xi^i = \xi^i_v + \delta^{ij}\nabla_j\xi, \tag{2.9}$$

where ξ is another scalar degree of freedom that one can use to set another function to zero. One can use these two scalar coordinate transformations to set two of the four "scalar mode" metric perturbations to zero.

Two commonly used gauges are the conformal Newtonian gauge and the synchronous gauge. In the conformal Newtonian gauge, $B = H_T = 0$, $A = \Psi$, $H_L = -\Phi$, where Ψ and Φ are the Newtonian gravitational potentials. The standard Boltzmann codes, such as `CAMB`, are developed in the synchronous gauge, where $A = B = 0$, $H_L = h/6$, and $H_T = -3(\eta + h/6)$, in which we define scalar potentials h and η to be consistent with the notation of Ma and Bertschinger [86] used in `CAMB`.

The synchronous gauge does not completely fix the gauge, making the solution of the system of perturbations not unique. A convenient way to fix the residual gauge freedom is to set the CDM velocity to zero, since CDM only evolves under the influence of gravity and is not directly observable.

While the equations and variables used to evolve linear cosmological perturbations depend on the gauge choice, cosmologists ultimately use theory to make predictions for quantities that are observable. Such observable quantities are gauge-independent.

Within GR, the gravitational interactions between the relativistic and non-relativistic particles are achieved through the response to the geometrical curvature of the spacetime, and the dynamics of spacetime is prescribed by the following Einstein-Hilbert action [87],

$$S_{\rm EH} = \int {\rm d}^4x\sqrt{-g}\left\{\left[\frac{1}{16\pi G}(\mathcal{R} - 2\Lambda)\right] + \mathcal{L}_{\rm m}\left(\psi_{\rm m}, g_{\mu\nu}\right)\right\} \tag{2.10}$$

where $\mathcal{R}$ is the Ricci scalar, G is the gravitational constant, Λ is the cosmological constant that plays the role of DE in the ΛCDM model, and $\mathcal{L}_{\rm m}\left(\psi_{\rm m}, g_{\mu\nu}\right)$ is the matter component of the Lagrangian density, which includes CDM, baryons, photons and neutrinos. One then varies $S_{\rm EH}$ with respect to $g_{\mu\nu}$, and uses the principle of least action, *i.e.* $\delta S_{\rm EH}/\delta g_{\mu\nu} = 0$, to derive the dynamical equation for the metric, known as the Einstein's equation,

$$G_{\mu\nu} = \mathcal{R}_{\mu\nu} - \frac{1}{2}g_{\mu\nu}\mathcal{R} = 8\pi G T_{\mu\nu} \ , \tag{2.11}$$

where $G_{\mu\nu}$ is called the Einstein tensor, $\mathcal{R}_{\mu\nu}$ is the Ricci tensor, and the $T_{\mu\nu}$ on the right side of the Eq. (2.11) is the energy-momentum tensor for all components of particle fluids, which takes the form of:

$$T_{\mu\nu} = (\rho + P)u_\mu u_\nu - P g_{\mu\nu} \tag{2.12}$$

where $u_\mu = dx^\mu/(-ds^2)^{1/2}$ is defined as the four-velocity of the particle fluid, P is the pressure and ρ is the density of matter and energy. In particular, the perturbation of each component in the energy-momentum tensor $\delta T^\mu{}_\nu$ is given by: [86]

$$\delta T^0{}_0 = -\delta\rho, \tag{2.13}$$

$$\delta T^0{}_i = (\rho + P)v_i, \tag{2.14}$$

$$\delta T^i{}_j = \delta P \delta^i{}_j + \Sigma^i{}_j, \tag{2.15}$$

where $\Sigma^i{}_j$ is defined as the anisotropic shear pertubation, with $\Sigma^i{}_i = 0$. Conventionally, we can also define the perturbation quantities θ as the velocity divergence of each matter species, $\theta = \partial^j v_j$, and σ as the anisotropic stress, based on the (ij) component of $\delta T^\mu{}_\nu$, as given by:

$$(\rho + P)\sigma = -(\hat{k}_i \hat{k}_j - \frac{1}{3}\delta_{ij})\Sigma^{ij} . \tag{2.16}$$

Here the quantities θ and σ imply the sum over different components of matter and radiation, including baryons, CDM, photons and neutrinos, namely,

$$(\rho + P)\theta = \sum_s (\rho_s + P_s)\theta_s, \qquad (\rho + P)\sigma = \sum_s (\rho_s + P_s)\sigma_s, \tag{2.17}$$

where the index s runs over all particle species.

Based on linear perturbation theory, it is natural to split the Einstein tensor $G_{\mu\nu}$ into background and perturbation components as:

$$G_{\mu\nu} = G^{(0)}_{\mu\nu} + \delta G_{\mu\nu} , \tag{2.18}$$

where '0' denotes the background component. By substituting the FLRW metric in Eq. (2.11), one can derive the background evolution equation, also known as the Friedmann equation,

$$\mathcal{H}^2 = \frac{8\pi G}{3}a^2\rho + \tilde{k}, \tag{2.19}$$

where the $\tilde{k}$ is the spatial curvature constant, with $\{+1, 0, -1\}$ standing for a closed, flat, or open universe, ρ is the total background density of matter and energy. Here $\mathcal{H}$ is the Hubble parameter defined as $\mathcal{H} = \dot{a(\tau)}/a(\tau)$ with the dot representing the derivative w.r.t conformal time τ, and it characterizes the background expansion rate of the Universe. Besides, one

can derive the time derivative (w.r.t conformal time) form of it:

$$\dot{\mathcal{H}} = -\frac{1}{6}a^2(\rho + 3P), \tag{2.20}$$

where P is the total background pressure of matter and energy. Since we focus on the flat spacetime in this work, *i.e.* $\tilde{k} = 0$ in Eq. (2.19), we will then obtain a simpler form of the Friedmann equation,

$$\mathcal{H}^2 = \frac{8\pi G}{3}a^2\rho, \tag{2.21}$$

while the derivative form stays the same as Eq. (2.20).

The Einstein's equation at the perturbation level is given by: $\delta G_{\mu\nu} = 8\pi G\delta T_{\mu\nu}$, which leads to four equations for the Newtonian potentials in Fourier space: [86]

$$k^2\Phi + 3\frac{\dot{a}}{a}\left(\dot{\Phi} + \frac{\dot{a}}{a}\Psi\right) = -4\pi G a^2\delta\rho, \tag{2.22}$$

$$k^2\left(\dot{\Phi} + \frac{\dot{a}}{a}\Psi\right) = 4\pi G a^2(\rho + P)\theta, \tag{2.23}$$

$$\ddot{\Phi} + \frac{\dot{a}}{a}(\Psi + 2\dot{\Phi}) + \left(2\frac{\ddot{a}}{a} - \frac{\dot{a}^2}{a^2}\right)\Psi + \frac{k^2}{3}(\Phi - \Psi) = 4\pi G a^2\delta P, \tag{2.24}$$

$$k^2(\Psi - \Phi) = -12\pi G a^2(\rho + P)\sigma. \tag{2.25}$$

Note that only two of the equations above are independent due to the Bianchi identity, *i.e.* $\nabla_\mu G^{\mu\nu} = 0$. One can substitute Eq. (2.23) into Eq. (2.22) to form the Poisson equation for Φ, which is algebraic:

$$k^2\Phi = -4\pi G\ a^2\rho\Delta, \tag{2.26}$$

where $\rho\Delta \equiv \sum_s \rho_s\Delta_s$ and Δ_s is the comoving matter density contrast, which relates to matter density contrast $\delta_s = \delta\rho_s/\rho_s$ via:

$$\Delta_s = \delta_s + \frac{3\mathcal{H}(1 + w_s)\theta_s}{k^2}, \tag{2.27}$$

where $w_s = P_s/\rho_s$, with index s running over all particle species. Then combining with (2.25), which is also algebraic, one can obtain the Poisson equation for Ψ. Thus, out of four perturbed Einstein equations, one only needs two algebraic equations:

$$k^2\Psi = -4\pi G\ a^2[\rho\Delta + 3(\rho + P)\sigma], \tag{2.28}$$

$$k^2(\Phi - \Psi) = 12\pi G\ a^2(\rho + P)\sigma\ . \tag{2.29}$$

The cosmological redshift is commonly defined as: $z = 1/a - 1$, with a being the scale factor as introduced before, and we have $a = 1$ at present time. Upon entering the matter-domination era, which corresponds to approximately redshift $z < 1000$, the anisotropic stress from photons and neutrinos is negligible, leading to $\Phi = \Psi$ in the late-time Universe.

In addition, the combined energy-momentum tensor of all the particle species is conserved, namely, its covariant derivative will satisfy:

$$\nabla_\mu T^{\mu\nu} = \partial_\mu T^{\mu\nu} + \Gamma^\mu_{\gamma\mu} T^{\gamma\nu} + \Gamma^\nu_{\mu\gamma} T^{\mu\gamma} = 0. \tag{2.30}$$

We will focus on the matter species, *i.e.* baryons and CDM. The (00) and the (0i) components of Eq. (2.30) give the continuity equation and the Euler equation of the matter species, respectively. For baryons, taking into account their coupling to photons, they are

$$\dot{\delta}_b + \theta_b - 3\dot{\Phi} = 0, \tag{2.31}$$

$$\dot{\theta}_b + \mathcal{H}\theta_b = k^2\Psi + c_s^2 k^2 \delta_b + \frac{4\rho_\gamma}{3\rho_b} a n_e \sigma_T (\theta_\gamma - \theta_b), \tag{2.32}$$

where the labels b, and γ refer to baryons and photons, respectively, and $c_s^2 = \frac{\delta P}{\delta\rho}$ is the square of sound speed. The last term on the right side of Eq. (2.32) is due to coupling between baryons and photons before recombination, in which n_e gives the proper mean density of free electrons, and σ_T is the cross-section of the Thompson scattering. Note all time derivatives here are taken w.r.t conformal time. For CDM, the Euler equation takes a simpler form since CDM is not interacting with the other particle species in ΛCDM model, namely,

$$\dot{\delta}_c + \theta_c - 3\dot{\Phi} = 0, \tag{2.33}$$

$$\dot{\theta}_c + \mathcal{H}\theta_c = k^2\Psi, \tag{2.34}$$

where c denotes CDM. Using Eqs (2.32)-(2.34), one can derive the evolution dynamics of baryons and CDM in the conformal Newtonian gauge.

The matter perturbations in the conformal Newtonian gauge and synchronous gauge are related to each other via [86]:

$$\delta^{(\text{syn})} = \delta^{(\text{Newton})} - \alpha\frac{\dot{\rho}}{\rho},$$

$$\theta^{(\text{syn})} = \theta^{(\text{Newton})} - \alpha k^2, \tag{2.35}$$

where $\alpha = (\dot{h} + 6\dot{\eta})/(2k^2)$. By applying these conversion relations, we may also acquire the continuity and Euler equations for baryons and CDM in the synchronous gauge as:

$$\dot{\delta}_b + \theta_b + \frac{1}{2}\dot{h} = 0, \tag{2.36}$$

$$\dot{\theta}_b + \mathcal{H}\theta_c = c_s^2 k^2 \delta_b + \frac{4\rho_\gamma}{3\rho_b} a n_e \sigma_T (\theta_\gamma - \theta_b), \tag{2.37}$$

$$\dot{\delta}_c + \theta_c + \frac{1}{2}\dot{h} = 0, \tag{2.38}$$

$$\dot{\theta}_c + \mathcal{H}\theta_c = 0. \tag{2.39}$$

2.2 Cosmic Microwave Background

The cosmic microwave baryonicackground (CMB) is the leftover radiation from the early epoch, serving as basic evidence for the hot Big Bang theory. During the recombination period, the protons and electrons recombined to form hydrogen, which marks the end of the Thompson scattering. The photons decoupled with baryons and begin the free streaming process from the last scattering surface. In this section, we will focus on the scalar mode perturbations only, which is the main and the only observationally confirmed contribution to the temperature and polarization anisotropies, and the one relevant to the large scale structure of the Universe.

The CMB radiation field is characterized by a rank-2 intensity tensor I_{ij}, which also contains the temperature and polarization information: [88, 89]

$$I_{ij} = \begin{pmatrix} \langle |E_1|^2 \rangle & \langle E_1 E_2^* \rangle \\ \langle E_2 E_1^* \rangle & \langle |E_2|^2 \rangle \end{pmatrix} = \begin{pmatrix} I+Q & U-iV \\ U+iV & I-Q \end{pmatrix}. \tag{2.40}$$

where I, Q, U, V are Stoke's parameters, in which the intensity I is associated with the temperature anisotropies, and Q and U describe the linear polarization. V represents circular polarization, and is not expected to be generated in the standard cosmological model. E_1 and E_2 represent the polarization components of electromagnetic field formed on the orthogonal basis, perpendicular to the propagation direction $\hat{n}$.

The intensity I of radiation at a given frequency is given by the black body spectrum, namely,

$$I(T) = \frac{2h\nu^3}{c^2} \frac{1}{e^{h_{Pl}\nu/k_B T} - 1}, \tag{2.41}$$

where ν denotes the frequency of the radiation, h_{Pl} is Planck's constant, c is the speed of light, k_B is Boltzmann's constant and T is the black body temperature. Because Thomson scattering preserves the black body nature of CMB, it is conventional to represent anisotropies of CMB intensity in terms of anisotropies of the black body temperature. The dimensionless temperature perturbation observed at a given direction on the sky $\hat{n}$ is defined as

$$\Theta(\hat{n}) = \frac{\Delta T(\hat{n})}{\bar{T}}, \tag{2.42}$$

where $\bar{T} \approx 2.726$ K is the mean CMB temperature.

The CMB is observed to be nearly Gaussian distributed. To extract the statistics of CMB perturbations, the temperature anisotropy, $\Theta(\hat{n})$ is commonly expanded into spherical harmonic functions as:

$$\Theta(\hat{n}) = \sum_{lm} a_{T,lm} Y_{lm}(\hat{n}). \tag{2.43}$$

For a Gaussian random field, $a_{T,lm}$ are completely independent for different moments of l and m, and are characterized by their two-point function, or the angular power spectrum

C_{Tl}, given by

$$C_{Tl} = \frac{1}{2l+1} \sum_m \langle a_{T,lm}^* a_{T,lm} \rangle. \tag{2.44}$$

The complete formalism for CMB polarization was introduced in [88], and the major points can be summarized as follows. The Stoke's parameters Q and U are spin-2 states and can be expanded into spin-2 spherical harmonic series as

$$(Q + iU)(\hat{n}) = \sum_{lm} a_{2,lm} \, {}_2Y_{lm}(\hat{n}), \tag{2.45}$$

$$(Q - iU)(\hat{n}) = \sum_{lm} a_{-2,lm} \, {}_{-2}Y_{lm}(\hat{n}), \tag{2.46}$$

where, like in the case of intensity I, Q and U are in units of the black body temperature fluctuation. The spin-2 polarization multipoles can be combined into linear combinations to define

$$a_{E,lm} = -\frac{(a_{2,lm} + a_{-2,lm})}{2}, \tag{2.47}$$

$$a_{B,lm} = \frac{i(a_{2,lm} - a_{-2,lm})}{2}, \tag{2.48}$$

which separate the parity-even (E) and the parity-odd (B) parts. One can then define two scalar quantities to describe parity-even and parity-odd polarization patterns on the sky as

$$E(\hat{n}) = \sum_{lm} a_{E,lm} Y_l^m(\hat{n}), \tag{2.49}$$

$$B(\hat{n}) = \sum_{lm} a_{B,lm} Y_l^m(\hat{n}), \tag{2.50}$$

Similar to the temperature anisotropies, one can define the angular power spectrum for polarization modes as well,

$$C_{El} = \frac{1}{2l+1} \sum_m \langle a_{E,lm}^* a_{E,lm} \rangle \tag{2.51}$$

$$C_{Bl} = \frac{1}{2l+1} \sum_m \langle a_{B,lm}^* a_{B,lm} \rangle. \tag{2.52}$$

In the actual numerical calculations, *e.g.* in `CAMB` and `MGCAMB`, we adopt angular power spectra for TT, TE, and EE as the observables, given by:

$$C_{TT}^{(\ell)} = (4\pi)^2 \int k^2 dk P_{\mathcal{R}}(k) \left| \Delta_{T\ell}(k) \right|^2, \tag{2.53}$$

$$C_{TE}^{(\ell)} = (4\pi)^2 \int k^2 dk P_{\mathcal{R}}(k) \Delta_{T\ell}(k) \Delta_{E\ell}(k), \tag{2.54}$$

$$C_{EE}^{(\ell)} = (4\pi)^2 \int k^2 dk P_{\mathcal{R}}(k) \left| \Delta_{E\ell}(k) \right|^2, \tag{2.55}$$

where $P_{\mathcal{R}}(k)$ refers to the primodial curvature power spectrum, and $\Delta_{X\ell}(k)$ are defined as below. In Fourier space, $P_{\mathcal{R}}(k)$ can be calculated through $\Delta_{\mathcal{R}}$, which is the amplitude of the primodial curvature perturbation as [90]

$$\langle \Delta_{\mathcal{R}}^*(k_1)\Delta_{\mathcal{R}}(k_2)\rangle = P_{\mathcal{R}}(k)\delta(k_1 - k_2). \tag{2.56}$$

In the Eqs. (2.53)-(2.55), $\Delta_{X\ell}(k)$ are defined as the transfer functions for each correlation case, which are derived using:

$$\Delta_{T\ell}(k) = \int_0^{\tau_0} d\tau S_T^{(S)}(k,\tau)j_\ell(x), \tag{2.57}$$

$$\Delta_{E\ell}(k) = \sqrt{\frac{(\ell+2)!}{(\ell-2)!}} \int_0^{\tau_0} d\tau S_E^{(S)}(k,\tau)j_\ell(x), \tag{2.58}$$

in which $j_\ell(x)$ are the spherical Bessel functions. $S_T^{(S)}(k,\tau)$ and $S_E^{(S)}(k,\tau)$ are the source terms of the CMB radiation field, which are specified by

$$S_E^{(S)}(k\tau) = \frac{3g(\tau)\Pi(\tau,k)}{4x^2},$$

$$S_T^{(S)}(k,\tau) = g\left(\Delta_{T_0} + 2\dot{\kappa}_{op} + \frac{\dot{v}_b}{k}\Pi + \frac{3\dot{\Pi}}{4k^2}\right) + e^{\kappa_{op}}(\dot{\eta} + \ddot{\alpha})$$

$$+ g\left(\alpha + \frac{\dot{v}_b}{k} + \frac{3\dot{\Pi}}{4k^2}\right) + \frac{3g\dot{\Pi}}{4k^2}. \tag{2.59}$$

Here κ_{op} is the total optical depth, g is the visibility function defined as: $g(\tau) = \dot{\kappa}_{op}\exp(\kappa_{op})$, $\alpha = (\dot{h} + 6\dot{\eta})/2k^2$, with η and h the two metric potentials in the synchronous gauge as introduced in Sec. 2.1, and all the dots represent the time derivatives with respect to the conformal time τ. Also, v_b stands for the velocity field of baryons, and Π is the polarization term, which is denoted as

$$\Pi = \Delta_{T_2}^{(S)} + \Delta_{E_2}^{(S)} + \Delta_{E_0}^{(S)}. \tag{2.60}$$

The three quantities on the right side of Eq. (2.60), as well as Δ_{T_0} in Eq. (2.59) are the hierarchical terms, corresponding to the solutions of photon's Boltzmann equations at the perturbation level, which are essentially the dynamical evolution of radiation particles in the phase space formed by their energy and momentum.

In addition to the temperature and polarization anisotropies generated from the last scattering surface, the integrated Sachs-Wolfe (ISW) effect [91] is a secondary anisotropy in the cosmic microwave background (CMB), produced by time variations in the gravitational potential on large scales that CMB photons need to traverse from the surface of last scattering to observers. Because gravitational potentials are traced by the large scale structure (LSS) in the Universe, the ISW effect is correlated with the matter distribution at lower redshifts. The ISW effect is largely sensitive to dark energy and curvature of the Universe,

14

for which gravitational potentials also vary with time, either at the transition epoch from radiation to matter domination or the late time Universe when modified gravity or dark energy has the major influence. Analytically, the ISW effect can written as

$$\left(\frac{\Delta T}{T}\right)_{\text{ISW}} = -\int dx \, e^{\kappa_{op}}[\dot{\Phi} + \dot{\Psi}], \tag{2.61}$$

where κ_{op} is the optical depth, the dot denotes the time derivative with respect to conformal time, and Φ and Ψ are the two Newtonian gravitational potentials. The term $(\dot{\Psi} + \dot{\Phi})$ is equivalent to $(\dot{\eta} + \ddot{\alpha})$ in the synchronous gauge on the right side of Eq. (2.59).

In addition, due to the existence of gravitational potentials which trace the distribution of matter including CDM and baryons on large scales, the trajectory of CMB photons gets deflected in the travelling process from the surface of last scattering to us. To characterize such a distortion effect, we can define the lensing potential based on the gravitational potentials as [92]

$$\Psi_L(\hat{n}) = -\int_0^{\chi^*} d\chi \frac{d_A(\chi^* - \chi)}{d_A(\chi^*)d_A(\chi)}\Big(\Psi(\chi\hat{n}; \tau_0 - \chi) + \Phi(\chi\hat{n}; \tau_0 - \chi)\Big), \tag{2.62}$$

where the term $\tau_0 - \chi$ represents the conformal time at which the photon was at position $\chi\hat{n}$, χ^* is the comoving distance of the photon source, and $d_A(\chi)$ is defined as the angular diameter distance. The CMB lensing can therefore be described by the deflection angle α which is defined as:

$$\alpha = -\int_0^{\chi^*} d\chi \frac{d_A(\chi^* - \chi)}{d_A(\chi^*)d_A(\chi)}\nabla_{\hat{n}}\Big(\Psi(\chi\hat{n}; \eta_0 - \chi) + \Phi(\chi\hat{n}; \eta_0 - \chi)\Big), \tag{2.63}$$

where $\nabla_{\hat{n}}$ denotes the covariant angular derivative on the sphere defined by $\hat{n}$, and $d_A(\chi) = \chi$ under the flat-sky approximation. The consequence of CMB lensing is to redistribute the CMB temperature and polarization anisotropies relative to their original positions on the last-scattering surface. Since CMB anisotropies are sensitive to the lensing potential, it offers another way to measure the latter and compare to the measurements of the weak gravitational lensing of galaxies as described in Sec. 2.4.

2.3 Matter Power Spectrum

The matter power spectrum characterizes the two-point correlation of the matter density field, and it corresponds to the result of transformation from real-space correlation function into Fourier space. Based on the comoving matter density contrast $\Delta(k, z)$, the matter power spectrum can be formulated by:

$$\Delta(\mathbf{k}, z) = \int \frac{d^3x}{(2\pi)^{3/2}}\Delta(\mathbf{x}, z)e^{-i\mathbf{k}\cdot\mathbf{x}}, \tag{2.64}$$

and

$$\langle \Delta^*(\mathbf{k}, z)\Delta(\mathbf{k}', z)\rangle = (2\pi)^3 \delta^{(3)}(\mathbf{k} - \mathbf{k}')P(k), \tag{2.65}$$

where $\delta^{(3)}(\mathbf{k} - \mathbf{k}')$ is the 3-dimensional Kronecker delta function, and the angle brackets on the left side denote the statistical ensemble average of the correlation between two points in the matter density field. Therefore, the matter power spectrum follows:

$$P(k, z) = \frac{2\pi^2 \Delta^2(k, z)}{k^3}. \tag{2.66}$$

Here a factor of k^3 is included to make $\Delta^2(k, z)$ a dimensionless quantity.

In practice, the transfer function $\Delta_{trans}(k, z)$ is adopted to describe the evolution of scalar perturbations, connecting the primodial curvature perturbation $\Delta_{\mathcal{R}}$ to the late-time scalar perturbation mode, as done in the main computational tools: CMBFAST, CAMB, MGCAMB, namely, [93]

$$\Delta(k, z) = \Delta_{\mathcal{R}}(k)\Delta_{trans}(k, z), \tag{2.67}$$

and therefore,

$$P(k, z) = \frac{2\pi^2}{k^3} P_{\mathcal{R}}(k)\Delta^2_{trans}(k, z) \tag{2.68}$$

where $P_{\mathcal{R}}(k)$ is the primodial curvature power spectrum from Eq. (2.56), commonly computed via:

$$P_{\mathcal{R}}(k) = A_s\left(\frac{k}{k_s}\right)^{n_s - 1}. \tag{2.69}$$

Here the parameter k_s is introduced as the pivot scale scalar, n_s is the scalar spectral index, and A_s represents the initial scalar power amplitude at the pivot scale, with the latter two among the six vanilla cosmological parameters in ΛCDM model, and we have ignored the running parameters of the scalar spectral index, $dn_s/d\ln k$ and $d^2 n_s/d\ln k^2$.

Besides, we point out that the transfer function does not only apply to matter density contrast. By replacing the transfer function Δ_{trans} with that of another variable, *e.g.* Weyl potential $W = (\Psi + \Phi)/2$, one can compute the corresponding power spectra: matter-Weyl cross power spectrum $P_{mW}(k, z)$ and Weyl-Weyl power spectrum $P_{WW}(k, z)$.

2.4 Weak Gravitational Lensing

Weak gravitational lensing (WL) describes the phenomenon where the photons radiating from background sources are deflected by the foreground mass distribution that is formed by CDM and clusters of galaxies, along with the associated gravitational potential in the large scale structure. This could be broadly divided into two cases, with the first on the deflection of CMB photons as discussed earlier in Sec. 2.2. The latter refers to the case where galaxies are the background sources, with the photons emitted from them also experiencing deflection in the process travelling from the source to observers, leading to the magnification

of galaxy images, featured by convergence field κ, and also the distortion of galaxy images, which suggests that the shapes of galaxies are changed, commonly known as the cosmic shear effect.

Intrinsically, weak gravitational lensing signal is a statistical measurement of the distribution of source galaxies along with the foreground mass distribution which is traced by the gravitational potentials on large scales. In general, there are three types of observables for weak lensing: galaxy-galaxy clustering, cross correlation of galaxy-galaxy lensing, and lensing-lensing auto correlation, which is also referred to as cosmic shear. The Dark Energy Survey (DES) [94, 95] is a prominent cosmological survey for measuring weak lensing signals, more specifically, the angular correlation functions between galaxy clusters and lensing potential, and here we will adopt the formalism in DES to summarize the weak lensing observables.

Firstly, similar to the scenario of CMB lensing, one may define the lensing efficiency term, as given by:

$$q_\kappa(\chi) = \chi \int_\chi^{\chi_h} d\chi' n_\kappa(z(\chi')) \frac{dz}{d\chi'} \frac{\chi' - \chi}{\chi'}, \tag{2.70}$$

where $n_\kappa(z(\chi))$ is the normalized number density of source galaxies as a function of redshift z, χ is the comoving radial distance, and the upper limit of integral χ_h is the comoving distance to the horizon, which represents the maximum comoving distance over which weak gravitational lensing can affect the light emitted from background source galaxies. Additionally, to describe the number density distribution of foreground galaxies, one can also define:

$$q_{\delta_g}(k, \chi) = b(k, z(\chi)) n_g(z(\chi)) \frac{dz}{d\chi}, \tag{2.71}$$

where $b(k, z)$ is the galaxy bias term specific to the type of galaxies, such as redMaGiC galaxies in DES Year-1 [94, 95] and Year-3 [96], as well as specifications of different cosmological surveys. Working under the Limber approximation [97, 98, 99, 100], for which one assumes small angular separations (thus large multipole moment ℓ) and power spectrum $P(k)$ varies more slowly than spherical Bessel functions, the angular correlation function of galaxy-galaxy clustering can be expressed by:

$$w(\theta) = \int \frac{dl}{2\pi} l J_0(l\theta) \int d\chi \frac{q_{\delta_g}\left(\frac{l+1/2}{\chi}, \chi\right) q_{\delta_g}\left(\frac{l+1/2}{\chi}, \chi\right)}{\chi^2} \times P_m\left(\frac{l+1/2}{\chi}, z(\chi)\right) \tag{2.72}$$

where $J_0(l\theta)$ is the zeroth-order Bessel function, and $P_m(k, z)$ is the matter power spectrum as introduced in Sec. 2.3. Similarly, we can calculate galaxy-galaxy lensing correlation functions as:

$$\gamma_t(\theta) = \int \frac{dl}{2\pi} l J_2(\ell\theta) \int d\chi \frac{q_{\delta_g}(\frac{\ell+1/2}{\chi}, \chi) q_\kappa(\chi)}{\chi^2} P_{mW}\left(\frac{\ell+1/2}{\chi}, z(\chi)\right), \tag{2.73}$$

17

as well as cosmic shear functions given by:

$$\xi_{+/-}(\theta) = \int \frac{dl}{2\pi} l J_{0/4}(\ell\theta) \int d\chi \frac{q_\kappa(\chi)q_\kappa(\chi)}{\chi^2} P_{WW}\left(\frac{\ell + 1/2}{\chi}, z(\chi)\right), \qquad (2.74)$$

where $P_{mW}(k, z)$ is the matter-Weyl power spectrum, $P_{WW}(k, z)$ is the Weyl-Weyl power spectrum, as discussed in Sec. 2.3, $J_2(\ell\theta)$ and $J_4(\ell\theta)$ are different orders of Bessel functions to make the transformation of correlation functions into real angular space, with the neglect of the shear bias terms specific to the galaxy surveys. Other important cosmological surveys that are useful to investigate weak lensing include Kilo-Degree Survey (KiDS) [101], the Large Synoptic Survey Telescope (LSST)[1] and Euclid[2].

2.5 Redshift Space Distortion

As discussed earlier, the redshift of the light emitted by galaxies is mostly determined by the cosmic background expansion. The galaxies, however, also have peculiar velocities caused by the local gravitational potential. The line of sight (LoS) direction of peculiar velocities will make the ditribution of galaxies appear squashed or distorted depending on whether the galaxies are moving towards or away from the observer. Such an effect only changes the positions of those galaxies in the radial direction of redshift space, and this is commonly known as redshift space distortion (RSD). RSD is one of the main probes to measure the growth structure and cosmic velocity field of the Universe.

For starters, we require the galaxy number density to be the same in real space and redshift space, *i.e.*:

$$N_s(\vec{x}_s^3)d^3x_s = N_r(\vec{x}_r^3)d^3x_r, \qquad (2.75)$$

where r denotes the comoving distance in real space, while s denotes the distance in redshift space. RSD effect can then be described by the analytical mapping relation as follows:

$$\vec{s} = \vec{r}\left(1 + \frac{u(r)}{r\mathcal{H}}\right), \qquad (2.76)$$

where $\mathcal{H}$ is the Hubble parameter in conformal time, and $u(r)$ is given by the peculiar velocity field $\vec{v}(\vec{r})$ via:

$$u(r) = \hat{r} \cdot \vec{v}(\vec{r}). \qquad (2.77)$$

From Eq. (2.75), one may apply Jacobian transformation between N_s and N_r, prescribed by:

$$N_s(\vec{x}_s^3) = J(r; s)N_r(\vec{r}_s^3). \qquad (2.78)$$

---

[1]https://www.lsst.org/

[2]https://www.esa.int/Science_Exploration/Space_Science/Euclid

and $J(r; s)$ will follow:

$$J(r; s) = \left(1 + \frac{du}{dr}\frac{1}{\mathcal{H}}\right)^{-1}\left(1 + \frac{u}{r\mathcal{H}}\right)^{-2} \approx \left(1 - \frac{du}{dr}\frac{1}{\mathcal{H}}\right), \tag{2.79}$$

where the last term is dropped due to the large distance approximation, where $kr \gg 1$. In Fourier space, the radial derivative of the velocity field $\frac{du}{dr}$ can be derived through:

$$\frac{du}{dr} = \mu_k \frac{d}{dr}v = \mu_k^2 \nabla \cdot \vec{v}(\vec{r}) = \mu_k^2 \theta, \tag{2.80}$$

where $\mu_k = \hat{r} \cdot \hat{k}$, and we have used the definition of velocity divergence $\theta = \nabla \cdot \vec{v}(\vec{r})$. As established in Sec. 2.1, by using the continuity equation for matter density contrast δ, we can then obtain:

$$\theta = -\dot{\delta} = -f\mathcal{H}\delta, \tag{2.81}$$

where the dot denotes the time derivative w.r.t conformal time, and $f = \frac{d \log \delta}{d \log a}$ is defined as the linear growth rate of the cosmic structure. By combining the equations above, one can get:

$$J(r; s) = 1 + \mu_k^2 f \delta \tag{2.82}$$

As pointed out earlier, the number density conservation of galaxies requires:

$$\bar{N}(1 + \delta_s) = \bar{N}(1 + \delta_r)J(r; s), \tag{2.83}$$

so we can obtain the relation on the matter density contrast δ between redshift space and real space as:

$$\delta_s = \delta_r(1 + f\mu_k^2). \tag{2.84}$$

In linear Kaiser model [102], we can assume galaxy bias is linearly coupled to the matter density contrast, *i.e.*

$$\delta_g = b\delta, \tag{2.85}$$

which leads to

$$\delta_{s,g}(k, z) = \delta_g(k, z)(1 + \beta\mu_k^2), \tag{2.86}$$

where $\beta = f/b$, and also corresponding power spectrum of galaxies that is measured, which takes the form:

$$P_{\delta_{s,g}\delta_{s,g}}(k, \mu_k) = P_{\delta_g\delta_g}(k)(1 + \beta\mu_k^2)^2. \tag{2.87}$$

It is then straightforward to expand the power spectrum in terms of Legendre polynomials as:

$$P_{\delta_{s,g}\delta_{s,g}}(k, \mu_k) = \sum_\ell \left(\frac{2\ell + 1}{4\pi}\right) P_{(\ell)}(k)L_\ell(\mu_k), \tag{2.88}$$

to extract the major statistical information from the monopole (P_0), quadrupole (P_2) and hexadecapole (P_4) of the galaxy power spectrum, since Eq. (2.87) is up to fourth order in μ_k.

In general, we can analyse the RSD effect without the necessity of relating matter density contrast δ to velocity field $u(r)$. Based on Eq. (2.84), we have:

$$\delta_s = \delta_r - \frac{\mu_k^2}{\mathcal{H}}\theta, \tag{2.89}$$

and then one can obtain the redshift-space power spectrum by taking the "square" of two sides of the equation:

$$P_s(k, \mu_k) = P_{\delta\delta}(k) - 2P_{\delta\theta}(k)\mu_k^2 + P_{\theta\theta}\mu_k^4, \tag{2.90}$$

where $P_{\delta\theta}(k) = -2\delta\frac{\theta}{\mathcal{H}}$, and $P_{\theta\theta} = (\frac{\theta}{\mathcal{H}})^2$.

Another observable relevant to RSD effect is the matter clustering amplitude, commonly referred to as the parameter σ_8, which denotes the normalized integration of matter density perturbation over a sphere with radius 8 h^{-1}Mpc, where $h = \frac{H_0}{100\,\mathrm{km/s\,Mpc^{-1}}}$, and H_0 is the Hubble constant giving the present value of Hubble parameter. Namely,

$$\sigma_8^2 = \frac{\left\langle |\int dr^3 \delta(x)|^2 \right\rangle}{|\int dr^3|^2}. \tag{2.91}$$

Alternatively, a commonly chosen parameter to measure is the S_8 paramater, which is also based on σ_8:

$$S_8 = \sigma_8 \left(\frac{\Omega_m}{0.3}\right)^{\frac{1}{2}}, \tag{2.92}$$

where Ω_m is the fractional density of matter.

In practice, what cosmologists directly measure for the RSD signal is $f\sigma_8$, in that it gives the combination of the structure growth rate and the amplitude of matter clustering, and is also insensitive to the galaxy bias, namely, differences between the clustering of galaxies and matter.

2.6 Distance Measures

In modern cosmology studies, the primary aim is to make precise measurements of the expansion rate of cosmic background in order to achieve better interpretation of dark energy. This, however, can not be achieved directly, since we can only observe the light arriving from different regions of the Universe. Given the brightness and the angular size of specific objects, known as standard candles and standard rulers, we are able to deduce the distances from the objects to us and also estimate the expansion rate of the Universe.

The angular diameter distance, denoted as $d_A(a)$, is the ratio between the physical size of the object l and the angular size θ it subtends on the sky, *i.e.* $d_A(a) = l/\theta$. In comoving coordinates, the size of the object is given by l/a, and the distance to it is the comoving distance $\chi(a)$, such that we can express $d_A(a)$ as:

$$d_A(a) = a\chi(a) = \frac{\chi(z)}{1+z}, \qquad (2.93)$$

with the comoving distance $\chi(a)$ given by:

$$\chi(a) = \int_t^{t_0} \frac{dt'}{a(t')} = \int_a^1 \frac{da'}{a'\mathcal{H}(a')}, \qquad (2.94)$$

where t_0 denotes the present time. Therefore, using angular diameter distances and observed redshifts of given objects, we can estimate the comoving distance $\chi(a)$, and infer the expansion rate from it, characterized by the Hubble parameter according to Eq. (2.94). Fortunately, the sound horizon at the surface of last scattering serves as such a standard ruler, setting the scale of the baryon acoustic oscillations (BAO) and the acoustic peaks in the CMB angular spectrum and power spectrum of galaxies. The available BAO measurements include those from the Baryon Oscillation Spectroscopic Survey (BOSS), the Extended Baryon Oscillation Spectroscopic Survey (eBOSS) and the Dark Energy Spectroscopic Instrument (DESI) [103].

The luminosity distance, d_L, connects the intrinsic brightness of a given object with the observed light flux from it. Assuming all photons carry the same energy E_γ, the luminosity of an object is defined as the energy radiated from it per unit time, namely,

$$L_s = \frac{N_\gamma \times E_\gamma}{t}. \qquad (2.95)$$

For a chosen standard candle, the radiated photons that pass a spherical shell at late times will be less than those at earlier times due to the cosmic expansion, following the proportionality of: $N_\gamma(a)/\Delta t \propto a$, and the same rule applies to total energy, hence the luminosity passing through a shell with comoving radius $\chi(a)$ is given by: $L(\chi(a)) = L_s a^2$ across the spherical shell. Then we can define the luminosity distance as:

$$d_L(a) = \frac{\chi(a)}{a}, \qquad (2.96)$$

such that the flux through the same shell is given by:

$$F = \frac{L(\chi(a))}{4\pi\chi^2(a)} = \frac{L_s}{4\pi d_L^2(a)}. \qquad (2.97)$$

Similarly, one can estimate the expansion rate from the luminosity distance given by Eq. (2.96), through the definition of comoving distance in Eq. (2.94). *Type Ia supernovae* (SN

Ia) are a nice example of a standard candle, whose intrinsic luminosity is well-understood. The current datasets for SN Ia measurements are available from Pan-STARRS1 (PS1) Medium Deep Survey [104], which provides Pantheon SN Ia samples, as well as the Sloan Digital Sky Survey (SDSS)-II and the Supernova Legacy Survey (SNLS) collaborations. [105] Besides, the SH0ES project (Supernovae, H_0, for the Equation of State of Dark energy) also uses SN Ia as a standard candle to achieve a more precise measurement on the Hubble constant H_0.

2.7   Phenomenological Parameterisation in `MGCAMB`

In `MGCAMB`, departures from GR are encoded in two phenomenological functions of the scale factor a and Fourier number k, $\mu(a,k)$ and $\gamma(a,k)$, introduced in the Newtonian gauge linearized Einstein equations as

$$k^2\Psi = -4\pi G\ \mu(a,k)\ a^2[\rho\Delta + 3(\rho + P)\sigma], \qquad (2.98)$$

$$k^2[\Phi - \gamma(a,k)\Psi] = 12\pi G\ \mu(a,k)\ a^2(\rho + P)\sigma\ . \qquad (2.99)$$

At late times, the Universe is matter-dominated, when the background density of radiation decreases faster than that of matter, so the anisotropic stress contribution from photons and neutrinos is negligible, and the equations become

$$k^2\Psi = -4\pi G\mu(a,k)a^2\rho\Delta, \qquad (2.100)$$

$$\Phi = \gamma(a,k)\Psi\ . \qquad (2.101)$$

A popular and equivalent parameterization employs $\Sigma(a,k)$, instead of $\gamma(a,k)$, defined as

$$k^2(\Phi + \Psi) = -4\pi G\ \Sigma(a,k)\ a^2[2\rho\Delta + 3(\rho + P)\sigma]\ . \qquad (2.102)$$

In the limit of negligible photon and neutrino anisotropic stress, *i.e.* well after the onset of matter domination, Σ and γ are simply related via

$$\Sigma = \frac{\mu}{2}(1 + \gamma). \qquad (2.103)$$

In the 2019 version of `MGCAMB`, when the user opted to specify μ and Σ, they would be converted into μ and γ using Eq. (2.103), with the subsequent calculations carried by the code in terms of the latter. One of the new features in the 2023 version is the direct implementation of the μ and Σ parameterization in the equations, eliminating the need to assume validity of Eq. (2.103), *i.e.* the need to neglect the anisotropic stress from relativistic particle species.

We note that variations of the gravitational coupling in the Solar System are tightly constrained by lunar ranging [106, 107] and other experiments. The parameterization in Eq. (2.100) implies an effective coupling $G_{\text{eff}} \equiv \mu(a, k)G$, determining the gravitational clustering of matter on cosmological scales, where G is the Newton's constant measured on the Earth. In particular, this parameterization allows for $G_{\text{eff}} \neq G$ at the present time, $a = 1$. This is indeed possible in theories with a screening mechanism [108, 109, 110, 111, 112], allowing for gravity to be different cosmologically, while being indistinguishable from GR in the Solar System. As all screening mechanisms are intrinsically nonlinear, they cannot be described using tools of linear perturbation theory employed in MGCAMB. Hence, while testing gravity on linear scales, we effectively assume the existence of a screening mechanism.

MGCAMB also allows the user to work with functions $Q(a, k)$ and $R(a, k)$, defined as [113]

$$k^2\Phi = -4\pi G \ Q(a, k) \ a^2\rho\Delta, \tag{2.104}$$

$$k^2(\Psi - R(a, k)\Phi) = -12\pi G \ Q(a, k) \ a^2(\rho + P)\sigma. \tag{2.105}$$

An entirely different parameterization of modified growth, also available in MGCAMB, is based on Linder's parameter γ_L [82], defined via $f \equiv [\Omega_m(a)]^{\gamma_L}$, where f is the growth rate and $\Omega_m(a)$ is the background matter density fraction.

For each of the above choices of phenomenological functions, the user can choose a parameterization from a set of built-in options or add their own. The built-in MGCAMB parameterizations can be broadly divided into two categories – those based on the expressions for μ and γ obtained from scalar-tensor theories in the quasi-static approximation, and the *ad hoc* parameterizations introduced in the literature. The latter includes the Planck [42] and DES [43] parameterizations of μ and Σ, while in the former category there are the Bertschinger-Zukin parameterization [114], which applies to most scalar-tensor theories, the generic [31] and the Hu-Sawicki [8] $f(R)$, the symmetron [111] and the dilaton [115, 109, 116]. We note that, in all the scalar-tensor-theory-based parameterizations, it is assumed that baryons and CDM are universally coupled to the scalar field. One of the added features in the 2023 version is the option to constrain scalar field models with coupling only to CDM.

The background evolution in the 2019 version of MGCAMB is set by specifying the DE equation of state, w, with $w = -1$ corresponding to Λ, and built-in options for a constant w and the (w_0, w_a) parameterization [117, 118],

$$w(a) = w_0 + w_a(1 - a). \tag{2.106}$$

The 2023 version has an additional option of a parameterization of the DE density fraction $\Omega_X(a)$. Note that, in the default CAMB, in models with $w \neq -1$, there is a contribution of DE density fluctuations to the Poisson equation calculated either under the assumption of a minimally coupled scalar field [119], *i.e.* the quintessence, or the parameterized post-

Friedmann (PPF) fluid model [120]. In `MGCAMB`, w is an effective quantity that need not be associated with a fluid, hence, the DE perturbations were not included. This, however, led to a small discrepancy between the output of `CAMB` and that of `MGCAMB` with $\mu = \gamma = 1$ for $w \neq -1$ background models. To give the user the option to eliminate this discrepancy, we added the DE perturbation option to the 2023 version of `MGCAMB`.

For a general modified gravity theory, namely the scalar-tensor type of the generalized Brans-Dicke (GBD), the evolution equations of baryons and CDM, including continuity and Euler equations due to the conservation of energy-moment tensor $T_{\mu\nu}$, are the same as those in GR, as described in Sec. 2.1. The exception is the CDM-only coupling model, also known as coupled quintessence (CQ) [121, 122, 34], which is one of the new features implemented in `MGCAMB`, where the conservation equations are modified due to the additional contribution from scalar field pertubation, which we will extensively discuss in Sec. 3.1.2.

In `MGCAMB`, in order to solve the full set of the differential equations, a central quantity to calculate is $\mathcal{Z} = k\alpha - 3\frac{\dot{\eta}}{k}$, where $\alpha = (\dot{h} + 6\dot{\eta})/2k^2$, η and h represent the two scalar fields in the synchronous gauge as introduced in Sec. 2.1, and the dot denotes the time derivative w.r.t. conformal time. It can be obtained by adopting the gauge transformation on the metric pertubations prescribed in [86] as:

$$\Psi = \dot{\alpha} + \mathcal{H}\alpha, \tag{2.107}$$

$$\Phi = \eta - \mathcal{H}\alpha, \tag{2.108}$$

and reordering the terms for $\dot{\eta}$. In Sec. 3.1.3, we present more details on the derivation of this quantity in the case of $\mu - \Sigma$ parameterisation.

As can be seen from Eq. (2.98), the phenomenological function μ significantly modifies the relations between gravitational potential Ψ and comoving matter density contrast Δ, hence it can be measured as the enhancement on the matter power spectrum $P_m(k, z)$ based on Δ, which is employed by the galaxy-galaxy auto correlation function observed in WL signal, and also the RSD, which is a prominent probe of the growth of structure on large scales, as described in Sec. 2.5. On the other hand, the function Σ effectively modifies the Poisson equation for the lensing potential as shown by Eq. (2.102), thus it will have a direct role in lensing-related effects that exist in the cosmological observables. These include lensing-lensing auto correlation and galaxy-galaxy lensing cross correlation in WL, CMB lensing, and the ISW effect in CMB anisotropies C_ℓ as introduced in Sec. 2.2.

Chapter 3

New MGCAMB Tests of Gravity with CosmoMC and Cobaya

In this chapter, we present a new version of MGCAMB, publicly available at `https://github.com/sfu-cosmo/MGCAMB_v4` that comes with tools for using it with `Cobaya` [37, 39, 40] and an implementation in the latest version of `CosmoMC` [37, 123, 38].

3.1   MGCAMB 2023

The new added features of this release of MGCAMB are:

- added compatibility with Cobaya, and an implementation in the latest CosmoMC;

- added Python wrapper to run `MGCAMB` using the Python interface;

- an option to constrain models of a scalar field coupled only to CDM in the QSA limit;

- a direct implementation of the μ-Σ parameterization in the Einstein-Boltzmann solver, eliminating the need to convert to μ-γ using Eq. (2.103);

- added background model based on parameterization of the DE density (as opposed to w), denoted as Ω_X;

- a non-parametric parameterization of μ, Σ and Ω_X, based on a cubic-spline interpolation over a set of discrete nodes in a. This allows a joint reconstruction of μ, Σ and Ω_X [50, 51];

- the option of including DE perturbations to restore the consistency with `CAMB` when working with $w \neq -1$ background models.

In what follows, we describe these new features in more detail.

3.1.1 MGCAMB with Cobaya and CosmoMC

Cobaya and CosmoMC are two commonly-used MCMC samplers in cosmological studies, as introduced in Sec. 1.1. In order to use Cobaya with `MGCAMB`, one needs to install Cobaya first from the Cobaya website [40]. Generally, running Cobaya with `MGCAMB` is the same as running it with `CAMB`. We have created an input `YAML` file, available for download at `https://github.com/sfu-cosmo/MGCobaya`, that includes both the basic cosmological model parameters and `MGCAMB`-specific new parameters along with complete instructions. Users are referred to the provided template file `temp.yaml` and can modify it according to which MG model they want to work with.

Additionally, a new version of MGCosmoMC, which is a modified version of the latest release of CosmoMC with `MGCAMB` implemented in it, is publicly available at: `https://github.com/sfu-cosmo/MGCosmoMC`.

3.1.2 Scalar field coupled only to CDM

`MGCAMB` evolves the full set of Einstein-Boltzmann equations parameterized via the functions μ-γ. Built-in expressions for the latter are typically based on their QSA form in scalar-tensor theories and are derived in the Jordan frame, in which baryons and CDM follow the geodesics and obey the standard conservation equations, while the scalar field is coupled to the metric, thus modifying Einstein equations. The Brans-Dicke type theories, such as $f(R)$, can also be formulated in the Einstein frame, conformally related to the Jordan frame, in which Einstein equations are not modified, but all the matter is non-minimally coupled to the scalar field. As all of our observational tools and units are based on the Standard Model physics, theoretical predictions must be made in the baryon frame, which is the Jordan frame in this case.

In addition to the universally coupled case, it is interesting to study models in which the scalar field only couples to CDM [124, 125]. In this case, the baryon frame is the Einstein frame, i.e. Einstein's equations are not modified. Instead, the CDM conservation equations are modified by the coupling to the scalar field. While the cosmological phenomenology of the universal and CDM-only coupled cases is very similar, the technical implementations of the two in `MGCAMB` are different. In the latter case, $\mu = \gamma = \Sigma = 1$, but the CDM continuity and Euler equations acquire new terms. In the Newtonian gauge, in Fourier space, they are given by (see Appendix A for more details)

$$\dot{\delta}_c + \theta_c - 3\dot{\Phi} - (\beta\dot{\delta\phi}) = 0, \tag{3.1}$$

$$\dot{\theta}_c + \left[\mathcal{H} + \beta\dot{\phi}^{(0)}\right]\theta_c - k^2\Psi = \beta k^2\delta\phi, \tag{3.2}$$

where δ_c is the density contrast, θ_c is the velocity divergence, $\dot{} = \partial/\partial\tau$, $\mathcal{H} = \dot{a}/a$, $\phi^{(0)}$ is the background scalar field, $\delta\phi$ is the perturbation, $m(\phi)$ and $\beta(\phi)$ are the mass and the coupling functions defined in Appendix A. When applying the QSA, we assume that all

time-derivatives of the scalar field can be neglected, giving

$$\dot{\delta}_c + \theta_c \quad = \quad 0, \tag{3.3}$$

$$\dot{\theta}_c + \mathcal{H}\theta_c - k^2\Psi \quad = \quad \beta k^2 \delta\phi \ , \tag{3.4}$$

with $\delta\phi$ algebraically related to the density contrast:

$$\delta\phi = -\frac{\beta\rho_c\delta_c}{k^2/a^2 + m^2} \ , \tag{3.5}$$

thus eliminating the scalar field entirely from all equations. We note that this is a strong version of the QSA which is not applicable to theories in which kinetic energy of the scalar field is a non-negligible fraction of the total energy [126]. However, this is a good approximation for theories like chameleon, symmetron and dilaton, in which the scalar field remains at the minimum of the slowly evolving effective potential. In theories where this is not the case, one should add the scalar field explicitly to the code, which is not done in `MGCAMB`.

For the implementations in `MGCAMB`, it is necessary to convert the CDM Euler equation to synchronous gauge using [86]

$$\delta^{(\mathrm{syn})} \quad = \quad \delta^{(\mathrm{con})} - \alpha\frac{\dot{\rho}}{\rho}, \tag{3.6}$$

$$\theta^{(\mathrm{syn})} \quad = \quad \theta^{(\mathrm{con})} - \alpha k^2 \ , \tag{3.7}$$

where $\alpha = (\dot{h} + 6\dot{\eta})/(2k^2)$, and h and η are the synchronous gauge potentials [86]. And therefore,

$$\dot{\delta}_c + \theta_c + \frac{1}{2}\dot{h} = 0 \tag{3.8}$$

$$\dot{\theta}_c + \mathcal{H}\theta_c = -k^2\tilde{\beta}^2\frac{\rho_c(\delta_c - 3\alpha\mathcal{H})}{k^2/a^2 + m^2}, \tag{3.9}$$

where $\tilde{\beta}(\phi) = \beta(\phi)/\sqrt{8\pi G}$, and all the quantities are now in synchronous gauge.

The 2023 `MGCAMB` has built-in parameterizations for CDM-coupled scalar field models based on the forms of $m(a)$ and $\tilde{\beta}(a)$ in the symmetron and dilaton models as described in [127]. In [122], we tested the validity of the QSA for these models by comparing to the exact solutions with an explicitly present scalar field, and found that the QSA works very well for a broad range of parameters. Other forms of m and $\tilde{\beta}$ are straightforward to add.

3.1.3 Direct $\mu - \Sigma$ parametrization

As mentioned earlier, the original version of `MGCAMB` was based on the set of linearly perturbed Einstein equations parameterized via the functions $\mu(a, k)$ and $\gamma(a, k)$. Depending on the data sets that one considers, it can be preferable to work with the combination

$\mu(a,k)$ - $\Sigma(a,k)$. In the original version, this choice would be first transformed into the corresponding $\mu(a,k)$ - $\gamma(a,k)$, with `MGCAMB` determining γ from $\gamma = 2\Sigma/\mu - 1$, along with the derivatives. As discussed earlier, the latter is an approximated relation valid as long as the modifications occur well-after the onset of matter domination and anisotropic stresses of relativistic species can be neglected. It can be generalized to properly take into account these effects; nevertheless, also in view of numerical accuracy, we opted for adding a direct implementation of μ and Σ, with the latter defined via Eq (2.102), in the equations for perturbations. When working with $\mu - \Sigma$ models, the user can opt for this direct implementation by setting `MG_flag=5`. Using other values for `MG_flag` would revert to the old way based on converting to γ.

The modifications to equations in the $\mu - \Sigma$ case are similar to those for $\mu - \gamma$ described in [33]. Here we point out the main differences. The modified Poisson equations with the $\mu - \Sigma$ parameterization are defined in the Newtonian gauge via Eqs (2.98) and (2.102). To convert to the synchronous gauge, and to find the variable $\mathcal{Z}$ used in `CAMB`,

$$\mathcal{Z} = k\alpha - 3\frac{\dot{\eta}}{k} \ , \tag{3.10}$$

we start with the transformations given by Eqs. (B.4) and (B.5) to find α and $\dot{\alpha}$ as

$$\dot{\alpha} = -\eta - \frac{a^2}{2k^2}\Sigma\Big[2\rho\Delta + 3\rho(1+w)\sigma\Big], \tag{3.11}$$

$$\alpha = \frac{1}{\mathcal{H}}\Big\{\eta + \frac{a^2}{2k^2}\Big[(2\Sigma - \mu)\rho\Delta + (\Sigma - \mu)3\rho(1+w)\sigma\Big]\Big\}. \tag{3.12}$$

Then, following the same steps that were used in the $\mu - \gamma$ case, as described in [33], we obtain

$$\begin{aligned}
\dot{\eta} = \frac{1}{2}&\frac{a^2}{k^2 + \frac{3}{2}a^2(2\Sigma - \mu)\rho(1+w)} \\
&\Big\{(2\Sigma - \mu)k\rho q\Big[1 + \frac{3(\mathcal{H}^2 - \dot{\mathcal{H}})}{k^2}\Big] \\
&+ \rho\Delta\big[2\mathcal{H}(\Sigma - \mu) - (2\dot{\Sigma} - \dot{\mu})\big] \\
&+ k^2\alpha\Big[(2\Sigma - \mu)\rho(1+w) - \frac{2}{a^2}(H^2 - \dot{\mathcal{H}})\Big] \\
&- 2(\Sigma - \mu)\rho\dot{\Pi} + 2\rho\Pi\big[(\Sigma - \mu)3\mathcal{H}(1+w) - (\dot{\Sigma} - \dot{\mu})\big]\Big\},
\end{aligned} \tag{3.13}$$

where $\Pi = \frac{3}{2}(1+w)\sigma$, and $(1+w)\theta = kq$, allowing us to determine $\mathcal{Z}$.

We have tested that, for late-time modifications (which includes all models currently implemented in `MGCAMB`), the results are equivalent to those based on the conversion to γ. Still, the added option gives the users the possibility to work with new models that may involve early-time modifications of μ and Σ.

3.1.4 Effective dark energy density fraction Ω_X

The dynamics of DE in `CAMB` is set by specifying the equation of state parameter w. In this version of `MGCAMB`, we added the option of specifying the DE energy density instead. Namely, we introduce a function $\Omega_X(a)$, defined via the Friedmann equation,

$$\frac{H^2}{H_0^2} = \Omega_r a^{-4} + \Omega_m a^{-3} + \Omega_X(a) , \tag{3.14}$$

where $H = a^{-1}da/dt$ is the Hubble parameter (defined in terms of the physical time t), H_0 is its present value, Ω_r and Ω_m are the fractional energy densities of radiation and matter, respectively, and $\Omega_X = \Omega_{\mathrm{DE}}X(a)$ with $X(a = 1) = 1$ and $\Omega_r + \Omega_m + \Omega_{\mathrm{DE}} = 1$. Thus, $\Omega_X(a)$, describes the collective contribution of any terms other than the radiation and matter densities, including terms due to modifications of gravity that may alter the Friedmann equation. In MG theories, the energy density of the effective DE fluid, defined as above, need not be positive and can cross zero, making its equation of state singular. Hence, when deriving constraints on MG, it is reasonable to avoid introducing w and work with the effective DE density instead.

The effective DE pressure $p_{\mathrm{DE}}^{\mathrm{eff}}$, used in the equations in `CAMB`, can be obtained from $X(a)$ via [128]

$$Y = -X - \frac{1}{3}\frac{dX}{da}a, \tag{3.15}$$

with $Y(a) = p_{\mathrm{DE}}^{\mathrm{eff}}(a)/\rho_{\mathrm{DE}}^{\mathrm{eff}}(a = 1)$.

In the current version of `MGCAMB`, $\Omega_X(a)$ is implemented as a cubic spline over a discrete set of nodes, as detailed in the next section. Other parameterizations can be added following the general scheme for adding new models to `MGCAMB`.

To work with Ω_X, one needs to choose `DE_model = 3` in the `params_MG.ini` file. This option can be used independently from the choice of parameterizations of μ and Σ. For example, to use the "DES" parameterization along with Ω_X, one needs to set `MG_flag = 1`, `pure_MG_flag = 2`, `musigma_par = 1` and `DE_model = 3`.

3.1.5 The cubic-spline parameterization and reconstructions

To allow for a non-parametric reconstruction of the functions μ, Σ and Ω_X, in this release, we provide an implementation of a pixelization which can be easily modified or extended by the user for their own purpose.

We restrict to the time-dependent case, and parameterize the functions μ, Σ and Ω_X by fitting nodes placed at certain chosen redshifts, and the values of these functions at intermediate redshifts are determined by a cubic spline interpolation. In the code, each function is assigned with 11 fitting nodes, with the first ten uniformly distributed in the redshift range of $z \in [0,3]$, and the last one set at $z = 4$. This is because most observations can only provide tomographic measurements at $z < 3$, thus variations of these functions beyond

29

$z = 3$, if any, are difficult to probe. From $z = 4$ to $z = 1000$, we require all three functions to smoothly transit from the fitted value at $z = 4$ to the ΛCDM value, which are unity for μ, Σ, and Ω_{DE} for Ω_X. This is hardcoded using 9 additional nodes uniform in the scale factor a whose values are determined by a `tanh` function. In sum, there are $11 \times 3 - 1 = 32$ free parameters[1] to be determined, which is quite challenging given the strong degeneracies among these parameters. The way out is to apply the correlated priors [129, 130], which can be calculated in theory [51, 50], to remove the flat directions of the likelihood surface. The covariance matrices for a few correlated priors are available in the MGCosmoMC package: `https://github.com/sfu-cosmo/MGCosmoMC`, under `data/corr_prior`. To make the priors work with Cobaya, one would need to construct an external likelihood class following the general way instructed on the Cobaya website [40]. The priors are simply implemented as a new contribution to the total χ^2 via:

$$\chi^2 = (\mathbf{f} - \mathbf{f}_{\mathrm{fid}}) \, \mathcal{C}^{-1} \, (\mathbf{f} - \mathbf{f}_{\mathrm{fid}})^T \,, \tag{3.16}$$

where $\mathbf{f} \equiv \{\Omega_{Xi}, \mu_i, \Sigma_i\}$ describes the discrete nodes for the functions, with the fiducial value $\mathbf{f}_{\mathrm{fid}}$ determined by the so-called running average method [16] to avoid the statistically biased result, instead of the mean value obtained from the covariance matrices for the functions, which is denoted as $\mathcal{C}$ in the expression.

Note that these three functions do not have to be in the same parametric form. For example, when μ and Σ are parameterised using the aforementioned fitting nodes with the cubic spline, dark energy can take the (w_0, w_a) parametrization, in which case one needs to set `MG_flag = 6` and `DE_model = 2` in the `params_MG.ini` file. Likewise, when Ω_X is a free function with fitting nodes, μ and Σ can take a simpler form as already mentioned in the previous subsection.

3.1.6 DE perturbations

A dynamical DE, *i.e.* any form of DE other than Λ, necessarily implies inhomogeneities in the DE fluid [131]. In `CAMB`, in models with $w \neq -1$, the DE stress-energy fluctuations are computed either based on a quintessence scalar field [119] or the PPF fluid model [120]. In previous versions of `MGCAMB`, the DE contribution to the stress-energy perturbations was not included in the perturbed Einstein equations. Instead, it was assumed that their contribution would be absorbed into the phenomenological functions μ and γ. This, however, caused a small but noticeable difference between the best fit parameters obtained using `CAMB` compared to the $\mu = \gamma = 1$ limit of `MGCAMB` for $w \neq -1$ background cosmologies. In the current version, we have added the option `MGDE_pert` in the `params_MG.ini` to include the DE perturbations, calculated using the quintessence or the PPF model, in the equations of

---

[1] $X(a = 1) = 1$ by definition.

`MGCAMB`, in the same way as they appear in `CAMB`. Whether the DE perturbations should be included when running `MGCAMB` depends on the context.

In MG theories, the DE equation of state w is not necessarily representative of a scalar field, or a conserved fluid assumed by the PPF model. Rather, it is an effective quantity representing the overall modification of the Friedman equation due to changes to the Einstein equation as well as the impact of inhomogeneities in the extra degree of freedom. Hence, using the quintessence or the PPF model for DE perturbation when performing model-agnostic tests of MG is, strictly speaking, theoretically inconsistent. On the other hand, if the user's priority is to be able to recover the default-`CAMB`-based results in the $\mu = \gamma = \Sigma = 1$ limit when running $w \neq -1$ models, they should include the DE perturbations.

In addition to the DE perturbations arising from DE dynamics, in scalar-tensor theories, in the Einstein frame, there is a contribution to the energy density perturbations in the Poisson equation due to the non-minimal coupling of the scalar field to matter. Since the baryon frame in the CDM-only coupled case is the Einstein frame, this term appears on the right hand side of Eq. (A.6). We note that it is generally very small on sub-horizon scales and could be safely neglected for models for which the QSA holds well. Nevertheless, we keep it for completeness.

3.2   Testing gravity with the new MGCAMB

In what follows, we demonstrate the use of the new `MGCAMB` for deriving constraints on parameters of two new models that were not present in previous versions. The first is the CDM-only coupled symmetron, which we compare to the universally (all matter) coupled case. The second is a joint reconstruction of Ω_X, μ and Σ as functions of redshift using the cubic spline model with and without the Horndeski prior.

3.2.1   Constraints on the universally and the CDM-only coupled symmetron

The built-in parameterizations in `MGCAMB` include the symmetron and dilaton models described in terms the QSA forms of the mass function $m(a)$ and the coupling $\tilde{\beta}(a)$. As described in Sec. 3.1.2, in addition to the previously implemented case of the scalar field universally coupled to all matter, the current version also includes the option for the scalar field coupled only to CDM. Fig. 3.1 compares the matter power spectra of two scalar field models, symmetron and dilaton, with CDM-only *vs* universal coupling. In both cases and for both models there is an enhancement due to the fifth force. However, this enhancement is smaller in the CDM-only coupled case, since the fifth force affects only a fraction of total matter.

In what follows, we compare the constraints on the symmetron model for the two cases with the universal and the CDM-only coupling. To work with this model, we set `MG_flag=3,`
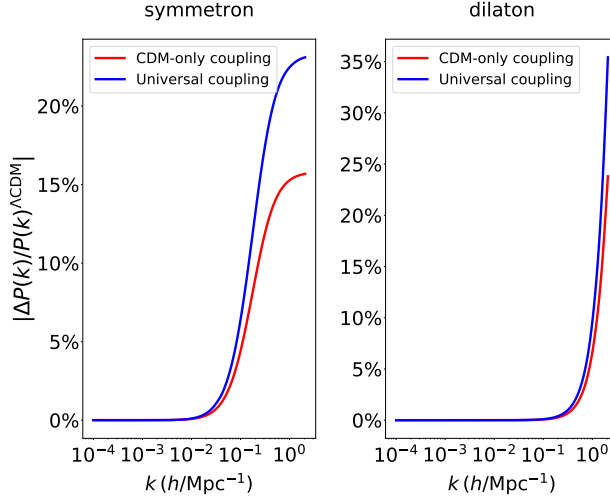
Figure 3.1: The relative difference in the matter power spectrum for two scalar field models with universal and CDM-only coupling compared to ΛCDM model. For the symmetron model, the parameter values are $\beta_* = 1.0$, $\xi_* = 10^{-3}$ ($\lambda_c = 4.29$ Mpc), $a_* = 0.5$; while the parameter values for dilaton model are $\beta_0 = 1.0$, $\xi_0 = 10^{-4}$ ($\lambda_c = 0.43$ Mpc), $a_{\text{trans}} = 0.001$, where a_{trans} sets the transition time from GR to MG regime. In both panels, the blue line corresponds to the CDM-only coupled scalar field, while the red line corresponds to the universally coupled scalar field.

`QSA_flag = 2` for the universal coupling and `MG_flag=4, QSA_flag = 2, CDM_flag = 1` for the CDM-only coupling in the `params_CMB_MG.ini` file for the CosmoMC runs, or the input `YAML` file if using Cobaya.

In the symmetron model, under the QSA, the functions $\tilde{\beta}(a)$ and $m(a)$ are given by [116, 127]

$$\tilde{\beta}(a) = \beta_\star \sqrt{1 - \left(\frac{a_\star}{a}\right)^3}, \tag{3.17}$$

$$m(a) = \frac{H_0}{c}\frac{1}{\xi_\star}\sqrt{1 - \left(\frac{a_\star}{a}\right)^3}, \tag{3.18}$$

for $a > a_\star$, where a_* is the scale factor at which the symmetry breaking takes place. Prior to the symmetry breaking, the minimum of the effective scalar field potential is at $\phi = 0$, implying $\tilde{\beta}(a) = 0$. Hence, under the QSA, the symmetron model reduces to ΛCDM, and we evolve the ΛCDM equations for $a < a_\star$. In [122], it was found that these QSA-based expressions work well for a broad range of parameters.

Current data is unable to constrain all three symmetron parameters (ξ_*, β_* and a_*) simultaneously. For our demonstration, we set $\beta_* = 1$ and $a_* = 0.5$, and constrain the remaining parameter ξ_* that sets the Compton wavelength of the fifth force mediated by

coupling	Universal coupling	CDM-only coupling	Universal coupling+A_L	CDM-only coupling+A_L
ξ_*	0.0011	0.0016	0.0013	0.0022
$\lambda_c(\mathrm{Mpc})$	4.743	7.051	5.802	9.539

Table 3.1: The 2σ upper bounds on ξ_* and λ_c for the two models with fixed and varying A_L, respectively, as defined in the text.
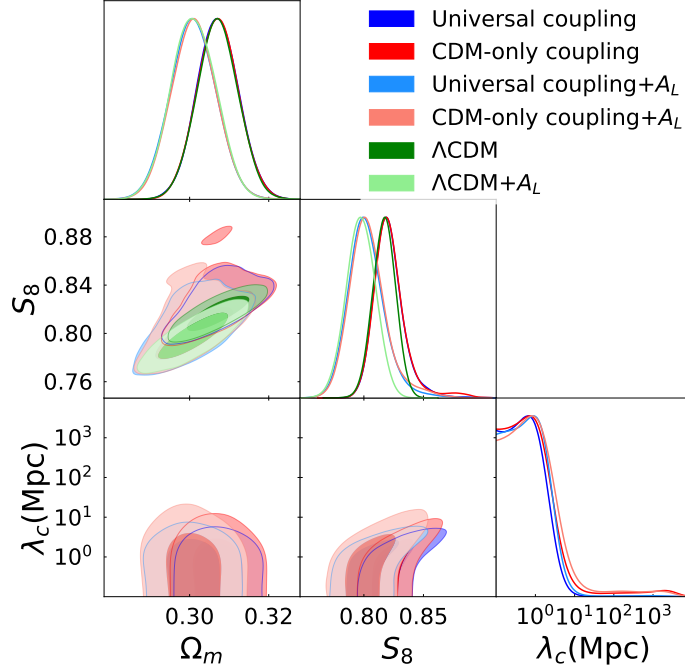
Figure 3.2: The 68% and 95% marginalized confidence level contours for Ω_m, S_8 and λ_c in the universally coupled (blue) and the CDM-only coupled symmetron (red), with fixed and varying A_L, respectively. The other symmetron model parameters are fixed at $\beta_* = 1$ and $a_* = 0.5$. The ΛCDM (green) contours are shown for comparison.

the scalar field,

$$\lambda_c = \frac{c}{H_0}\xi_* \; . \tag{3.19}$$

We present our results in terms of λ_c.

We use the new version of `MGCosmoMC` to compare constraints on λ_c in the symmetron model with universal and CDM-only coupling. Along with ξ_*, we vary the main cosmological parameters: $\Omega_b h^2$, $\Omega_c h^2$, θ, τ, n_s and $\ln[10^{10}A_s]$. Our dataset includes the Planck 2018 CMB temperature, polarization and lensing [132], joint measurements of baryon acoustic oscillations (BAO) and redshift-space distortions (RSD) from the Baryon Oscillation Spectroscopic Survey (BOSS) Data Release 12 (DR12) [62], the SDSS DR7 MGS data [133], the BAO measurement from 6dF [134], and the Dark Energy Survey (DES) Year 1 galaxy-galaxy-lensing correlation data [94] with the standard cut of nonlinear scales (see [33] for more details on the implementation of the cut). We use a logarithmic prior on ξ_* covering seven orders of magnitude, $\xi_* \in [10^{-6}, 1]$.

Fig. 3.2 shows the marginalized joint constraints on λ_c for the universal and the CDM-only coupling cases, along with the derived parameters S_8 and Ω_m. As expected, λ_c is constrained more stringently in the universally coupled case compared to the CDM-only coupled case, whether the CMB lensing parameter, A_L, is fixed or set free to vary, since all of the matter is affected by the fifth force in the universally coupled case. The quantitative 68% and 95% confidence level constraints on λ_c cannot be readily obtained from `getdist` due to the fact that we use a logarithmic prior and the parameter is unbounded from below. Instead, in Table 3.1, we provide the "2σ" upper bounds on ξ_* and λ_c defined as the value of the parameter at which the marginalized probability is equal to $1/e^2$ of the peak value. For a Gaussian distribution, this would set the 95% confidence level, or the 2σ bound.

We note that there is a degeneracy between S_8 and λ_c at larger values of S_8, which is plausible since the fifth force tends to increase the clustering amplitude of matter. Note that the value of Ω_m stays the same, *i.e.* the increase in clustering can be achieved without increasing the matter fraction. In addition, the mean values of Ω_m and S_8 are lower when A_L is varying, since CMB temperature data tends to elevate Ω_m and S_8 due to the preference for more CMB lensing effects when A_L is fixed. Instead, when A_L is varied, one finds a preference for $A_L > 1$.

3.2.2 Reconstructing gravity with and without a Horndeski prior

As a second worked out example, we perform a combined non-parametric reconstruction of Ω_X, μ and Σ from current cosmological data. We set `{MG_flag=6, DE_flag=3}` in the input `params_CMB_MG.ini` file, which corresponds to modeling all three functions through the cubic spline over 11 fitting nodes in redshift, as described in Sec. 3.1.5. We fit the resulting 32 free parameters of the theory, along with the standard cosmological parameters, to data, considering both the case with and without the Horndeski correlated prior (as already discussed, the Horndeski prior can be added by including `cor_prior_Hor_ox.ini` and setting `use_SMPrior = T` in the input `.ini` file).

Our dataset is comprised of the Planck 2018 CMB temperature, polarization and lensing spectra [132], the full shape consensus results of joint measurements of BAO and RSD from BOSS DR12 [62] complemented by portion of the eBOSS DR16 data release [135, 136, 137, 137, 137, 137, 138] not included in DR12, the BAO measurements from MGS and 6dF, the Pantheon sample of uncalibrated supernovae [104], along with the DES Y1 data with the standard cut of nonlinear scales. The results are shown in Fig. 3.3 and Fig. 3.4. They reproduce the more general results obtained in [50, 51], where the same set of data were used. We refer the reader to the latter work for an extensive discussion of the findings. Here we shall simply comment on the main points: the reconstructed functions are consistent with their ΛCDM predictions within $2-3\,\sigma$; the role of the prior, in preventing overfitting of the data, is clearly visible; all three functions show some mild deviations from their ΛCDM values, hinting at the features that would be needed for late time dark energy in

order to ease some of the cosmological tensions [5]. In particular, as can be seen in Fig. 3.3, it is possible for late time modifications to ease the S_8 tension if A_L, is let free to vary. This is achieved mostly through the combined behaviour of Ω_X and μ, with an increase in Ω_X at intermediate redshifts, and μ achieving values above unity at low and intermediate redshifts, while Σ is close to unity in the redshift range relevant for the CMB lensing kernel.

One expects the values of μ, Σ and Ω_X at adjacent redshifts not to be entirely independent, as these functions are generally smooth and correlated with each other. The Horndeski correlated prior plays an important role in suppressing the likelihood of abrupt unphysical changes in the data-only reconstruction, preventing an overfitting and ensuring that the reconstruction is independent of the binning scheme. We use the prior covariance obtained from the ensemble of cosmological histories within Horndeski theories generated in [48]. There, the space of Horndeski models was sampled by varying the five free functions of time that appear in the effective field theory (EFT) action for (linear) Horndeski gravity, keeping only the solutions that satisfy basic principles of physical viability (*e.g.* no instabilities) and are in broad agreement with the observed cosmic expansion history. The strength of the resultant correlation depends on the amount of freedom in a given model (*e.g.* the entire Horndeski *vs* only the Brans-Dicke subset). We have made the covariance matrices for a few correlated priors available in the `MGCosmoMC` package, but the user could follow the same template to build other correlation matrices, e.g. for other theories of gravity.

While it is not evident from the results that we are presenting here, in the original reconstruction work [51] it was shown that current cosmological data can constrain 15 combined modes of Ω_X, μ and Σ. This is already significantly more than the few parameters typically employed in simple parameterizations and highlights the importance of non-parametric methods.
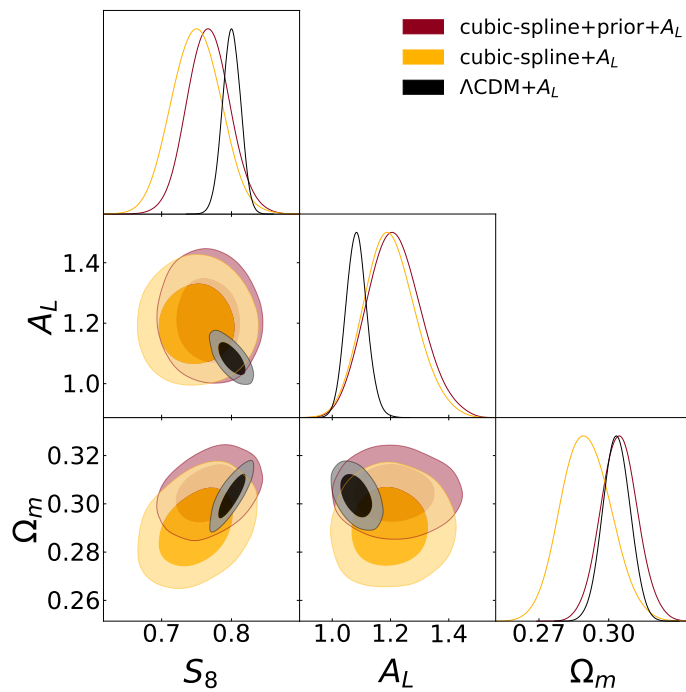
Figure 3.3: The 68% and 95% marginalized confidence level contours for S_8, A_L and Ω_m, in the cases of joint reconstruction of μ, Σ and Ω_X using the same datasets with varying A_L, with and without the Horndeski prior, respectively, in comparison with ΛCDM model.
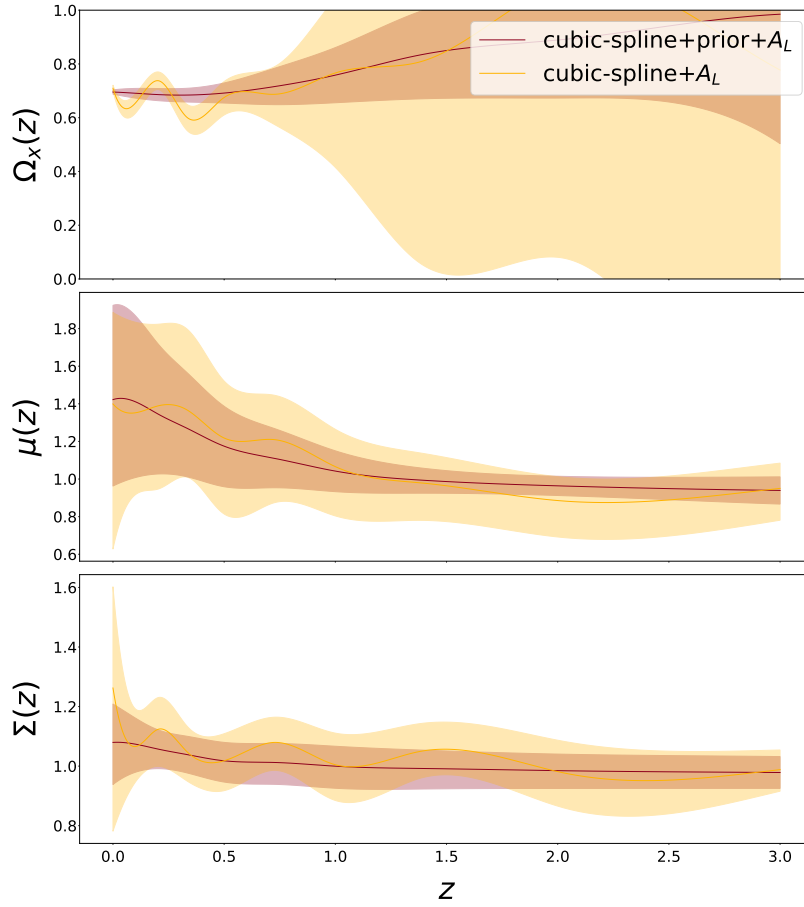
Figure 3.4: The evolution of μ, Σ and Ω_X derived from the reconstruction by cubic-spline model, using all data with varying A_L, with and without the Horndeski prior. The bands in all subplots correspond to the 68% confidence level regions obtained from the marginalized posterior distributions for each node, and the solid lines inside the bands correspond to the mean values of parameter functions.

Chapter 4

Disentangling Modified Gravity from a Dark Force with Gravitational Redshift

As discussed earlier in Sec. 1, it is of fundamental importance to be able to distinguish a modification to gravity from a dark fifth force acting only on dark matter. In Ref. [121], it was shown that this cannot be achieved with current observables. The growth rate of structure is affected by the modifications in both scenarios, potentially in the very same way. On the other hand, weak lensing, which is sensitive to the sum of the two gravitational potentials describing the geometry of the Universe, is also generically unable to discriminate between the two cases. While it is possible to look for observational signatures of specific models (see e.g. Refs. [112, 139, 140]), these two scenarios cannot be disentangled without knowing a priori which kind of modifications (if any) are present in the data.

Ref. [121] however pointed out that the degeneracy can be broken by considering measurements of an observable accessible by the coming generation of galaxy surveys: gravitational redshift [141, 142]. This effect, originally predicted by Einstein [143], directly probes the gravitational potential encoding the distortion of time and entering the Euler equation. This yields an immediate test of modified gravity and provides a way to distinguish it from the presence of a fifth force acting on dark matter.

In this work, we quantify the capability of gravitational redshift to break the degeneracy between gravity modifications and a dark fifth force, performing a Markov Chain Monte Carlo (MCMC) analysis on synthetic data, based on the survey specifications of the Square Kilometer Array Phase 2 (SKA2) [144]. We consider two specific models: the symmetron modified gravity model [111], which is a scalar-tensor theory of generalized Brans-Dicke (GBD) type, and a coupled quintessence (CQ) model [124, 125] with exactly the same form of the coupling and the potential as the symmetron, but with only dark matter coupled to the scalar field. We show that the parameters of the two models are fully degenerate in an analysis including RSD, weak lensing and cosmic microwave background (CMB) data.

We then demonstrate that including gravitational redshift into the analysis breaks the degeneracy, and we determine how large the deviations from ΛCDM need to be for this observable to be effective.

The rest of this chapter is organized as follows. In Sec. 4.1, we present the GBD and CQ models considered in our analysis, highlighting their degeneracies in RSD and weak lensing data. We then describe the galaxy clustering, weak lensing and CMB observables included in the analysis in Sec. 4.2 and discuss the details of the numerical investigation in Sec. 4.3. Finally, we present the results in Sec. 4.4. We include some additional details on the GBD and CQ models in Appendix C and on the specifications for the galaxy clustering observables in Appendix D.

4.1 The two degenerate scenarios

4.1.1 GBD and CQ

In order to illustrate the disentangling power of gravitational redshift, we compare a modified gravity model with a scenario involving a dark fifth force acting on dark matter. The argument that follows is fully general and applicable to any model belonging to these categories, but for the sake of concreteness, we focus on a GBD scalar-tensor theory and a CQ model, following Ref. [121]. Both scenarios involve an additional scalar field, according to the actions given in Appendix C. In the GBD case, the scalar field has the same conformal coupling to all cosmic components, whereas in CQ the coupling only involves dark matter (in the form of CDM) and propagates a dark force of non-gravitational origin. We denote the coupling strengths with β_1 and β_2 and the scalar field masses with m_1 and m_2 in the GBD and CQ models, respectively.

We work within linear perturbation theory and assume that the Universe is described by a perturbed flat Friedmann-Lemaître-Robertson-Walker (FLRW) metric in the conformal Newtonian gauge, with line element

$$\mathrm{d}s^2 = a^2[-(1+2\Psi)\mathrm{d}\tau^2 + (1-2\Phi)\mathrm{d}\mathbf{x}^2]\,, \tag{4.1}$$

where τ denotes conformal time and a the scale factor. The two metric potentials Ψ and Φ encode perturbations in the geometry of the Universe. The matter content can be described by two fields: the density contrast $\delta = \delta\rho/\rho$ and the velocity divergence θ. These contain contributions from both CDM (c) and baryons (b), $\rho\delta = \rho_b\delta_b + \rho_c\delta_c$ and $\rho\theta = \rho_b\theta_b + \rho_c\theta_c$. The relations among these fields, listed in Appendix C, are provided by the chosen theory of gravity and the energy-momentum conservation. In particular, we notice that the GBD scenario involves a nonzero anisotropic stress and modifications in the Poisson equation, whereas the CQ case only includes modifications in the Euler equation for CDM.

4.1.2 Impact on the growth of cosmic structure

Let us analyze the implications of the GBD and CQ scenarios on the growth of cosmic structure. In either scenario, combining the Einstein and conservation equations yields an equation for the growth of density fluctuations in the linear regime of the form

$$\ddot{\delta} + \mathcal{H}\dot{\delta} = 4\pi G_{\text{eff}} a^2 \rho \delta \,. \tag{4.2}$$

Here, overdots indicate derivatives with respect to conformal time, $\mathcal{H}$ is the conformal Hubble parameter and G_{eff} is the effective Newton constant that encodes the effective gravitational coupling. The latter takes the following form in the two models:

$$G_{\text{eff}}^{\text{GBD}} = G\left[1 + \frac{2\tilde{\beta}_1^2 k^2}{a^2 m_1^2 + k^2}\right] \,, \tag{4.3}$$

$$G_{\text{eff}}^{\text{CQ}} = G\left[1 + \frac{2\tilde{\beta}_2^2 k^2}{a^2 m_2^2 + k^2}\left(\frac{\rho_c}{\rho}\right)^2\left(\frac{\delta_c}{\delta}\right)\right] \,, \tag{4.4}$$

where G is the Newton constant and we have defined $\tilde{\beta}_i^2 = \beta_i^2/(8\pi G)$, for $i = 1, 2$. We remark that the only difference between the two expressions is the term $(\rho_c/\rho)^2 (\delta_c/\delta)$ suppressing the value of G_{eff} in the CQ case, due to the fact that the coupling only affects CDM in this scenario. However, such a difference can be absorbed into the unknown value of the coupling β_2. Therefore, measurements of the growth of cosmic structure that only constrain G_{eff} cannot distinguish between a scenario where $\beta_1 = 0$ (GR is valid) and $\beta_2 \neq 0$ (CDM experiences a fifth force), and a scenario where $\beta_1 \neq 0$ (gravity is modified) and $\beta_2 = 0$ (there is no dark fifth force). In general, if we analyze the data allowing for both β_1 and β_2 to vary, we see from Eqs. (4.3) and (4.4) that one can only constrain the combination $\beta_1^2 + (\rho_c/\rho)^2 (\delta_c/\delta) \beta_2^2$. While the shape of the degeneracy depends on the specific models considered, deviations in the Poisson and the Euler equations are generically indistinguishable through measurements of the growth of structure [145].

4.1.3 Impact on weak lensing

The other key large-scale structure observable is weak lensing, measured in cosmic shear, magnification of high-redshift galaxies, and the lensing of the CMB. Weak lensing is directly sensitive to the Weyl potential, *i.e.* the sum of the two gravitational potentials Φ and Ψ [93]. However, as shown in Ref. [121], measurements of the Weyl potential cannot disentangle

GBD from CQ, as in both scenarios we have the following Poisson-like relation,[1]

$$k^2(\Phi + \Psi) = -8\pi G\rho\delta\,. \tag{4.5}$$

This shows that the Weyl potential is directly related to the evolution of density fluctuations and is consequently subject to the same degeneracy found with measurements of the growth of structure. Note that modified gravity models other than GBD can lead to modifications in Eq. (4.5) and consequently can be distinguished from a dark fifth force through measurements of weak lensing. However, the opposite statement is not true: models with a dark fifth force always leave Eq. (4.5) unchanged and thus cannot be distinguished from a GBD modification of gravity using weak lensing.

4.1.4   The setup for the analysis

In the following, we will show that the two types of modifications can be disentangled using gravitational redshift, which provides a direct measurement of the potential Ψ appearing in the Euler equation. For the purpose of this demonstration, we adopt the symmetron model [111, 116, 127, 34], in which the modifications become important only at late cosmological times, above a given value of the scale factor $a_\star$. The time evolution of $\tilde{\beta}_{1,2}$ and $m_{1,2}$ in this model is given by

$$\tilde{\beta}(a) = \beta_\star\sqrt{1 - \left(\frac{a_\star}{a}\right)^3}\,, \tag{4.6}$$

$$m(a) = m_\star\sqrt{1 - \left(\frac{a_\star}{a}\right)^3}\,, \tag{4.7}$$

for $a > a_\star$. We fix $a_\star = 0.5$ for both scenarios and study the constraints on the parameters β_{*1} and β_{*2} for different values of the masses that set the Compton wavelength of the scalar field.

4.2   Observables

We consider three observables to constrain the GBD and CQ models: galaxy clustering, weak lensing, and the CMB.

---

[1]This assumes that $A^2 \approx 1$ in the GBD action in Eq. (C.1), which is required for the screening mechanism to be effective [112]. As discussed in Appendix C, this assumption has no impact on the arguments presented.

4.2.1 Galaxy clustering

Spectroscopic galaxy surveys provide a measurement of the galaxy number counts fluctuations,

$$\Delta^{gal}(\hat{\mathbf{n}}, z) \equiv \frac{N(\hat{\mathbf{n}}, z) - \bar{N}(z)}{\bar{N}(z)}, \tag{4.8}$$

where N is the number of galaxies in a pixel centered in direction $\hat{\mathbf{n}}$ and at redshift z, and $\bar{N}$ denotes the average number of galaxies inside the pixel. The observable Δ can be expressed within linear perturbation theory as [146, 147, 148]

$$\begin{aligned}
\Delta^{gal}(\hat{\mathbf{n}}, z) = {} & b\delta - \frac{1}{\mathcal{H}}\partial_r(\mathbf{V} \cdot \hat{\mathbf{n}}) + \frac{1}{\mathcal{H}}\partial_r\Psi + \frac{1}{\mathcal{H}}\dot{\mathbf{V}} \cdot \hat{\mathbf{n}} \\
& + \left(1 - 5s + \frac{5s - 2}{\mathcal{H}r} - \frac{\dot{\mathcal{H}}}{\mathcal{H}^2} + f^{\mathrm{evol}}\right)\mathbf{V} \cdot \hat{\mathbf{n}},
\end{aligned} \tag{4.9}$$

where r denotes the comoving distance to the galaxies, b is the galaxy bias, s is the magnification bias and f^{evol} is the evolution bias. The dominant contribution to Δ arises from the first two terms, which respectively encode the effect of matter density perturbations and RSD [102]. These are the only two contributions that are measurable with current data. The other terms are relativistic corrections suppressed on sub-horizon scales by a factor of $\mathcal{H}/k$, including the Doppler terms and the gravitational redshift effect given by the radial derivative of Ψ.[2]

We can extract information from $\Delta^{gal}(\hat{\mathbf{n}}, z)$ by measuring its two-point correlation function $\xi \equiv \langle \Delta^{gal}(\hat{\mathbf{n}}, z)\Delta^{gal}(\hat{\mathbf{n}}', z')\rangle$. The density and RSD terms in Eq. (4.9) generate three even multipoles in the correlation function: a monopole, a quadrupole and a hexadecapole, which probe the growth of structure and are the key quantities measured in a standard RSD analysis. Relativistic corrections to these three multipoles have been shown to be negligible, being suppressed by $(\mathcal{H}/k)^2$ relative to the density and RSD contributions [149]. One can however exploit the anti-symmetry generated by relativistic effects. This is manifested in the presence of odd multipoles, most notably a dipole, when cross-correlating two different populations of galaxies [151, 152, 153, 154, 155, 156]. Since the dipole is sensitive to the effect of gravitational redshift, which is suppressed by only a single power of $\mathcal{H}/k$, measuring it can help to disentangle modified gravity from a dark fifth force, as we show below.

The cross-correlation between two populations of galaxies with different luminosities—a bright and faint sample labelled B and F, respectively—generates the following even

---

[2]Note that Δ^{gal} is also affected by other relativistic effects suppressed by $(\mathcal{H}/k)^2$ and by gravitational lensing, whose impact is negligible in the redshift range considered in this work [149, 150].

multipoles in the flat-sky approximation:

$$\xi_0^{\mathrm{BF}}(z,d) = \frac{1}{2\pi^2}\int \mathrm{d}k\, k^2 \left[b_{\mathrm{B}}b_{\mathrm{F}}P_{\delta\delta} + \frac{1}{5}\left(\frac{1}{\mathcal{H}}\right)^2 P_{\theta\theta} \right.$$
$$\left. - \frac{1}{3}(b_{\mathrm{B}}+b_{\mathrm{F}})\left(\frac{1}{\mathcal{H}}\right)P_{\delta\theta}\right]j_0(kd)\,, \tag{4.10}$$

$$\xi_2^{\mathrm{BF}}(z,d) = -\frac{1}{2\pi^2}\int \mathrm{d}k\, k^2 \left[-\frac{2}{3}(b_{\mathrm{B}}+b_{\mathrm{F}})\left(\frac{1}{\mathcal{H}}\right)P_{\delta\theta} \right.$$
$$\left. + \frac{4}{7}\left(\frac{1}{\mathcal{H}}\right)^2 P_{\theta\theta}\right]j_2(kd)\,, \tag{4.11}$$

$$\xi_4^{\mathrm{BF}}(z,d) = \frac{1}{2\pi^2}\int \mathrm{d}k\, k^2 \left[\frac{8}{35}\left(\frac{1}{\mathcal{H}}\right)^2 P_{\theta\theta}\right]j_4(kd)\,. \tag{4.12}$$

Here, j_ℓ denotes the spherical Bessel function of order ℓ and $P_{\delta\delta}, P_{\theta\theta}$ and $P_{\delta\theta}$ are the auto- and cross-power spectra, which depend on k and z. The velocity divergence θ is defined in Fourier space by $\mathbf{V} = i(\mathbf{k}/k^2)\,\theta$. The dipole is given by

$$\xi_1^{\mathrm{BF}}(z,d) = -\frac{1}{2\pi^2}\int \mathrm{d}k\, k^2 \left[\frac{(b_{\mathrm{B}}-b_{\mathrm{F}})}{\mathcal{H}}\left(kP_{\delta\Psi} - \frac{P_{\delta\dot\theta}}{k}\right)\right.$$
$$\left. -(b_{\mathrm{B}}\alpha_{\mathrm{F}}-b_{\mathrm{F}}\alpha_{\mathrm{B}})\frac{P_{\delta\theta}}{k} + \frac{3}{5}(\alpha_{\mathrm{B}}-\alpha_{\mathrm{F}})\frac{P_{\theta\theta}}{\mathcal{H}k}\right]j_1(kd)$$
$$ -\frac{1}{5\pi^2}\int \mathrm{d}k\, k^2 \frac{d}{r}\left(\frac{1}{\mathcal{H}}\right)(b_{\mathrm{B}}-b_{\mathrm{F}})P_{\delta\theta}(k,z)j_2(kd)\,, \tag{4.13}$$

where as a shorthand we have defined

$$\alpha_{\mathrm{B,F}} \equiv 1 - 5s_{\mathrm{B,F}} + \frac{5s_{\mathrm{B,F}}-2}{r\mathcal{H}} - \frac{\dot{\mathcal{H}}}{\mathcal{H}^2} + f_{\mathrm{B,F}}^{\mathrm{evol}}\,. \tag{4.14}$$

The first term in Eq. (4.13), proportional to $P_{\delta\Psi}$, is the contribution from gravitational redshift. This key term is not present in the even multipoles and provides the information needed to disentangle the GBD and CQ scenarios. The last term in Eq. (4.13) is a wide-angle correction, which is needed for a consistent treatment of the dipole [157].[3] Note that anti-symmetry can only be probed by cross-correlating distinct populations, meaning that the dipole signal is nonzero only for $\mathrm{B} \neq \mathrm{F}$.

4.2.2 Weak lensing

Weak lensing can be measured through cosmic shear. Here, we consider both shear-shear correlations and shear-clustering correlations (also called galaxy-galaxy lensing), both of

---

[3]Note that wide-angle corrections also enter the even multipoles, but can be neglected since they are more suppressed compared to those in the dipole [158, 151].

which can be written in terms of the density power spectrum $P_{\delta\delta}$ by employing Eq. (4.5). We can safely neglect the covariance between the lensing observables and the spectroscopic galaxy clustering sample, since the lensing correlations are largely insensitive to the small radial modes from which the growth of structure and gravitational redshift are measured [159].

4.2.3 CMB

We consider the CMB temperature and polarization angular power spectra (TT, TE and EE). We are interested in scenarios in which the deviations from ΛCDM appear at late cosmological times, leaving the physics at the time of last scattering unchanged. Therefore, the role of the CMB observables in this analysis is primarily to constrain the standard cosmological parameters.

In addition to this, there are also the secondary CMB anisotropies. In particular, we note that late-time modifications to the growth of cosmic structure can impact the CMB on large scales through the integrated Sachs-Wolfe (ISW) effect. Moreover, the temperature and polarization spectra we employ in this analysis are affected by gravitational lensing. Since both ISW and gravitational lensing depend on the Weyl potential, we can use Eq. (4.5) to relate these terms to the density power spectrum $P_{\delta\delta}$, thus providing constraints on β_{*1} and β_{*2}. However, this does not give any contribution in discriminating between the two types of modifications, and, for this reason, we do not include separate measurements of the CMB lensing potential.

4.3 Numerical analysis

4.3.1 The general approach

In order to quantify the degeneracy between the GBD and CQ scenarios and assess the ability of gravitational redshift to break it, we use `MGCAMB` [31, 32, 33, 34], a modified gravity patch of the Boltzmann code `CAMB` [35, 160]. We employ `Cobaya` [161, 39] to carry out an MCMC analysis of the mock data set consisting of the observables described in Sec. 4.2. As a first step, we generate the mock data for a given fiducial model involving one kind of modification only, for example CQ with $\beta_{*2} = 1$ and fixed mass m_{*2}. We then perform a fit of the data allowing for both β_{*1} and β_{*2} to vary, fixing $m_{*1} = m_{*2}$.[4] The resulting constraints will either indicate the presence of a degeneracy or the lack thereof: if the two configurations $\{\beta_{*1} = 0, \beta_{*2} \neq 0\}$ and $\{\beta_{*1} \neq 0, \beta_{*2} = 0\}$ provide an equally good fit, we can conclude that the data cannot distinguish between the two scenarios. On the

---

[4]Note that by simultaneously varying both β_{*1} and β_{*2}, we are not claiming that we live in a universe where both gravity modifications and a dark fifth force are present. Rather, this approach is necessary to determine which models can be constrained by the data, without arbitrarily excluding one of the modifications.

other hand, if the case $\{\beta_{*1} \neq 0, \beta_{*2} = 0\}$ is excluded, the two kinds of modifications can be disentangled from one another, breaking the degeneracy.

For each data vector, we perform two types of analysis to assess the degeneracy between the two models: one where we do not include the dipole in the clustering data in Eq. (4.15), *i.e.* there are no constraints from gravitational redshift, and another one where the dipole is included. We build a multivariate Gaussian likelihood for the combination of the three observables and adopt wide uniform priors on the free parameters.

In each analysis, we have 11 free parameters: 5 cosmological parameters, with fiducial values $\omega_b = 0.02242$, $\omega_c = 0.12$, $h = 0.677$, $A_s = 2.105 \times 10^{-9}$, and $n_s = 0.9665$; 4 bias parameters related to the galaxy populations (defined in Appendix D); and 2 parameters associated with GBD and CQ, β_{*1} and β_{*2}, see Eq. (4.6). Since the mass of the scalar field is strongly degenerate with the coupling and thus cannot be separately constrained [34], we fix it to the same value in both scenarios, $m_{*1} = m_{*2}$, and run our analysis for different choices of the Compton wavelength $\lambda_* \equiv 1/m_*$.

4.3.2 Data vector specifications

Galaxy clustering

The galaxy clustering data vector consists of the following eight multipoles:

$$\mathbf{D} = \left(\xi_0^{\mathrm{BB}}, \xi_0^{\mathrm{BF}}, \xi_0^{\mathrm{FF}}, \xi_1^{\mathrm{BF}}, \xi_2^{\mathrm{BB}}, \xi_2^{\mathrm{BF}}, \xi_2^{\mathrm{FF}}, \xi_4^{\mathrm{TT}} \right). \tag{4.15}$$

This includes the usual even multipoles of RSD and importantly, also the dipole ξ_1^{BF}. Note that we only consider the hexadecapole in the total population of galaxies (labelled T), as Eq. (4.12) does not contain a dependence on population-specific biases so that considering different galaxy samples does not provide additional information. We compute the multipoles in Fourier space from power spectra generated using `MGCAMB` and perform the transform to configuration space using the FFTLog method [162].

Since the dipole is too small to be measured from current data [153], we perform the forecasts assuming a SKA2-like survey, for which the dipole is expected to reach a signal-to-noise ratio of 80 [163]. We consider the specifications of Ref. [144] for the number density, sky coverage and galaxy bias. The separations considered in this work range from $d = 20\,h^{-1}\mathrm{Mpc}$ to $d = 160\,h^{-1}\mathrm{Mpc}$, an interval where nonlinear corrections were found to be negligible for the dipole [164]. Furthermore, we assume a bias difference of 1 between the bright and faint galaxy populations, in agreement with that measured in Ref. [153]. More details on the modelling of the galaxy bias and the magnification bias can be found in Appendix D.

We use the data vector covariance calculated in Appendix C of Ref. [165], which includes both shot noise and cosmic variance. We account for the covariance between different separations and different multipoles, but neglect the one between different redshift bins, since

the bins are quite wide and do not overlap thanks to the spectroscopic precision of the redshift measurements.

Gravitational lensing

For gravitational lensing, we consider the specifications of the Dark Energy Survey (DES) Year-1 [94, 95] and compute the shear-shear correlations and the galaxy-galaxy lensing correlations using `MGCAMB`. Since `MGCAMB` is based on linear perturbation theory, we impose the "aggressive" scale cut implemented in Ref. [33] to effectively remove the data in the nonlinear regime. This is more restrictive than the cut used in the DES analysis for the ΛCDM model [94], since in our case it would be incorrect to follow the same approach and assume the validity of GR to model the observables on mildly nonlinear scales. All nuisance parameters, including intrinsic alignment, lens photo-z shift, source photo-z shift and shear calibration are fixed according to the DES Year 1 standard values [94, 95].

Note that by the time SKA2 data will be available, more precise measurements of weak lensing will have been performed by Euclid[5] and LSST[6]. However, we do not include these in our forecasts, since weak lensing cannot break the degeneracy between GBD and CQ, as discussed in Sec. 4.1.3.

CMB

For the CMB power spectra, we consider the Planck specifications introduced in Ref. [166], using the 143 GHz channel parameter values to compute the noise of the measurement [31]. The cosmic variance is computed according to Refs. [167, 168].

4.4   Results

4.4.1   Breaking the degeneracy

In Fig. 4.1, we show the marginalized constraints on β_{*1} and β_{*2} for a CQ fiducial model with $\beta_{*2} = 1$, $\lambda_* = 10$ Mpc, a combination that is not excluded by current data, see Ref. [34]. The blue contours correspond to the analysis without the dipole, *i.e.* without gravitational redshift, while the red contours include it. As expected, when the dipole is not present, we obtain a perfect elliptic degeneracy between β_{*1} and β_{*2}, which matches the analytical expectation discussed in Sec. 4.1.2. This means that even though no gravity modifications were included in the mock data vector, the data (RSD, weak lensing, and CMB) are equally well described using either the (correct) CQ model or the GBD one.

---

[5] `https://www.esa.int/Science_Exploration/Space_Science/Euclid`

[6] `https://www.lsst.org/`
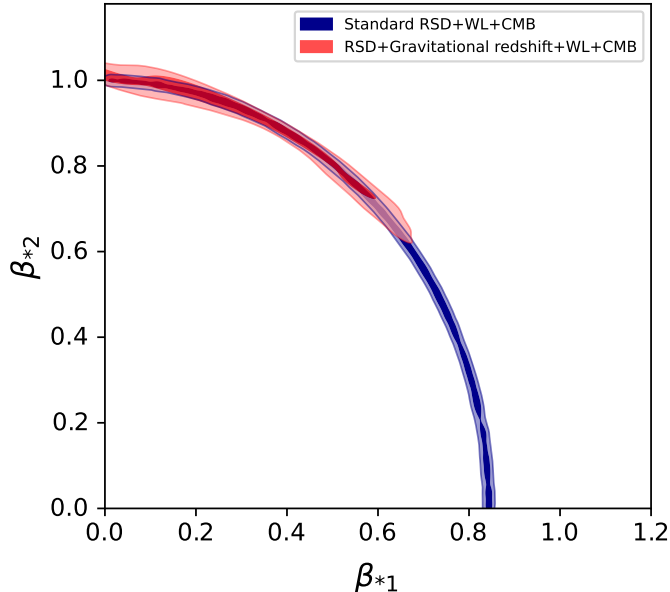
Figure 4.1: Marginalized 1σ and 2σ contours on β_{*1} and β_{*2}, with and without gravitational redshift. Here, the fiducial model is CQ and is specified by $\beta_{*2} = 1$ and $\lambda_* = 10$ Mpc (with $\beta_{*1} = 0$). The inclusion of gravitational redshift allows us to exclude GBD and thus break the degeneracy between modified gravity and a fifth force.

In the GBD case, the best fit is around $\beta_{*1} = 0.84$ and not $\beta_{*1} = 1$. This reflects the fact that the impact of a dark fifth force with coupling strength $\beta_{*2} = 1$ on the growth of cosmic structure can be mimicked by a modification of gravity with smaller coupling $\beta_1 = (\rho_c/\rho)(\delta_c/\delta)^{1/2}\beta_2 \simeq (\rho_c/\rho)^{3/2}\beta_2 \simeq 0.84\,\beta_2$, as can be seen from Eqs. (4.3)-(4.4) with our choice of fiducial cosmological parameters. This degeneracy has important consequences when jointly analyzing RSD, weak lensing and CMB data: if CDM is subject to additional interactions, such modifications in the dark sector could be incorrectly interpreted as evidence for modified gravity, even though GR remains valid.

The inclusion of gravitational redshift into the analysis decisively breaks the degeneracy between the two models. Indeed, we can clearly see that the red contours exclude the case $\beta_{*2} = 0$, indicating that a pure modification of gravity no longer fits the data. Even with the dipole, a large portion of the parameter space is still allowed, implying that models with both a dark fifth force and a modification of gravity are not excluded. However, such scenarios involving both kinds of modifications would be disfavoured according to the Occam's razor. An alternative representation of the constraints in polar coordinates is presented in Appendix E.
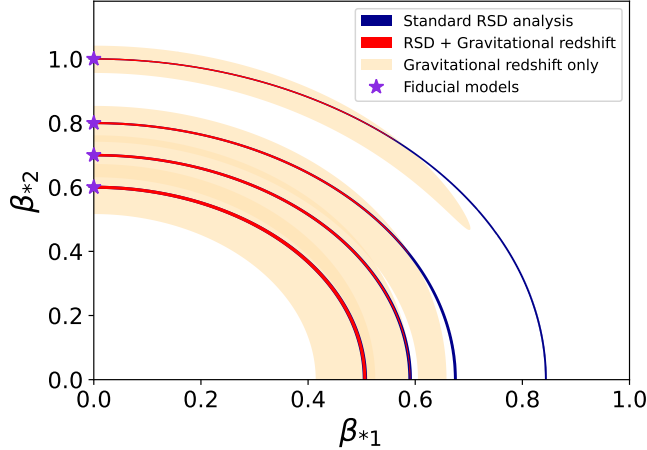
Figure 4.2: The 1σ confidence regions for four different fiducial values of the CQ coupling β_{*2}. For all fiducial models (indicated by stars) we set $\lambda_* = 10$ Mpc. All parameters except for β_{*1} and β_{*2} have been fixed to their fiducial values.

4.4.2   Varying the coupling strength

As a next step, we investigate how small the CQ parameter β_{*2} can be for the two models to be distinguishable with a SKA2-like survey. In Fig. 4.2, we present the constraints on various fiducial models with fixed $\lambda_* = 10\,\mathrm{Mpc}$ and different values of β_{*2}. To reduce the computational cost of the analysis, we fix the cosmological parameters to their fiducial values, and perform a likelihood minimization analysis only considering the spectroscopic galaxy sample. The CMB and weak lensing data are essential in constraining the cosmological parameters, but the constraints on β_{*1} and β_{*2} are driven by RSD and gravitational redshift.

We show the results including the RSD data only (in blue), the dipole only (in yellow) and the combination of the two (in red). Since the cosmological parameters are fixed, the contours are now artificially much tighter than in Fig. 4.1, but the degeneracy is perfectly captured and we obtain a very good qualitative agreement with Fig. 4.1 for the corresponding fiducial model. We notice that the case $\beta_{*2} = 0.7$ is at the edge of the region where the addition of the dipole can exclude a pure GBD scenario, whereas this observable does not give any additional information for the fiducial model with $\beta_{*2} = 0.6$. This means that if there is a fifth force acting on CDM with a coupling $\beta_{*2} \leq 0.6$, we will clearly detect the modifications with a survey like SKA2, but we will not be able to determine whether they are due to a dark fifth force or a modification of gravity. On the other hand, if the coupling is larger, the dipole will be able to discriminate between the two scenarios.
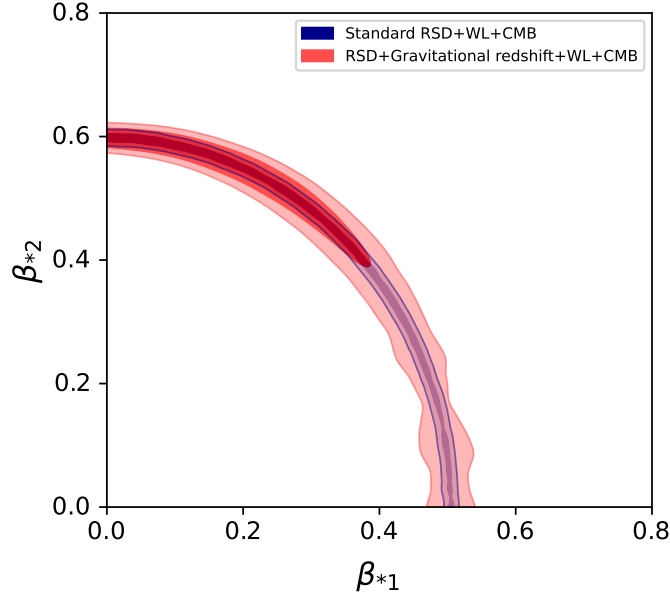
Figure 4.3: As in Fig. 4.1, but for fiducial parameters $\beta_{*2} = 0.6$ and $\lambda_* = 100$ Mpc (with $\beta_{*1} = 0$). The inclusion of gravitational redshift allows us to exclude GBD at 1σ.

4.4.3 Varying the Compton wavelength

In Figs. 4.1 and 4.2, we have fixed the value of λ_* to 10 Mpc. Since λ_* governs the Compton wavelength of the force mediated by the scalar field, a larger value of this parameter would generate modifications in the clustering observables at larger scales. In Fig. 4.3, we show the constraints on mock data generated for a CQ fiducial model with $\beta_{*2} = 0.6$ and $\lambda_* = 100$ Mpc, where we see that the dipole is able to break the degeneracy between the two models at the 1σ level. This is due to the fact that, for $\lambda_* = 100$ Mpc, this observable is significantly modified at large scales when $\beta_{*2} = 0.6$, contrary to the previous case with $\lambda_* = 10$ Mpc, where the modifications are very small for this value of β_{*2}.

4.4.4 The range of validity of our results

All the results presented so far concern GR models with a dark fifth force acting on CDM. Since the situation is symmetric, the same conclusions also apply in the case of GBD modified gravity with no CDM interactions. In this case, the elliptic degeneracy without gravitational redshift will be such that mock data generated by a GBD model with $\beta_{*1} = 1$ can be well described by a CQ scenario with $\beta_2 \simeq (\rho_c/\rho)^{-3/2} \simeq 1.19$. Including gravitational redshift allows us to distinguish between the two scenarios down to $\beta_{*1} \simeq 0.7$ for $\lambda_* = 10$ Mpc.

Finally, for the dipole to be helpful in this analysis, let us briefly discuss two quantities that impact the aforementioned thresholds in β_{*1} and β_{*2}. First, the bias difference between the correlated galaxy populations directly governs the amplitude of the gravitational redshift

contribution, which in turn determines the ability of the dipole to discriminate between the models. Here, we have assumed a bias difference of 1, consistent with the measurements from BOSS [153]. The population of galaxies detected by SKA2 may significantly differ from that of BOSS, possibly leading to a smaller bias difference. However, it is possible to boost this difference by exploring different ways to divide the galaxies into two populations, for example performing density splits based on their environment, which can increase the amplitude of the gravitational redshift contribution [169, 170].

Secondly, the range of scales considered in the analysis also has an influence on the role played by the dipole. Here, we have adopted a minimum separation of $20\,h^{-1}\mathrm{Mpc}$, since at such scales nonlinear effects are expected to have a small impact on the dipole in GR [164]. The situation may be slightly different in modified gravity. We checked that if the minimum separation is raised to $32\,h^{-1}\mathrm{Mpc}$, the constraining power of the dipole slightly decreases, leading to wider contours. As a consequence, the limiting values for β_{*1} and β_{*2} obtained in Sec. 4.4.2 would become somewhat larger, but the main message of our work would remain unchanged.

Chapter 5

Extending MGCAMB tests of gravity to nonlinear scales

In this Chapter, we present a new extension of MGCAMB, based on the halo model reaction (HMR) method, allowing for modelling the nonlinear growth of cosmic structures in alternative gravity models. In what follows, we introduce the HMR method in Sec. 5.1, describe the implementation of the HMR in `MGCAMB` in Sec. 5.2, and demonstrate its use in Sec. 5.3.

5.1 Modelling the effect of nonlinearities on the matter power spectrum

In this section, we introduce the HMR method and the corresponding computational tool, `ReACT`[1].

5.1.1 The halo model reaction method

In order to use the information from nonlinear scales for constraining models beyond ΛCDM, one needs to modify the standard halo model. To model the effect of nonlinearities one can introduce a *reaction function* $\mathcal{R}(k, z)$ defined as [75]

$$\mathcal{R}(k, z) \equiv \frac{P_{\mathrm{NL}}(k, z)}{P_{\mathrm{L}}(k, z) + P_{1h}^{\mathrm{pseudo}}(k, z)} \, ,$$
(5.1)

where $P_{\mathrm{NL}}(k, z)$ is the nonlinear spectrum for the targeted modified cosmology. The denominator is the nonlinear 'pseudo' spectrum, which is defined as a ΛCDM spectrum whose linear clustering matches the modified cosmology at the targeted redshift z, i.e.

$$P_{\mathrm{L}}^{\mathrm{pseudo}}(k, z) = P_{\mathrm{L}}^{\mathrm{MG}}(k, z) \, .$$
(5.2)

---

[1] `https://github.com/nebblu/ACTio-ReACTio`

In Eq. (5.1) we have implicitly assumed the halo model to construct the pseudo spectrum, where we have separated the 2-halo, or linear, spectrum $P_{\mathrm{L}}(k, z)$, and the 1-halo spectrum, $P_{1h}^{\mathrm{pseudo}}(k, z)$.

Based on the approach in Refs. [171, 76, 77], the reaction function can be computed using:

$$\mathcal{R}(k) = \frac{(1 - f_v)^2 \, P_{\mathrm{HM}}^{(\mathrm{cb})}(k) + 2 f_v \, (1 - f_v) \, P_{\mathrm{HM}}^{(\mathrm{cb}v)}(k) + f_v^2 P_{\mathrm{L}}^{(v)}(k)}{P_{\mathrm{HM}}^{\mathrm{pseudo}}(k, z)} \,, \tag{5.3}$$

where 'HM' represents the halo model, 'cb' denotes cold dark matter and baryons, 'v' denotes massive neutrinos, and $f_v = \Omega_{v,0}/\Omega_{\mathrm{m},0}$ being the ratio of energy density fractions of massive neutrinos to total matter today. In Eq. (5.3), the total halo model matter power spectrum is constructed from the weighted sum of individual components in the presence of massive neutrinos [172]. The $P_{\mathrm{HM}}^{(\mathrm{cb}v)}(k)$ stands for the cross power spectrum between neutrinos and the other two matter components, defined as

$$P_{\mathrm{HM}}^{(\mathrm{cb}v)}(k) \approx \sqrt{P_{\mathrm{HM}}^{(\mathrm{cb})}(k) P_{\mathrm{L}}^{(v)}(k)} \,, \tag{5.4}$$

and $P_{\mathrm{HM}}^{(\mathrm{cb})}$ is given by [173, 77]

$$P_{\mathrm{HM}}^{(\mathrm{cb})}(k) = \left[(1 - \mathcal{E}) e^{-k/k_\star} + \mathcal{E} \right] P_{\mathrm{L}}^{(\mathrm{cb})}(k) + P_{1h}^{(\mathrm{cb})}(k) \,. \tag{5.5}$$

The relevant parameters are given by

$$\mathcal{E}(z) = \qquad \lim_{k \to 0} \frac{(1 - f_v)^2 P_{1h}^{(\mathrm{cb})}(k, z)}{P_{1h}^{\mathrm{pseudo}}(k, z)} \,, \tag{5.6}$$

$$k_\star(z) = \quad -\bar{k} \left(\ln \left[\frac{A_1(\bar{k}, z) \pm A_2(\bar{k}, z)}{(1 - f_v)^2 P_{\mathrm{L}}^{(\mathrm{cb})}(\bar{k}, z) \left(1 - \mathcal{E}(z) \right)} \right] \right)^{-1} \,, \tag{5.7}$$

with $A_1(k, z)$ and $A_2(k, z)$ expressed as

$$A_1(k, z) = f_v^2 P_{\mathrm{L}}^{(v)}(k, z) + P_{\mathrm{HM}}^{\mathrm{pseudo}}(k, z) \mathcal{R}_{\mathrm{SPT}}(k, z)$$
$$- (1 - f_v)^2 \left[\mathcal{E}(z) P_{\mathrm{L}}^{(\mathrm{cb})}(k, z) + P_{1h}^{(\mathrm{cb})}(k, z) \right] \,, \tag{5.8}$$

$$A_2(k, z) = 2\sqrt{f_v^2 P_{\mathrm{HM}}^{\mathrm{pseudo}}(k, z) P_{\mathrm{L}}^{(v)}(k, z) \mathcal{R}_{\mathrm{SPT}}(k, z)} \,, \tag{5.9}$$

respectively. $\mathcal{R}_{\mathrm{SPT}}(k, z)$ is the 1-loop standard perturbation theory (SPT) prediction for the reaction function, which characterizes the quasi-nonlinear scales well, and is used to calibrate the halo model reaction to better predict this transitory regime in the presence of modifications to gravity. Typically SPT has a good accuracy in the range $0.01 < k \, \mathrm{Mpc} \, h^{-1} < 0.1$, whereas the nonlinear regime is typically considered to be given by $k > 0.1 \, h \, \mathrm{Mpc}^{-1}$ for late time structure formation. This latter regime can be more accurately predicted by $P_{1h}^{(\mathrm{cb})}(k)$.

5.1.2 The nonlinear phenomenological parameterization

Since we need to compute the matter power spectrum, a natural starting point is the Poisson equation describing the relation between gravitational metric potentials and matter density contrast. In linear perturbation theory, which is the default framework of MGCAMB, we have the modified equations given by Eqs. (2.98) and (2.99). These can be extended to describe perturbations on smaller cosmological scales, which can be generally separated into quasi-nonlinear scales and fully nonlinear scales. Namely, [77]

$$k^2 \Psi_{\mathrm{QNL}} = -4\pi G \mu(a, k) a^2 \rho_m \delta_{\mathrm{QNL}}(k, a) + S(k, a), \tag{5.10}$$

$$k^2 \Psi_{\mathrm{NL}}(k, a) = -4\pi G [1 + \mathcal{F}(k, a)] a^2 \rho_m \delta_{\mathrm{NL}}(k, a), \tag{5.11}$$

where the labels QNL and NL denote 'quasi-nonlinear' and 'nonlinear', respectively. $S(k, a)$ is the source term that contains the 2nd-order and 3rd-order contributions in perturbation theory that describes the additional modifications on quasi-nonlinear scales. The function $\mathcal{F}(k, a)$ in the second equation captures the fully nonlinear modification to the Poisson equation.

In [77], two different approaches were proposed for deriving quantitative prediction for δ_{NL}, and the relation between the function μ and the nonlinear modification $\mathcal{F}(k, a)$: the parameterized post-Friedmannian framework [174] and a simpler phenomenological parameterization that we will adopt below. The latter approach has the benefit of being simple, having only a few free parameters, while still being able to reproduce the nonlinear effects in representative modified gravity theories.

In the phenomenological parameterization, the function $\mathcal{F}(k, a)$ is taken to be the error function (Erf). The error function was shown to reflect the general profile of the effective gravitational constant in a variety of modified gravity theories [77], and allows for a smooth transition from the unscreened to the screened regime. The specific form is taken to be

$$\mathcal{F}_{\mathrm{Erf}} = \mathrm{Erf} \left[a y_{\mathrm{h}} 10^{\bar{J}} \right] \times (1 - \mu(\hat{k}, a)), \tag{5.12}$$

in which

$$\hat{k} = \frac{10^{p_4}}{a^2 y_{\mathrm{h}} R_{\mathrm{th}}}, \tag{5.13}$$

$$\bar{J} = p_1 - p_2 \log(R_{\mathrm{th}}) + p_3 \log(a y_{\mathrm{env}}), \tag{5.14}$$

where $y_{\mathrm{h}} = (R_{\mathrm{th}}/a)/(R_{\mathrm{i}}/a_{\mathrm{i}})$, R_{th} being the comoving halo top-hat radius and the subscript 'i' stands for initial time. y_{env} is the normalised radius of the environment. Note that, if $\mu \sim 1$ in the GR limit, $1 + \mathcal{F}_{\mathrm{Erf}} \sim 1$, and the nonlinear correction to modified perturbations also disappears. There are four additional nonlinear regime parameters: p_1 - p_4 introduced in this framework that represent typical MG phenomenological effects. Namely, p_1 param-

eterizes the strength of screening, p_2 and p_3 characterize the mass dependency and the environment dependency, respectively, and p_4 sets the Yukawa suppression scale [175]. The QNL correction, described by $S(k, a)$, was shown in [77] to have a negligible effect for scale-independent MG theories, while it can have up to a 2% effect on the power spectrum for the Hu-Sawicki $f(R)$ model. We will ignore the QNL correction in the current implementation.

5.2 The nonlinear extension and other upgrades of MGCAMB

As mentioned earlier, the effect of nonlinearities on the matter power spectrum can be captured using the reaction function. In what follows, we describe how `ReACT` [176], a publicly available code for computing the reaction function, can be used with `MGCAMB`. We also describe the other upgrades implemented in the latest version of `MGCAMB` and `MGCobaya` [177].

5.2.1 MGCAMB with ReACT

Since both `ReACT` and `MGCAMB` come with Python wrappers, making them work together amounts to establishing an appropriate Python interface. As mentioned in Sec. 5.1.2, the nonlinear modfication function $\mathcal{F}(k, a)$ depends on the linear modification $\mu(k, a)$, which is specified for the models implemented `MGCAMB`, namely, the generic scalar-tensor, $f(R)$, Planck and DES parameterizations, etc. We need to implement the same models in the part of `ReACT` that calculates μ. To achieve this, we create a new "case", labeled 14, in addition to existing cases in the default `ReACT` repository [176]. Then, we use a wrapper function to pass the parameters of the $\mu(k, a)$ functions from `MGCAMB` to `ReACT`. Since `ReACT` can also output the modified linear power spectrum $P(k)$, we conduct consistency checks between `MGCAMB` and `ReACT` to validate our implementation. As a representative case, we compare the linear power spectra for the DES parameterization, defined as: [43]

$$\mu = 1 + \mu_0 \frac{\Omega_{\mathrm{DE}}(a)}{\Omega_{\mathrm{DE},0}}, \tag{5.15}$$

$$\Sigma = 1 + \Sigma_0 \frac{\Omega_{\mathrm{DE}}(a)}{\Omega_{\mathrm{DE},0}}, \tag{5.16}$$

where μ_0 and Σ_0 are the present values of μ and Σ, respectively, and $\Omega_{\mathrm{DE}}(a) = \rho_{\mathrm{DE}}/\rho_{\mathrm{tot}}$. As can be seen from Fig. 5.1, we find a good agreement between the two codes.

We also implement the dynamical dark energy options, including the cubic-spline parameterization of the dark energy density [50, 51, 34], to make it possible to use `ReACT` with the full range of models implemented in MGCAMB.

In `MGCAMB`, we use the function call `compute_reaction_nu_ext`, which is an option in the Python interface of `ReACT`, to compute the reaction function with the contribution of massive neutrinos. As input, this function requires three types of linear power spectra: $P_{\mathrm{MG}}^{\mathrm{total}}(k)$, $P_{\mathrm{MG}}^{\mathrm{cb}}(k)$ and $P_{\Lambda\mathrm{CDM}}^{\mathrm{cb}}(k)$, under the assumption of the ΛCDM background, which can be
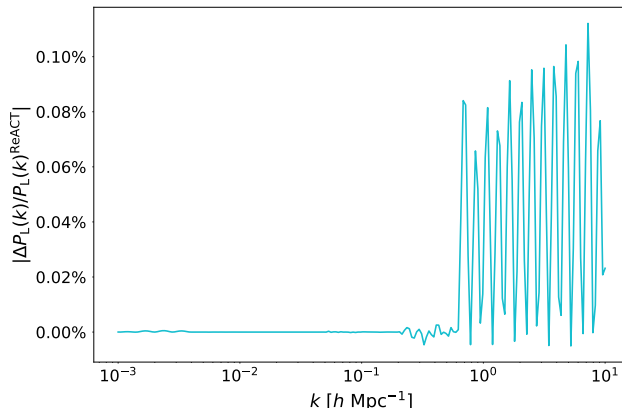
Figure 5.1: The relative difference in modified linear matter power spectra at $z = 0$ computed using `MGCAMB` and `ReACT` for the DES parametrization with $\mu_0 = 0.4$ and $\Sigma_0 = 0.1$.

easily computed by `MGCAMB`. Besides, we add a new function named `get_react_function` into the nonlinear Python module of `MGCAMB` to return the result of the reaction function and get `MGCAMB` to compute the pseudo power spectrum $P_{\rm HM}^{\rm pseudo}(k, z)$ in Eq. 5.3. We then adopt the commonly-used interpolator function in `CAMB` and `MGCAMB` to get the fully nonlinear power spectrum $P_{\rm NL}(k, z)$.

Currently, `ReACT` can only provide nonlinear corrections for the matter power spectrum and not the Weyl potential $W = (\Phi + \Psi)/2$. Thus, $P_{WW}(k)$ and $P_{W\delta}(k)$, needed for interpreting data from weak lensing surveys, must be calculated separately. We assume that the relation between W and δ is the same as the one on linear scales and is given by Eq. (2.99). With this assumption, we can compute $P_{WW}(k)$ and $P_{W\delta}(k)$ from the matter power spectrum $P_{\delta\delta}(k)$.

In addition to the parameters of the functions μ and Σ, we have four parameters, p_1 - p_4, specifying the nonlinear correction. In what follows, we simply take p_1 as the only parameter for the nonlinear regime, setting the others to zero, as was also done in [80]. This is justified for our example using the DES parameterization (where μ only depends on time), since for scale-independent MG models the screening has no environmental or halo mass dependence and, hence, no dependence on p_2 or p_3. Also, there is no Yukawa suppression, and hence no dependence on p_4, in models with no scale-dependence. We have observed that varying p_1 in the case of the DES parameterization results in up to $\sim 10\%$ percent differences in the $z = 0$ nonlinear power spectrum, for $\mu_0 = 0.4$ and $\Sigma_0 = 0.1$, as shown by Fig. 5.2. The limit $p_1 \rightarrow \infty$ corresponds to no screening and the limit $p_1 \rightarrow -\infty$ corresponds to a strong screening where the power spectrum goes back to the ΛCDM prediction.

The current version of `ReACT` is limited to making predictions up to redshift $z = 2.5$, which is good enough to account for nonlinear modification effects at late times. On the other hand, the redshift bins in the DES likelihood go to slighly higher redshifts. To maintain
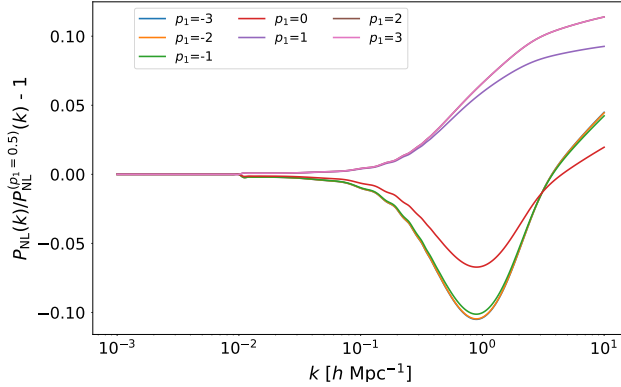
Figure 5.2: The relative difference in the nonlinear matter power spectrum $P_{\mathrm{NL}}(k)$ with different values of p_1 with respect to the case of $p_1 = 0.5$ for the DES parametrization with $\mu_0 = 0.4$ and $\Sigma_0 = 0.1$.

a relatively smooth transition from low to high redshifts, we adopt the $P^{\mathrm{pseudo}}(k, z)$ for redshifts above $z = 2.5$ without losing much of precision, since the majority of the modified nonlinear correction effects are focused on the redshifts below $z = 2.5$. Fig. 5.3 shows the smooth transition of output $P(k, z)$ from low to high redshifts for several representative k modes.

5.2.2   Other upgrades

In addition to the nonlinear extension, we have added a few other features to `MGCAMB` and `MGCobaya` to aid cosmological tests of gravity.

Galaxy-Weyl correlation in the DES Year-1 likelihood

The DES Year-1 likelihood, as implemented in Cobaya, computes the galaxy-Weyl correlation from the galaxy-galaxy correlation using the standard equations of GR relating density contrast $\delta = \delta\rho/\rho$ and W. In order to use the likelihood to constrain modifications of Einstein's equations, including the possibility of $\Sigma \neq 1$, we have modified the DES Year-1 likelihood implementation in MGCobaya to compute $P_{W\delta}(k)$ within `MGCAMB` together with $P_{WW}(k)$ and $P_{\delta\delta}(k)$.

Implementation of the DES Year-3 likelihood in Cobaya

We follow the formulation for calculating the weak lensing observables as described in [64] to implement the DES Year-3 likelihood in `Cobaya`. For the lens sample, we follow the treatment in [64]. Specifically, we choose the MagLim sample [178], which contains six tomographic redshift slices with nominal edges at $z = [0.20, 0.40, 0.55, 0.70, 0.85, 0.95, 1.05]$,
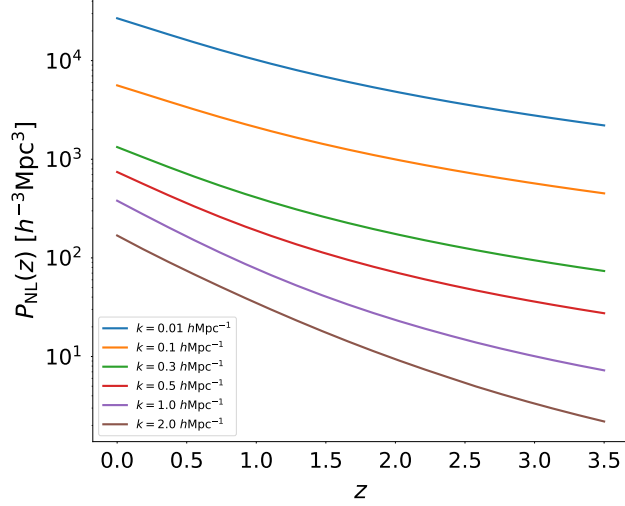
Figure 5.3: The modified matter power spectrum $P(k, z)$ as a function of redshift for several representative values of k for the DES parametrization with $\mu_0 = 0.4, \Sigma_0 = 0.1$, and $p_1 = 0.5$.

as the lens galaxy sample. We remove the two highest redshift MagLim bins from our analysis, as [179] revealed issues with the sample at $z > 0.85$.

Regarding the intrinsic alignments (IA) model used in the likelihood, we use the nonlinear alignment (NLA) model which is consistent with the DES Collaboration's study of modified gravity constraints form their Year-3 data [64], but not the same as the model (tidal alignment and tidal torquing, TATT) used in their constraints on the ΛCDM model [179].

The two-point angular correlation functions for the separation θ are computed as,

$$
\begin{aligned}
w^i(\theta) &= \sum_\ell \frac{2\ell + 1}{4\pi} P_\ell(\cos\theta) C^{ii}_{\delta_g \delta_g}(\ell) \,, \\
\gamma_t^{ij}(\theta) &= \sum_\ell \frac{2\ell + 1}{4\pi} \frac{P_\ell^2(\cos\theta)}{\ell(\ell+1)} C^{ij}_{\delta_g \mathrm{E}}(\ell) \,, \\
\xi_\pm^{ij}(\theta) &= \sum_{\ell \geqslant 2} \frac{2\ell + 1}{4\pi} \frac{2(G^+_{\ell,2}(\cos\theta) \pm G^-_{\ell,2}(\cos\theta))}{\ell^2(\ell+1)^2} \\
&\quad \times [C^{ij}_{\mathrm{EE}}(\ell) \pm C^{ij}_{\mathrm{BB}}(\ell)] \,,
\end{aligned}
\tag{5.17}
$$

where i, j denote two different redshift slices, P_ℓ is the Legendre polynomials of order ℓ, P_ℓ^m is the associated Legendre polynomial, and the functions $G^{+/-}_{\ell,m}(x)$ are combinations of the associated Legendre polynomials $P_\ell^m(x)$ and $P_{\ell-1}^m(x)$ given explicitly in Eq. (4.19) of [180].

The angular power spectra $C(\ell)$ in Eqs. (5.17) receive contributions from the galaxy density (δ_g), gravitational shear (κ), intrinsic alignments (I), cosmic magnification (mag)

and redshift space distortions (RSD). Specifically,

$$
\begin{aligned}
C_{\mathrm{EE}}^{ij}(\ell) =& C_{\kappa\kappa}^{ij}(\ell) + C_{\kappa \mathrm{I_E}}^{ij}(\ell) + C_{\kappa \mathrm{I_E}}^{ji}(\ell) + C_{\mathrm{I_E I_E}}^{ij}(\ell)\,, \\
C_{\mathrm{BB}}^{ij}(\ell) =& C_{\mathrm{I_B I_B}}^{ij}\,, \\
C_{\delta_{\mathrm{obs}}\mathrm{E}}^{ij}(\ell) =& C_{\delta_{\mathrm{g}}\kappa}^{ij}(\ell) + C_{\delta_{\mathrm{g}}\mathrm{I_E}}^{ij}(\ell) + C_{\delta_{\mathrm{mag}}\kappa}^{ij}(\ell) + C_{\delta_{\mu}\mathrm{I_E}}^{ij}(\ell)\,, \\
C_{\delta_{\mathrm{obs}}\delta_{\mathrm{obs}}}^{ii}(\ell) =& C_{\delta_{\mathrm{g}}\delta_{\mathrm{g}}}^{ii}(\ell) + C_{\delta_{\mathrm{mag}}\delta_{\mathrm{mag}}}^{ii}(\ell) + C_{\delta_{\mathrm{RSD}}\delta_{\mathrm{RSD}}}^{ii}(\ell) \\
& + 2C_{\delta_{\mathrm{g}}\delta_{\mathrm{mag}}}^{ii}(\ell) + 2C_{\delta_{\mathrm{g}}\delta_{\mathrm{RSD}}}^{ii}(\ell) + 2C_{\delta_{\mathrm{RSD}}\delta_{\mathrm{mag}}}^{ii}(\ell)\,.
\end{aligned}
\tag{5.18}
$$

The exact expression for the angular clustering power spectrum between two galaxy fields A, B is

$$
\begin{aligned}
C_{\mathrm{AB}}^{ij}(\ell) =& \frac{2}{\pi} \int d\chi_1\, W_A^i(\chi_1) \int d\chi_2\, W_B^j(\chi_2) \\
& \int \frac{dk}{k} k^3 P_{AB}(k, \chi_1, \chi_2) j_\ell(k\chi_1) j_\ell(k\chi_2)\,,
\end{aligned}
\tag{5.19}
$$

with P_{AB} being the corresponding three-dimensional power spectrum, and the kernels $W_{\mathrm{A,B}}^{ij}$ contain relevant contributions mentioned above.

For the level of sensitivity of the DES measurements on the shear-shear (C_{EE}, C_{BB}) and galaxy-shear ($C_{\delta_{\mathrm{obs}}\mathrm{E}}$) spectra, one can evaluate them efficiently using the Limber approximation [97], namely,

$$
C_{AB}^{ij}(\ell) = \int d\chi \frac{W_A^i(\chi) W_B^j(\chi)}{\chi^2} P_{AB}\left(k = \frac{\ell + \frac{1}{2}}{\chi}, z(\chi)\right),
\tag{5.20}
$$

for which $P_{W\delta}$, $P_{WW}(k)$ and $P_{\delta\delta}(k)$ are computed within `MGCAMB`, as in the case of the DES Year-1 likelihood described in Sec. 5.2.2.

However, the galaxy-galaxy spectrum ($C_{\delta_{\mathrm{g}}\delta_{\mathrm{g}}}$) is measured better than the shear-shear and galaxy-shear spectra, and the Limber approximation fails to provide the theory prediction with the required precision. Therefore we evaluate $C_{\delta_{\mathrm{g}}\delta_{\mathrm{g}}}$ using the exact formula in Eq. (5.19). To be efficient, we follow the method described in [181] to calculate the double-Bessel integral in Eq. (5.19) with the FFTLog algorithm.

We have created wrapper functions for μ, γ, and Σ in the Python interface of `MGCAMB`, making it convenient to test the time evolution of these phenomenological functions at a given Fourier number k for all implemented modified gravity models.

Synchronization with `CAMB`

The current version of `MGCAMB`[2] is now forked with `CAMB`[3] on GitHub, making it convenient to keep it consistent with future upgrades of `CAMB`.

5.3 Demonstrations

To demonstrate the use of the nonlinear extension of `MGCAMB`, we adopt the DES parametrization, to make it easy to compare to the previous results in the literature.

Parameters	Flat Prior	Fiducial
μ_0	(-0.2,1.2)	0.4
Σ_0	(-0.2,0.4)	0.1
p_1	(-2,2)	0.5
$\Omega_b h^2$	-	0.112
$\Omega_c h^2$	-	0.0226
n_s	-	0.969
$\ln(10^{10} A_s)$	-	3.06
$100\,\theta_{\mathrm{MC}}$	-	1.0410
τ	-	0.067
$\Sigma\,m_\nu$	-	0.06

Table 5.1: The fiducial values and the range of flat priors used for the MG and cosmological parameters in the tests using the synthetic DES-like data.

	NL ext + DES baseline	no NL ext + aggressive cut	NL ext + aggressive cut
μ_0	0.393 ± 0.046	0.392 ± 0.097	0.393 ± 0.098
Σ_0	0.100 ± 0.012	0.110 ± 0.015	0.102 ± 0.016

Table 5.2: The mean values and the 68% CL uncertainties for μ_0 and Σ_0 recovered from the synthetic data with and without the nonlinear extension (NL ext), while applying the aggressive linear cut. Results show that the nonlinear extension does not impact constraints derived from linear scales.

First, we perform a test on mock data, generating synthetic DES-like galaxy-galaxy, galaxy-lensing and lensing-lensing (3×2pt) correlations for a fiducial model with $\mu_0 = 0.4, \Sigma_0 = 0.1$ and $p_1 = 0.5$, and assuming a ΛCDM background expansion. As our "data" covariance, we adopt the covariance matrix from the DES Year-1 likelihood rescaled down by a factor of 25 as the actual DES Year-1 covariance would not allow us to constrain the nonlinear parameter p_1. We then run MCMC chains using `MGCobaya` [177] to see if we can recover the input model. We vary μ_0 and Σ_0, and also p_1 when the nonlinear extension is

---

[2]`https://github.com/sfu-cosmo/MGCAMB`

[3]`https://github.com/cmbant/CAMB`

applied, with the priors given in Tab. 5.1. The other cosmological parameters are fixed to the fiducial values specified in Tab. 5.1, and the DES likelihood parameters are fixed at the standard values of DES Year-1 [43, 95], to help us isolate the impact of using the nonlinear extension.

As mentioned earlier, the DES 3×2pt data includes information from nonlinear scales. For their Year-1 constraints of the ΛCDM model [43], the DES collaboration applied a conservative cut to keep only scales that can be reliably modelled with Halofit. We will refer to the DES 3×2pt data with this conservative cut as "DES baseline". In earlier `MGCAMB` studies that used DES data, an additional "aggressive" cut was applied [33] to eliminate all nonlinear scales, as `MGCAMB` was unable to model them until now.

In what follows, we compare the case of using the baseline DES-like data with the nonlinear extension of `MGCAMB` to the case without the nonlinear extension and applying the aggressive linear cut.

As a first test, we compare the results with and without the nonlinear extension, while applying the agressive cut in both cases. As shown in Fig. 5.4 and Table 5.2, the recovered constraints on the parameters μ_0 and Σ_0 are consistent with each other and with the fiducial model, demonstrating that nonlinear corrections do no impact the linear scales.
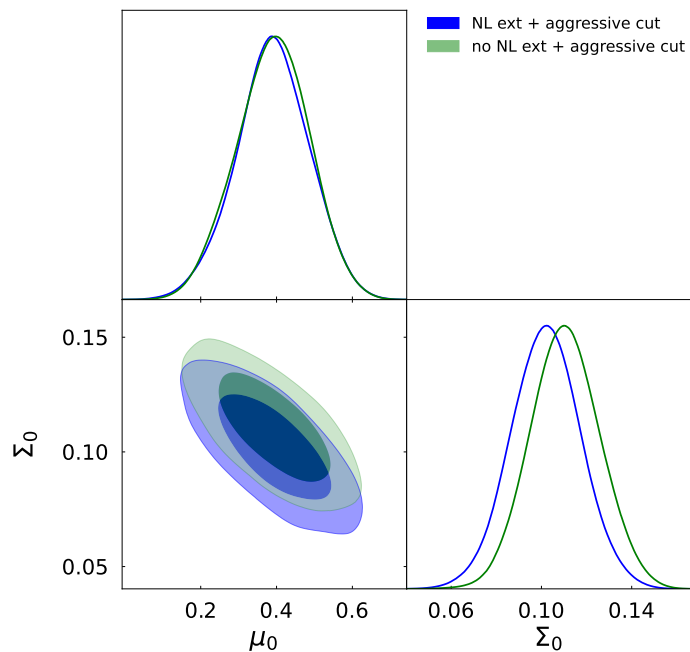
Figure 5.4: Joint 68% and 95% CL constraints on μ_0 and Σ_0 obtained from the synthetic data with and without the nonlinear extension (NL ext), while applying the aggressive linear cut in both cases. Results show that the nonlinear extension does not impact constraints derived from linear scales.

As our next test, we compare the case of using the nonlinear extension in `MGCAMB` along with the baseline DES-like synthetic data to the case without the nonlinear extension and

	DES Y3 baseline + PBRS	DES Y3 with linear cut + PBRS
μ_0	0.003 ± 0.201	-0.012 ± 0.216
Σ_0	0.016 ± 0.039	0.043 ± 0.045

Table 5.3: The mean values along with 68% CL uncertainties for μ_0 and Σ_0 obtained using the nonlinear extension with the DES Year-3 baseline data, and without the extension while using the linear cut. PBRS denotes the combination of Planck 2018, BAO, RSD, and SN Ia as detailed in Sec. 5.3.

applying the aggressive linear cut. The joint constraints on μ_0 and Σ_0 are shown in Fig. 5.5, along with the constraint on p_1 in the former case. It is clear that, in the case where the nonlinear extension and the baseline data are used, one obtains better constraints on μ_0 and Σ_0 even after marginalizing over p_1. The corresponding numbers are provided in Table 5.2, showing the 1σ uncertainty in μ_0 is reduced by a factor of 2.1 when the nonlinear extension is used, which is consistent with Fig. 3 of [80].
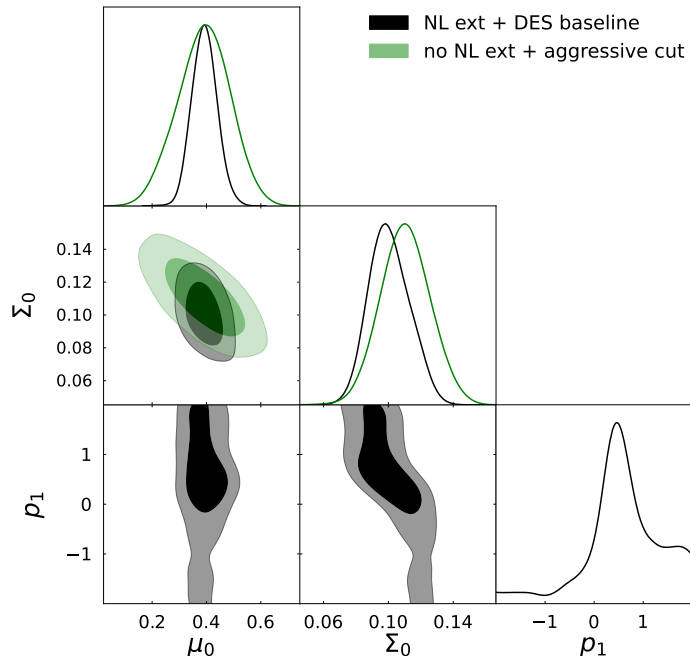
Figure 5.5: The comparison of constraints on μ_0 and Σ_0 between the case of using the baseline DES-like synthetic data with the nonlinear extension (NL ext) and the case with the aggressive cut (without the nonlinear extension).

Finally, we use `MGCAMB` with the nonlinear extension to derive constraints on μ_0 and Σ_0 from current cosmological datasets. We use the DES Year-3 3×2pt data [64], Planck 2018 CMB temperature, polarization and lensing spectra [132], joint measurements of baryon acoustic oscillations (BAO) and redshift-space distortions (RSD) from eBOSS DR16, the SDSS DR7 MGS data [133], the BAO measurement from 6dF [134], and the Pantheon sample of uncalibrated supernovae [104]. We compare the case of using the nonlinear extension

with the baseline DES Year-3 data to the case without the nonlinear extension and applying the linear cut. We used the same linear cut as the one adopted in the DES Year-3 constraints [64] on modified gravity models. From the posterior plots in Fig. 5.6, it is clear that one obtains stronger constraints on μ_0 and Σ_0 in the case with the nonlinear extension. There is practically no difference in the posteriors of μ_0, but the improvement in the constraint on Σ_0 is apparent. This is because a weak lensing survey like DES primarily constrains Σ. The corresponding numbers are provided in Table 5.3. The constraints obtained with a linear cut are consistent with those reported by the DES collaboration [64].
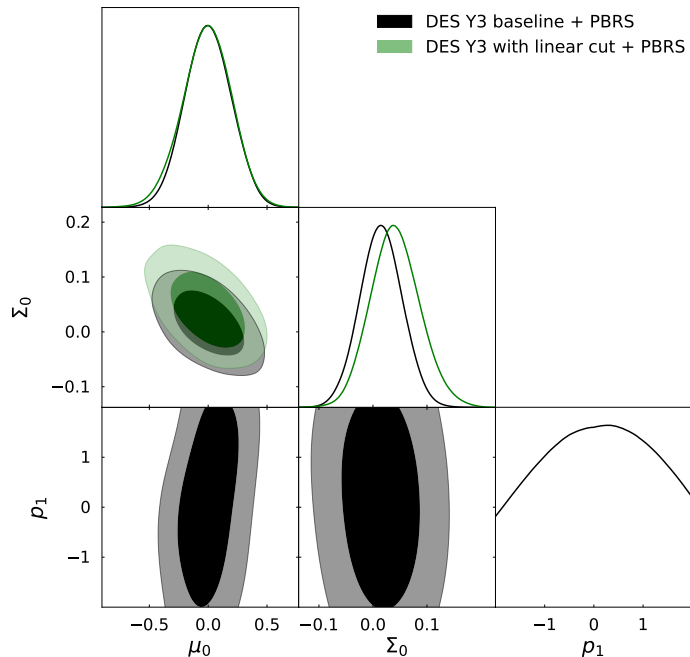

Figure 5.6: Constraints on μ_0 and Σ_0 obtained using the nonlinear extension and the baseline DES Year-3 data, and without the nonlinear extension and using the linear cut. PBRS denotes the combination of Planck 2018, BAO, RSD, and SN Ia as detailed in Sec. 5.3.

Chapter 6

Summary

This thesis began with an overview of the main ingredients of the current cosmological model and the types of observations available to cosmologists, with a particular focus on cosmological tests of gravity. We then introduced a commonly used phenomenological parameterisation for investigating modified gravity.

In Chapter 3, we presented `MGCAMB 2023`, which comes with tools for using it with `Cobaya` [37, 39, 40], as well as an implementation in the latest version of `CosmoMC` [37, 123, 38]. This new version includes several added features: new built-in models, *e.g.* a scalar field coupled only to dark matter in the quasi-static approximation; a direct implementation of the μ-Σ parameterization in the Einstein-Boltzmann solver, eliminating the need to convert to μ-γ; the option to include DE perturbations when working with $w \neq -1$ backgrounds; a new binned parameterization allowing for a simultaneous reconstruction of μ, Σ and Ω_X (the fractional dark energy density) as functions of redshift. For each of these we have provided detailed instructions on how to use it. In some cases, we have also provided a worked out example complete with fits to currently available cosmological data.

As we have shown in Chapter 4, combining RSD with gravitational lensing cannot distinguish a modification of gravity from additional forces acting on CDM. By performing an MCMC analysis, we have demonstrated that mock data generated by a coupled quintessence model with a fifth force acting on CDM is equally well fitted by a GBD modified gravity scenario. This means that, we may wrongly claim to have discovered a deviation from GR on cosmological scales, whereas in reality the modifications are due to new interactions in the dark sector (or vice versa). This ambiguity can be resolved by including the effect of gravitational redshift into the analysis. Thanks to its sensitivity to the temporal distortion Ψ of the metric, gravitational redshift combined with RSD directly probes the validity of the Euler equation for CDM. This provides an efficient way to discriminate between dark interactions and modifications of gravity. Here, we have quantified the constraining power of gravitational redshift by comparing a GBD modification of gravity with a CQ model, finding that modifications that are still in agreement with current constraints will be distinguishable by a future survey like SKA2. This is particularly remarkable, since measuring

gravitational redshift does not require new data, but can be simply achieved by augmenting the standard RSD analysis with the dipole generated in the cross-correlation of different galaxy samples.

In Chapter 5, we have extended `MGCAMB` to add capability to make predictions of modified gravity models for cosmological observables on scales where nonlinearities are important. The extension employed the halo model reaction method, with the reaction function computed using `ReACT` interfaced in the Python wrapper of `MGCAMB`. We have tested the nonlinear extension on a synthetic dataset based on a two-parameter phenomenological model, recovering the input fiducial parameters μ_0 and Σ_0. The mock test demonstrates that using the nonlinear extension with the baseline DES-like data improves constraints on μ_0 and Σ_0 relative to the case when a linear cut was applied. We then use the nonlinear extension to derive constraints on μ_0 and Σ_0 from a combination of current datasets that include the DES Year-3 data and find an enhancement in the constraints. The nonlinear extension of `MGCAMB` will enable using the a wider range of the data from the current and forthcoming cosmological surveys, including weak lensing surveys such as LSST and Euclid.

Bibliography

[1] B. P. Abbott et al. Observation of Gravitational Waves from a Binary Black Hole Merger. *Phys. Rev. Lett.*, 116(6):061102, 2016.

[2] S. Perlmutter et al. Measurements of Ω and Λ from 42 High Redshift Supernovae. *Astrophys. J.*, 517:565–586, 1999.

[3] Steven Weinberg. The Cosmological Constant Problem. *Rev. Mod. Phys.*, 61:1–23, 1989.

[4] C. P. Burgess. The Cosmological Constant Problem: Why it's hard to get Dark Energy from Micro-physics. In *100e Ecole d'Ete de Physique: Post-Planck Cosmology*, pages 149–197, 2015.

[5] Elcio Abdalla et al. Cosmology intertwined: A review of the particle physics, astrophysics, and cosmology associated with the cosmological tensions and anomalies. *JHEAp*, 34:49–211, 2022.

[6] Salvatore Capozziello, Sante Carloni, and Antonio Troisi. Quintessence without scalar fields. *Recent Res. Dev. Astron. Astrophys.*, 1:625, 2003.

[7] Sean M. Carroll, Vikram Duvvuri, Mark Trodden, and Michael S. Turner. Is cosmic speed - up due to new gravitational physics? *Phys. Rev. D*, 70:043528, 2004.

[8] Wayne Hu and Ignacy Sawicki. Models of f(R) Cosmic Acceleration that Evade Solar-System Tests. *Phys. Rev. D*, 76:064004, 2007.

[9] Levon Pogosian and Alessandra Silvestri. The pattern of growth in viable f(R) cosmologies. *Phys. Rev. D*, 77:023503, 2008. [Erratum: Phys.Rev.D 81, 049901 (2010)].

[10] G. R. Dvali, G. Gabadadze, and M. Porrati. Metastable gravitons and infinite volume extra dimensions. *Phys. Lett. B*, 484:112–118, 2000.

[11] Kazuya Koyama and Roy Maartens. Structure formation in the dgp cosmological model. *JCAP*, 01:016, 2006.

[12] Giulia Gubitosi, Federico Piazza, and Filippo Vernizzi. The Effective Field Theory of Dark Energy. *JCAP*, 02:032, 2013.

[13] Jolyon K. Bloomfield, Éanna É. Flanagan, Minjoon Park, and Scott Watson. Dark energy or modified gravity? An effective field theory approach. *JCAP*, 08:010, 2013.

[14] Jerome Gleyzes, David Langlois, Federico Piazza, and Filippo Vernizzi. Essential Building Blocks of Dark Energy. *JCAP*, 08:025, 2013.

[15] Jolyon Bloomfield. A Simplified Approach to General Scalar-Tensor Theories. *JCAP*, 12:044, 2013.

[16] Alessandra Silvestri, Levon Pogosian, and Roman V. Buniy. Practical approach to cosmological perturbations in modified gravity. *Phys. Rev. D*, 87(10):104015, 2013.

[17] Emilio Bellini and Ignacy Sawicki. Maximal freedom at minimum cost: linear large-scale structure in general modifications of gravity. *JCAP*, 07:050, 2014.

[18] Jérôme Gleyzes, David Langlois, and Filippo Vernizzi. A unifying description of dark energy. *Int. J. Mod. Phys. D*, 23(13):1443010, 2015.

[19] Jérôme Gleyzes, David Langlois, Michele Mancarella, and Filippo Vernizzi. Effective Theory of Interacting Dark Energy. *JCAP*, 08:054, 2015.

[20] Gregory Walter Horndeski. Second-order scalar-tensor field equations in a four-dimensional space. *Int. J. Theor. Phys.*, 10:363–384, 1974.

[21] C. Deffayet, Xian Gao, D. A. Steer, and G. Zahariade. From k-essence to generalised Galileons. *Phys. Rev. D*, 84:064039, 2011.

[22] Jérôme Gleyzes, David Langlois, Federico Piazza, and Filippo Vernizzi. Exploring gravitational theories beyond Horndeski. *JCAP*, 02:018, 2015.

[23] Jérôme Gleyzes, David Langlois, Federico Piazza, and Filippo Vernizzi. Healthy theories beyond Horndeski. *Phys. Rev. Lett.*, 114(21):211101, 2015.

[24] David Langlois and Karim Noui. Degenerate higher derivative theories beyond Horndeski: evading the Ostrogradski instability. *JCAP*, 02:034, 2016.

[25] Jibril Ben Achour, David Langlois, and Karim Noui. Degenerate higher order scalar-tensor theories beyond Horndeski and disformal transformations. *Phys. Rev. D*, 93(12):124005, 2016.

[26] Bin Hu, Marco Raveri, Noemi Frusciante, and Alessandra Silvestri. Effective Field Theory of Cosmic Acceleration: an implementation in CAMB. *Phys. Rev. D*, 89(10):103530, 2014.

[27] Bin Hu, Marco Raveri, Noemi Frusciante, and Alessandra Silvestri. EFT-CAMB/EFTCosmoMC: Numerical Notes v3.0. 5 2014.

[28] Marco Raveri, Bin Hu, Noemi Frusciante, and Alessandra Silvestri. Effective Field Theory of Cosmic Acceleration: constraining dark energy with CMB data. *Phys. Rev.*, D90(4):043513, 2014.

[29] Miguel Zumalacárregui, Emilio Bellini, Ignacy Sawicki, Julien Lesgourgues, and Pedro G. Ferreira. hi_class: Horndeski in the Cosmic Linear Anisotropy Solving System. *JCAP*, 08:019, 2017.

[30] Emilio Bellini, Ignacy Sawicki, and Miguel Zumalacárregui. hi_class: Background Evolution, Initial Conditions and Approximation Schemes. *JCAP*, 02:008, 2020.

[31] Gong-Bo Zhao, Levon Pogosian, Alessandra Silvestri, and Joel Zylberberg. Searching for modified growth patterns with tomographic surveys. *Phys. Rev. D*, 79:083513, 2009.

[32] Alireza Hojjati, Levon Pogosian, and Gong-Bo Zhao. Testing gravity with CAMB and CosmoMC. *JCAP*, 08:005, 2011.

[33] Alex Zucca, Levon Pogosian, Alessandra Silvestri, and Gong-Bo Zhao. MGCAMB with massive neutrinos and dynamical dark energy. *JCAP*, 05:001, 2019.

[34] Zhuangfei Wang, Seyed Hamidreza Mirpoorian, Levon Pogosian, Alessandra Silvestri, and Gong-Bo Zhao. New MGCAMB tests of gravity with CosmoMC and Cobaya. *JCAP*, 08:038, 2023.

[35] Antony Lewis, Anthony Challinor, and Anthony Lasenby. Efficient computation of CMB anisotropies in closed FRW models. *Astrophys. J.*, 538:473–476, 2000.

[36] `http://camb.info`.

[37] Antony Lewis and Sarah Bridle. Cosmological parameters from CMB and other data: A Monte Carlo approach. *Phys. Rev. D*, 66:103511, 2002.

[38] `http://cosmologist.info/cosmomc`.

[39] Jesus Torrado and Antony Lewis. Cobaya: Code for Bayesian Analysis of hierarchical physical models. *JCAP*, 05:057, 2021.

[40] `https://cobaya.readthedocs.io`.

[41] Fergus Simpson et al. CFHTLenS: Testing the Laws of Gravity with Tomographic Weak Lensing and Redshift Space Distortions. *Mon. Not. Roy. Astron. Soc.*, 429:2249, 2013.

[42] P. A. R. Ade et al. Planck 2015 results. XIV. Dark energy and modified gravity. *Astron. Astrophys.*, 594:A14, 2016.

[43] T. M. C. Abbott et al. Dark Energy Survey Year 1 Results: Constraints on Extended Cosmological Models from Galaxy Clustering and Weak Lensing. *Phys. Rev. D*, 99(12):123505, 2019.

[44] Ziad Sakr and Matteo Martinelli. Cosmological constraints on sub-horizon scales modified gravity theories with MGCLASS II. *JCAP*, 05(05):030, 2022.

[45] Jason N. Dossett, Mustapha Ishak, and Jacob Moldenhauer. Testing General Relativity at Cosmological Scales: Implementation and Parameter Correlations. *Phys. Rev. D*, 84:123001, 2011.

[46] Cristhian Garcia-Quintero, Mustapha Ishak, Logan Fox, and Jason Dossett. Testing deviations from GR at cosmological scales including dynamical dark energy, massive neutrinos, functional or binned parametrizations, and spatial curvature. *Phys. Rev. D*, 100(10):103530, 2019.

[47] Cristhian Garcia-Quintero and Mustapha Ishak. Singling out modified gravity parameters and data sets reveals a dichotomy between Planck and lensing. *Mon. Not. Roy. Astron. Soc.*, 506(2):1704–1714, 2021.

[48] Juan Espejo, Simone Peirone, Marco Raveri, Kazuya Koyama, Levon Pogosian, and Alessandra Silvestri. Phenomenology of Large Scale Structure in scalar-tensor theories: joint prior covariance of w_{DE}, Σ and μ in Horndeski. *Phys. Rev. D*, 99(2):023512, 2019.

[49] Levon Pogosian and Alessandra Silvestri. What can cosmology tell us about gravity? Constraining Horndeski gravity with Σ and μ. *Phys. Rev. D*, 94(10):104014, 2016.

[50] Levon Pogosian, Marco Raveri, Kazuya Koyama, Matteo Martinelli, Alessandra Silvestri, Gong-Bo Zhao, Jian Li, Simone Peirone, and Alex Zucca. Imprints of cosmological tensions in reconstructed gravity. *Nature Astron.*, 6(12):1484–1490, 2022.

[51] Marco Raveri, Levon Pogosian, Matteo Martinelli, Kazuya Koyama, Alessandra Silvestri, and Gong-Bo Zhao. Principal reconstructed modes of dark energy and gravity. *JCAP*, 02:061, 2023.

[52] Rennan Barkana. Possible interaction between baryons and dark-matter particles revealed by the first stars. *Nature*, 555(7694):71–74, 2018.

[53] J. A. Schewtschenko, C. M. Baugh, R. J. Wilkinson, C. Bœhm, S. Pascoli, and T. Sawala. Dark matter–radiation interactions: the structure of Milky Way satellite galaxies. *Mon. Not. Roy. Astron. Soc.*, 461(3):2282–2287, 2016.

[54] Roberta Diamanti, Elena Giusarma, Olga Mena, Maria Archidiacono, and Alessandro Melchiorri. Dark Radiation and interacting scenarios. *Phys. Rev. D*, 87(6):063509, 2013.

[55] Manuel A. Buen-Abad, Gustavo Marques-Tavares, and Martin Schmaltz. Non-Abelian dark matter and dark radiation. *Phys. Rev. D*, 92(2):023531, 2015.

[56] David N. Spergel and Paul J. Steinhardt. Observational evidence for selfinteracting cold dark matter. *Phys. Rev. Lett.*, 84:3760–3763, 2000.

[57] Valeria Pettorino, Luca Amendola, Carlo Baccigalupi, and Claudia Quercellini. Constraints on coupled dark energy using CMB data from WMAP and south pole telescope. *Phys.Rev.D*, 86(10), nov 2012.

[58] André A. Costa, Lucas C. Olivari, and E. Abdalla. Quintessence with Yukawa Interaction. *Phys.Rev.D*, 92(10):103501, 2015.

[59] Maria Archidiacono, Emanuele Castorina, Diego Redigolo, and Ennio Salvioni. Unveiling dark fifth forces with linear cosmology. *JCAP*, 10:074, 2022.

[60] Chris Blake et al. The WiggleZ Dark Energy Survey: the growth rate of cosmic structure since redshift z=0.9. *Mon. Not. Roy. Astron. Soc.*, 415:2876, 2011.

[61] Cullan Howlett, Ashley Ross, Lado Samushia, Will Percival, and Marc Manera. The clustering of the SDSS main galaxy sample – II. Mock galaxy catalogues and a measurement of the growth of structure from redshift space distortions at $z = 0.15$. *Mon. Not. Roy. Astron. Soc.*, 449(1):848–866, 2015.

[62] Shadab Alam et al. The clustering of galaxies in the completed SDSS-III Baryon Oscillation Spectroscopic Survey: cosmological analysis of the DR12 galaxy sample. *Mon. Not. Roy. Astron. Soc.*, 470(3):2617–2652, 2017.

[63] Shadab Alam et al. Completed SDSS-IV extended Baryon Oscillation Spectroscopic Survey: Cosmological implications from two decades of spectroscopic surveys at the Apache Point Observatory. *Phys. Rev. D*, 103(8):083533, 2021.

[64] T. M. C. Abbott et al. Dark Energy Survey Year 3 results: Constraints on extensions to ΛCDM with weak lensing and galaxy clustering. *Phys. Rev. D*, 107(8):083504, 2023.

[65] A. Pourtsidou, C. Skordis, and E. J. Copeland. Models of dark matter coupled to dark energy. *Phys. Rev. D*, 88(8):083505, 2013.

[66] Manuel A. Buen-Abad, Martin Schmaltz, Julien Lesgourgues, and Thejs Brinckmann. Interacting Dark Sector and Precision Cosmology. *JCAP*, 01:008, 2018.

[67] Salvatore Bottaro, Emanuele Castorina, Marco Costa, Diego Redigolo, and Ennio Salvioni. Unveiling Dark Forces with Measurements of the Large Scale Structure of the Universe. *Phys. Rev. Lett.*, 132(20):201002, 2024.

[68] Željko Ivezić et al. LSST: from Science Drivers to Reference Design and Anticipated Data Products. *Astrophys. J.*, 873(2):111, 2019.

[69] A. Blanchard et al. Euclid preparation. VII. Forecast validation for Euclid cosmological probes. *Astron. Astrophys.*, 642:A191, 2020.

[70] N. Frusciante et al. Euclid: Constraining linearly scale-independent modifications of gravity with the spectroscopic and photometric primary probes. 6 2023.

[71] A. Spurio Mancini and B. Bose. On the degeneracies between baryons, massive neutrinos and f(R) gravity in Stage IV cosmic shear analyses. 5 2023.

[72] R. E. Smith, J. A. Peacock, A. Jenkins, S. D. M. White, C. S. Frenk, F. R. Pearce, P. A. Thomas, G. Efstathiou, and H. M. P. Couchmann. Stable clustering, the halo model and nonlinear cosmological power spectra. *Mon. Not. Roy. Astron. Soc.*, 341:1311, 2003.

[73] Ryuichi Takahashi, Masanori Sato, Takahiro Nishimichi, Atsushi Taruya, and Masamune Oguri. Revising the Halofit Model for the Nonlinear Matter Power Spectrum. *Astrophys. J.*, 761:152, 2012.

[74] Alexander Mead, Samuel Brieden, Tilman Tröster, and Catherine Heymans. HMcode-2020: Improved modelling of non-linear cosmological power spectra with baryonic feedback. 9 2020.

[75] Matteo Cataneo, Lucas Lombriser, Catherine Heymans, Alexander Mead, Alexandre Barreira, Sownak Bose, and Baojiu Li. On the road to percent accuracy: non-linear reaction of the matter power spectrum to dark energy and modified gravity. *Mon. Not. Roy. Astron. Soc.*, 488(2):2121–2142, 2019.

[76] Benjamin Bose, Matteo Cataneo, Tilman Tröster, Qianli Xia, Catherine Heymans, and Lucas Lombriser. On the road to per cent accuracy IV: ReACT – computing the non-linear power spectrum beyond ΛCDM. *Mon. Not. Roy. Astron. Soc.*, 498(4):4650–4662, 2020.

[77] B. Bose, M. Tsedrik, J. Kennedy, L. Lombriser, A. Pourtsidou, and A. Taylor. Fast and accurate predictions of the nonlinear matter power spectrum for general models of Dark Energy and Modified Gravity. 10 2022.

[78] Sankarshana Srinivasan, Daniel B. Thomas, Francesco Pace, and Richard Battye. Cosmological gravity on all scales. Part II. Model independent modified gravity N-body simulations. *JCAP*, 06:016, 2021.

[79] Sankarshana Srinivasan, Daniel B. Thomas, and Richard Battye. Cosmological gravity on all scales. Part III. Non-linear matter power spectrum in phenomenological modified gravity. *JCAP*, 03:039, 2024.

[80] Maria Tsedrik, Benjamin Bose, Pedro Carrilho, Alkistis Pourtsidou, Sefa Pamuk, Santiago Casas, and Julien Lesgourgues. Stage-IV Cosmic Shear with Modified Gravity and Model-independent Screening. 4 2024.

[81] P. James Peebles. *The Large-Scale Structure of the Universe*. Princeton University Press, 11 1980.

[82] Eric V. Linder. Cosmic growth history and expansion history. *Phys. Rev. D*, 72:043529, 2005.

[83] Eric V. Linder and Robert N. Cahn. Parameterized Beyond-Einstein Growth. *Astropart. Phys.*, 28:481–488, 2007.

[84] James M. Bardeen. Gauge Invariant Cosmological Perturbations. *Phys. Rev. D*, 22:1882–1905, 1980.

[85] Wayne Hu, Uros Seljak, Martin J. White, and Matias Zaldarriaga. A complete treatment of CMB anisotropies in a FRW universe. *Phys. Rev. D*, 57:3290–3301, 1998.

[86] Chung-Pei Ma and Edmund Bertschinger. Cosmological perturbation theory in the synchronous and conformal Newtonian gauges. *Astrophys. J.*, 455:7–25, 1995.

[87] David Hilbert. Die Grundlagen der Physik. 1. *Gott. Nachr.*, 27:395–407, 1915.

[88] Matias Zaldarriaga and Uros Seljak. An all sky analysis of polarization in the microwave background. *Phys. Rev. D*, 55:1830–1840, 1997.

[89] Jean Kaplan, J. Delabrouille, P. Fosalba, and C. Rosset. Cmb polarization as complementary information to anisotropies. *Comptes Rendus Physique*, 4:917, 2003.

[90] C. Bennett et al. First year Wilkinson Microwave Anisotropy Probe (WMAP) observations: Foreground emission. *Astrophys. J. Suppl.*, 148:97, 2003.

[91] R. K. Sachs and A. M. Wolfe. Perturbations of a cosmological model and angular variations of the microwave background. *Astrophys. J.*, 147:73–90, 1967.

[92] Antony Lewis and Anthony Challinor. Weak gravitational lensing of the CMB. *Phys. Rept.*, 429:1–65, 2006.

[93] Scott Dodelson. *Modern Cosmology.* Academic Press, Amsterdam, 2003.

[94] T. M. C. Abbott et al. Dark Energy Survey year 1 results: Cosmological constraints from galaxy clustering and weak lensing. *Phys. Rev. D*, 98(4):043526, 2018.

[95] E. Krause et al. Dark Energy Survey Year 1 Results: Multi-Probe Methodology and Simulated Likelihood Analyses. 6 2017.

[96] S. Pandey et al. Dark Energy Survey year 3 results: Constraints on cosmological parameters and galaxy-bias models from galaxy clustering and galaxy-galaxy lensing using the redMaGiC sample. *Phys. Rev. D*, 106(4):043520, 2022.

[97] D. Nelson Limber. The Analysis of Counts of the Extragalactic Nebulae in Terms of a Fluctuating Density Field. II. *Astrophys. J.*, 119:655, 1954.

[98] Nick Kaiser. Weak gravitational lensing of distant galaxies. *Astrophys. J.*, 388:272, 1992.

[99] Nick Kaiser. Weak lensing and cosmology. *Astrophys. J.*, 498:26, 1998.

[100] Marilena LoVerde and Niayesh Afshordi. Extended Limber Approximation. *Phys. Rev. D*, 78:123506, 2008.

[101] Catherine Heymans et al. KiDS-1000 Cosmology: Multi-probe weak gravitational lensing and spectroscopic galaxy clustering constraints. *Astron. Astrophys.*, 646:A140, 2021.

[102] N. Kaiser. Clustering in real space and in redshift space. *Mon. Not. Roy. Astron. Soc.*, 227:1–27, 1987.

[103] C. Garcia-Quintero et al. HOD-Dependent Systematics in Emission Line Galaxies for the DESI 2024 BAO analysis. 4 2024.

[104] D. M. Scolnic et al. The Complete Light-curve Sample of Spectroscopically Confirmed SNe Ia from Pan-STARRS1 and Cosmological Constraints from the Combined Pantheon Sample. *Astrophys. J.*, 859(2):101, 2018.

[105] M. Betoule et al. Improved cosmological constraints from a joint analysis of the SDSS-II and SNLS supernova samples. *Astron. Astrophys.*, 568:A22, 2014.

[106] Stephen M. Merkowitz. Tests of Gravity Using Lunar Laser Ranging. *Living Rev. Rel.*, 13:7, 2010.

[107] James G. Williams, Slava G. Turyshev, and Dale H. Boggs. Progress in lunar laser ranging tests of relativistic gravity. *Phys. Rev. Lett.*, 93:261101, 2004.

[108] A. I. Vainshtein. To the problem of nonvanishing gravitation mass. *Phys. Lett. B*, 39:393–394, 1972.

[109] T. Damour and Alexander M. Polyakov. The String dilaton and a least coupling principle. *Nucl. Phys. B*, 423:532–558, 1994.

[110] Justin Khoury and Amanda Weltman. Chameleon fields: Awaiting surprises for tests of gravity in space. *Phys. Rev. Lett.*, 93:171104, 2004.

[111] Kurt Hinterbichler and Justin Khoury. Symmetron Fields: Screening Long-Range Forces Through Local Symmetry Restoration. *Phys. Rev. Lett.*, 104:231301, 2010.

[112] Austin Joyce, Bhuvnesh Jain, Justin Khoury, and Mark Trodden. Beyond the Cosmological Standard Model. *Phys. Rept.*, 568:1–98, 2015.

[113] Rachel Bean and Matipon Tangmatitham. Current constraints on the cosmic growth history. *Phys. Rev. D*, 81:083534, 2010.

[114] Edmund Bertschinger and Phillip Zukin. Distinguishing Modified Gravity from Dark Energy. *Phys. Rev. D*, 78:024015, 2008.

[115] T. Damour, G. W. Gibbons, and C. Gundlach. Dark Matter, Time Varying G, and a Dilaton Field. *Phys. Rev. Lett.*, 64:123–126, 1990.

[116] Philippe Brax, Anne-Christine Davis, Baojiu Li, and Hans A. Winther. A Unified Description of Screened Modified Gravity. *Phys. Rev. D*, 86:044015, 2012.

[117] Michel Chevallier and David Polarski. Accelerating universes with scaling dark matter. *Int. J. Mod. Phys. D*, 10:213–224, 2001.

[118] Eric V. Linder. Exploring the expansion history of the universe. *Phys. Rev. Lett.*, 90:091301, 2003.

[119] Jochen Weller and A. M. Lewis. Large scale cosmic microwave background anisotropies and dark energy. *Mon. Not. Roy. Astron. Soc.*, 346:987–993, 2003.

[120] Wenjuan Fang, Wayne Hu, and Antony Lewis. Crossing the Phantom Divide with Parameterized Post-Friedmann Dark Energy. *Phys. Rev. D*, 78:087303, 2008.

[121] Camille Bonvin and Levon Pogosian. Modified Einstein versus modified Euler for dark matter. *Nature Astron.*, 7(9):1127–1134, 2023.

[122] Seyed Hamidreza Mirpoorian, Zhuangfei Wang, and Levon Pogosian. On validity of the quasi-static approximation in scalar-tensor theories. *JCAP*, 07:069, 2023.

[123] Antony Lewis. Efficient sampling of fast and slow cosmological parameters. *Phys. Rev. D*, 87(10):103529, 2013.

[124] Luca Amendola et al. Cosmology and fundamental physics with the Euclid satellite. *Living Rev. Rel.*, 21(1):2, 2018.

[125] Bruno J. Barros, Luca Amendola, Tiago Barreiro, and Nelson J. Nunes. Coupled quintessence with a ΛCDM background: removing the σ_8 tension. *JCAP*, 01:007, 2019.

[126] Marco Baldi. Structure formation in Multiple Dark Matter cosmologies with long-range scalar interactions. *Mon. Not. Roy. Astron. Soc.*, 428:2074, 2013.

[127] Alireza Hojjati, Aaron Plahn, Alex Zucca, Levon Pogosian, Philippe Brax, Anne-Christine Davis, and Gong-Bo Zhao. Searching for scalar gravitational interactions in current and future cosmological data. *Phys. Rev. D*, 93(4):043531, 2016.

[128] Yuting Wang, Levon Pogosian, Gong-Bo Zhao, and Alex Zucca. Evolution of dark energy reconstructed from the latest observations. *Astrophys. J. Lett.*, 869:L8, 2018.

[129] Robert G. Crittenden, Levon Pogosian, and Gong-Bo Zhao. Investigating dark energy experiments with principal components. *JCAP*, 12:025, 2009.

[130] Robert G. Crittenden, Gong-Bo Zhao, Levon Pogosian, Lado Samushia, and Xinmin Zhang. Fables of reconstruction: controlling bias in the dark energy equation of state. *JCAP*, 02:048, 2012.

[131] R. R. Caldwell, Rahul Dave, and Paul J. Steinhardt. Cosmological imprint of an energy component with general equation of state. *Phys. Rev. Lett.*, 80:1582–1585, 1998.

[132] N. Aghanim et al. Planck 2018 results. V. CMB power spectra and likelihoods. *Astron. Astrophys.*, 641:A5, 2020.

[133] Ashley J. Ross, Lado Samushia, Cullan Howlett, Will J. Percival, Angela Burden, and Marc Manera. The clustering of the SDSS DR7 main Galaxy sample – I. A 4 per cent distance measure at $z = 0.15$. *Mon. Not. Roy. Astron. Soc.*, 449(1):835–847, 2015.

[134] Florian Beutler, Chris Blake, Matthew Colless, D. Heath Jones, Lister Staveley-Smith, Lachlan Campbell, Quentin Parker, Will Saunders, and Fred Watson. The 6df galaxy survey: baryon acoustic oscillations and the local hubble constant. *Monthly Notices of the Royal Astronomical Society*, 416(4):3017–3032, jul 2011.

[135] Gong-Bo Zhao et al. The completed SDSS-IV extended Baryon Oscillation Spectroscopic Survey: a multitracer analysis in Fourier space for measuring the cosmic structure growth and expansion rate. *Mon. Not. Roy. Astron. Soc.*, 504(1):33–52, 2021.

[136] Jiamin Hou et al. The Completed SDSS-IV extended Baryon Oscillation Spectroscopic Survey: BAO and RSD measurements from anisotropic clustering analysis of the Quasar Sample in configuration space between redshift 0.8 and 2.2. *Mon. Not. Roy. Astron. Soc.*, 500(1):1201–1221, 2020.

[137] Arnaud de Mattia et al. The Completed SDSS-IV extended Baryon Oscillation Spectroscopic Survey: measurement of the BAO and growth rate of structure of the emission line galaxy sample from the anisotropic power spectrum between redshift 0.6 and 1.1. *Mon. Not. Roy. Astron. Soc.*, 501(4):5616–5645, 2021.

[138] Helion du Mas des Bourboux et al. The Completed SDSS-IV Extended Baryon Oscillation Spectroscopic Survey: Baryon Acoustic Oscillations with Lyα Forests. *Astrophys. J.*, 901(2):153, 2020.

[139] Clare Burrage, Edmund J. Copeland, Christian Käding, and Peter Millington. Symmetron scalar fields: Modified gravity, dark matter, or both? *Phys. Rev. D*, 99(4):043539, 2019.

[140] Christian Käding. Lensing with Generalized Symmetrons. *Astronomy*, 2(2):128–140, 2023.

[141] Daniel Sobral-Blanco and Camille Bonvin. Measuring anisotropic stress with relativistic effects. *Phys. Rev. D*, 104(6):063516, 2021.

[142] Daniel Sobral-Blanco and Camille Bonvin. Measuring the distortion of time with relativistic effects in large-scale structure. *Mon. Not. Roy. Astron. Soc.*, 519(1):L39–L44, 2022.

[143] Albert Einstein. The foundation of the general theory of relativity. *Annalen Phys.*, 49(7):769–822, 1916.

[144] Philip Bull. Extending cosmological tests of General Relativity with the Square Kilometre Array. *Astrophys. J.*, 817(1):26, 2016.

[145] Sveva Castello, Nastassia Grimm, and Camille Bonvin. Rescuing constraints on modified gravity using gravitational redshift in large-scale structure. *Phys. Rev. D*, 106(8):083511, 2022.

[146] Camille Bonvin and Ruth Durrer. What galaxy surveys really measure. *Phys. Rev. D*, 84:063505, 2011.

[147] Anthony Challinor and Antony Lewis. The linear power spectrum of observed source number counts. *Phys. Rev. D*, 84:043516, 2011.

[148] Jaiyul Yoo, A. Liam Fitzpatrick, and Matias Zaldarriaga. A New Perspective on Galaxy Clustering as a Cosmological Probe: General Relativistic Effects. *Phys. Rev. D*, 80:083514, 2009.

[149] Goran Jelic-Cizmek, Francesca Lepori, Camille Bonvin, and Ruth Durrer. On the importance of lensing for galaxy clustering in photometric and spectroscopic surveys. *JCAP*, 04:055, 2021.

[150] F. Lepori et al. Euclid preparation. XIX. Impact of magnification on photometric galaxy clustering. *Astron. Astrophys.*, 662:A93, 2022.

[151] Camille Bonvin, Lam Hui, and Enrique Gaztanaga. Asymmetric galaxy correlation functions. *Phys. Rev. D*, 89(8):083535, 2014.

[152] Camille Bonvin. Isolating relativistic effects in large-scale structure. *Class. Quant. Grav.*, 31(23):234002, 2014.

[153] Enrique Gaztanaga, Camille Bonvin, and Lam Hui. Measurement of the dipole in the cross-correlation function of galaxies. *JCAP*, 01:032, 2017.

[154] Patrick McDonald. Gravitational redshift and other redshift-space distortions of the imaginary part of the power spectrum. *JCAP*, 11:026, 2009.

[155] Jaiyul Yoo, Nico Hamaus, Uros Seljak, and Matias Zaldarriaga. Going beyond the Kaiser redshift-space distortion formula: a full general relativistic account of the effects and their detectability in galaxy clustering. *Phys. Rev. D*, 86:063514, 2012.

[156] Rupert A. C. Croft. Gravitational redshifts from large-scale structure. *Mon. Not. Roy. Astron. Soc.*, 434:3008–3017, 2013.

[157] Camille Bonvin, Lam Hui, and Enrique Gaztanaga. Optimising the measurement of relativistic distortions in large-scale structure. *JCAP*, 08:021, 2016.

[158] Paulo H. F. Reimberg, Francis Bernardeau, and Cyril Pitrou. Redshift-space distortions with wide angular separations. *JCAP*, 01:048, 2016.

[159] Peter L. Taylor and Katarina Markovič. Covariance of photometric and spectroscopic two-point statistics: Implications for cosmological parameter inference. *Phys. Rev. D*, 106(6):063536, 2022.

[160] Cullan Howlett, Antony Lewis, Alex Hall, and Anthony Challinor. CMB power spectrum parameter degeneracies in the era of precision cosmology. *JCAP*, 04:027, 2012.

[161] Jesús Torrado and Antony Lewis. Cobaya: Bayesian analysis in cosmology. Astrophysics Source Code Library, record ascl:1910.019, October 2019.

[162] A. J. S. Hamilton. Uncorrelated modes of the nonlinear power spectrum. *Mon. Not. Roy. Astron. Soc.*, 312:257–284, 2000.

[163] Sveva Castello, Michele Mancarella, Nastassia Grimm, Daniel Sobral-Blanco, Isaac Tutusaus, and Camille Bonvin. Gravitational redshift constraints on the effective theory of interacting dark energy. *JCAP*, 05:003, 2024.

[164] Camille Bonvin, Francesca Lepori, Sebastian Schulz, Isaac Tutusaus, Julian Adamek, and Pablo Fosalba. A case study for measuring the relativistic dipole of a galaxy cross-correlation with the Dark Energy Spectroscopic Instrument. *Mon. Not. Roy. Astron. Soc.*, 525(3):4611–4627, 2023.

[165] Camille Bonvin and Pierre Fleury. Testing the equivalence principle on cosmological scales. *JCAP*, 05:061, 2018.

[166] G. Rocha, R. Trotta, C. J. A. P. Martins, A. Melchiorri, P. P. Avelino, R. Bean, and Pedro T. P. Viana. Measuring alpha in the early universe: cmb polarization, reionization and the fisher matrix analysis. *Mon. Not. Roy. Astron. Soc.*, 352:20, 2004.

[167] Martin J. White, Lawrence M. Krauss, and Joseph Silk. Inflation and the statistics of cosmic microwave background anisotropies: From 1-degree to COBE. *Astrophys. J.*, 418:535, 1993.

[168] K. W. Ng and A. D. Speliotopoulos. Calculation of cosmic variance in cosmic microwave background anisotropy. 1995.

[169] Enrique Paillas, Yan-Chuan Cai, Nelson Padilla, and Ariel G. Sánchez. Redshift-space distortions with split densities. *Mon. Not. Roy. Astron. Soc.*, 505(4):5731–5752, 2021.

[170] Florian Beutler and Enea Di Dio. Modeling relativistic contributions to the halo power spectrum dipole. *JCAP*, 07(07):048, 2020.

[171] Matteo Cataneo, J. D. Emberson, Derek Inman, Joachim Harnois-Deraps, and Catherine Heymans. On the road to per cent accuracy – III. Non-linear reaction of the matter power spectrum to massive neutrinos. *Mon. Not. Roy. Astron. Soc.*, 491(3):3101–3107, 2020.

[172] Shankar Agarwal and Hume A. Feldman. The effect of massive neutrinos on the matter power spectrum. *Mon. Not. Roy. Astron. Soc.*, 410:1647, 2011.

[173] Asantha Cooray and Ravi K. Sheth. Halo Models of Large Scale Structure. *Phys. Rept.*, 372:1–129, 2002.

[174] Lucas Lombriser. A parametrisation of modified gravity on nonlinear cosmological scales. *JCAP*, 11:039, 2016.

[175] Hideki Yukawa. On the Interaction of Elementary Particles I. *Proc. Phys. Math. Soc. Jap.*, 17:48–57, 1935.

[176] https://github.com/nebblu/ACTio-ReACTio.

[177] https://github.com/sfu-cosmo/MGCobaya.

[178] A. Porredon et al. Dark Energy Survey Year 3 results: Optimizing the lens sample in a combined galaxy clustering and galaxy-galaxy lensing analysis. *Phys. Rev. D*, 103(4):043503, 2021.

[179] T. M. C. Abbott et al. Dark Energy Survey Year 3 Results: Cosmological Constraints from Galaxy Clustering and Weak Lensing. 5 2021.

[180] Albert Stebbins. Weak lensing on the celestial sphere. 9 1996.

[181] Xiao Fang, Elisabeth Krause, Tim Eifler, and Niall MacCrann. Beyond Limber: Efficient computation of angular power spectra for galaxy clustering and weak lensing. *JCAP*, 05:010, 2020.

[182] Junpu Wang, Lam Hui, and Justin Khoury. No-Go Theorems for Generalized Chameleon Field Theories. *Phys. Rev. Lett.*, 109:241301, 2012.

Appendix A

Scalar field coupled to CDM

The action of a theory with a scalar field coupled to CDM can be written as

$$S = \int \mathrm{d}^4 x \sqrt{-g} \left[\frac{M_{\mathrm{Pl}}^2}{2} \mathcal{R} - \frac{1}{2} \partial_\mu \phi \partial^\mu \phi - V(\phi) \right.$$
$$\left. + \mathcal{L}_c \left(\psi_c, A^2(\phi) g_{\mu\nu} \right) + \mathcal{L}_{\mathrm{SM}} \left(\psi_{\mathrm{SM}}, g_{\mu\nu} \right) \right] \tag{A.1}$$

where $\mathcal{L}_{\mathrm{SM}}$ represents the Lagrangian density of the Standard Model of particle physics, which includes baryons and radiations, and $\mathcal{L}_c$ represents the Lagrangian density of dark matter. Here $M_{\mathrm{pl}} \equiv (8\pi G)^{-1/2}$ is the reduced Planck mass, and ϕ is the scalar field. The coupling of the scalar field to dark matter arises due to the conformal factor $A(\phi)$ that alters the gravitational metric felt by the CDM. Varying the action in Eq. (A.1) with respect to ϕ gives the equation of motion for ϕ,

$$\Box \phi = V_{,\phi} - \frac{A_{,\phi}}{A} T^c = V_{,\phi} + \frac{A_{,\phi}}{A} \rho_c \equiv V_{,\phi}^{\mathrm{eff}} \tag{A.2}$$

where $_{,\phi}$ is the derivative with respect to ϕ, $T^c = -\rho_c$ is the trace of the CDM stress-energy $T_{\mu\nu}^c$, and we have defined the effective potential V^{eff}. The Einstein's equation is obtained by varying the action with respect to $g_{\mu\nu}$:

$$G_{\mu\nu} = M_{\mathrm{Pl}}^{-2} \left[T_{\mu\nu}^{\mathrm{SM}} + T_{\mu\nu}^c + T_{\mu\nu}^\phi \right] , \tag{A.3}$$

where the stress-energy tensor of the standard matter is conserved, $\nabla^\mu T_{\mu\nu}^{\mathrm{SM}} = 0$, and so is the sum of the scalar field and the CDM stress-energies: $\nabla^\mu [T_{\mu\nu}^c + T_{\mu\nu}^\phi] = 0$, but $T_{\mu\nu}^c$ and $T_{\mu\nu}^\phi$ are not individually conserved. We have

$$\nabla^\mu T_{\mu\nu}^c = -\beta \rho_c \partial_\nu \phi , \tag{A.4}$$

where $\beta \equiv A_{,\phi}/A$.

Perturbing Eq. (A.4) to first order and transforming to Fourier space, yields the continuity and the Euler equations for CDM given by Eqs. (3.1) and (3.2). Also, perturbing Eq. (A.2)

to first order and taking the QSA, gives

$$\delta\phi = -\frac{\beta\rho_c\delta_c}{k^2/a^2 + m^2}, \tag{A.5}$$

where $m^2 \equiv V_{,\phi\phi}^{\text{eff}}$ evaluated at the minimum of the effective potential. Namely, when applying the QSA we assume that the scalar field is always at the minimum of V^{eff}. This allows us to eliminate the scalar field entirely from all equations.

The form of the Einstein equations is unchanged in this model, hence $\mu = \gamma = \Sigma = 1$. There is a contribution from the scalar energy density, $V_{,\phi}\delta\phi$, on the right hand side of the Poisson equation, which is negligible for the class of models for which our QSA is valid. However, we include it in the Poisson equation, after using (A.5), as

$$k^2\Psi = -4\pi Ga^2 \left[\rho\Delta + \frac{\beta^2\rho_c a^2}{k^2 + m^2a^2}\rho_c\Delta_c + 3(\rho + p)\sigma \right]. \tag{A.6}$$

While not strictly relevant to `MGCAMB`, let us note that combining Eqs. (3.3) and (3.4) in the QSA limit, we obtain the second order differential equation for δ_c:

$$\ddot{\delta}_c + \mathcal{H}\dot{\delta}_c = -k^2\left[\Psi + \beta\delta\phi\right] \tag{A.7}$$

which has the additional term on the right hand side, due to the fifth force mediated by the scalar field. The same equation for the baryons is

$$\ddot{\delta}_b + \mathcal{H}\dot{\delta}_b = -k^2\Psi , \tag{A.8}$$

where we have omitted the baryon-photon coupling effect for the convenience of discussion. Hence, the total matter density contrast, $\delta = (\rho_c\delta_c + \rho_b\delta_b)/(\rho_c + \rho_b)$, obeys

$$\ddot{\delta} + \mathcal{H}\dot{\delta} = 4\pi Ga^2\left(1 + \frac{2\tilde{\beta}^2k^2}{k^2 + m^2a^2}\frac{\rho_c^2\delta_c}{\rho^2\delta}\right), \tag{A.9}$$

where we have used Eq. (A.5) to replace $\delta\phi$. This allows us to identify the effective gravitational coupling as

$$G_{\text{eff}} = G\left(1 + \frac{2\tilde{\beta}^2k^2}{k^2 + m^2a^2}\frac{\rho_c^2\delta_c}{\rho^2\delta}\right) , \tag{A.10}$$

which is very similar to the G_{eff} on obtains from scalar-tensor theories with a universal coupling to matter,

$$G_{\text{eff}} = G\left(1 + \frac{2\tilde{\beta}^2k^2}{k^2 + m^2a^2}\right) , \tag{A.11}$$

making it challenging to distinguish between the two cases observationally [121].

Appendix B

The synchronous gauge implementation of Einstein equations in the CDM-only coupled scalar field models

While the contribution from the scalar field density perturbation to the Poisson equation (A.9) is negligible for the QSA-compatible models that we study, for completeness, we show their implementation in `MGCAMB`, which uses the synchronous gauge. Let us introduce

$$C_\phi \equiv \frac{\beta^2 \rho_c a^2}{k^2 + m^2 a^2}, \tag{B.1}$$

and write

$$-\frac{k^2 \Psi}{4\pi G a^2} = \rho\Delta + C_\phi \rho_c \Delta_c + 3(\rho + p)\sigma, \tag{B.2}$$

$$\frac{k^2(\Phi - \Psi)}{4\pi G a^2} = 3(\rho + p)\sigma , \tag{B.3}$$

where $\rho\Delta = \rho\delta + 3\mathcal{H}(\rho + p)\theta/k^2$ includes all species, including photons and neutrinos. Our goal is to derive the quantity $\mathcal{Z} = \dot{h}/(2k)$ appearing in `CAMB`. Applying the transformation between the two gauges [86],

$$\Psi = \dot{\alpha} + \mathcal{H}\alpha, \tag{B.4}$$

$$\Phi = \eta - \mathcal{H}\alpha, \tag{B.5}$$

where $\alpha = (\dot{h} + 6\dot{\eta})/2k^2$, to (B.2) and (B.3), allows us to write

$$\dot{\alpha} = -\eta - \frac{a^2}{2k^2}\left[2\rho\Delta + C_\phi\rho_c\Delta_c + 3\rho\left(1+w\right)\sigma\right], \tag{B.6}$$

$$\alpha = \frac{1}{H}\left\{\eta + \frac{a^2}{2k^2}\left[\rho\Delta + C_\phi\rho_c\Delta_c\right]\right\}. \tag{B.7}$$

We can rewrite (B.7) as

$$\eta = \mathcal{H}\alpha - \frac{a^2}{2k^2}[\rho\Delta + C_\phi\rho_c\Delta_c] = \mathcal{H}\alpha - \frac{a^2}{2k^2}\Gamma, \tag{B.8}$$

where $\Gamma = \rho\Delta + C_\phi\rho_c\Delta_c$. We can also combine (B.6) and (B.7) to obtain

$$\dot{\alpha} = -\mathcal{H}\alpha - \frac{a^2}{2k^2}\left[\Gamma + 3\rho\left(1+w\right)\sigma\right]. \tag{B.9}$$

Taking the derivative of (B.8), we obtain

$$\dot{\eta} = \dot{\mathcal{H}}\alpha + \mathcal{H}\dot{\alpha} - \frac{a^2}{2k^2}\dot{\Gamma} - \frac{a^2}{k^2}\mathcal{H}\Gamma. \tag{B.10}$$

In order to calculate $\dot{\Gamma}$, we need to know $(\dot{\rho\Delta})$. For standard matter, the conservation equations are

$$\dot{\delta} = -(1+w)\left(\theta + \frac{\dot{h}}{2}\right) - 3\mathcal{H}\left(\frac{\delta p}{\delta\rho} - w\right)\delta, \tag{B.11}$$

$$\dot{\theta} = -\mathcal{H}(1-3w)\theta - \frac{\dot{w}}{1+w}\theta + \frac{\delta p/\delta\rho}{1+w}k^2\delta - k^2\sigma. \tag{B.12}$$

From this, we can write

$$(\dot{\rho\Delta}) = -3\mathcal{H}\rho\Delta - (1+w)\rho\theta\left[1 + \frac{3}{k^2}(\mathcal{H}^2 - \dot{\mathcal{H}})\right]$$
$$- 3\mathcal{H}\rho(1+w)\sigma - (1+w)\rho\left(k^2\alpha - 3\dot{\eta}\right). \tag{B.13}$$

For dark matter, the conservation equations are given by (3.8) and (3.9), from which we find

$$(\dot{\rho_c\Delta_c}) = -3\mathcal{H}\rho_c\Delta_c - \rho_c\theta_c\left[1 + \frac{3}{k^2}\left(\mathcal{H}^2 - \dot{\mathcal{H}}\right)\right]$$
$$- \rho_c\left(k^2\alpha - 3\dot{\eta}\right) - (\beta\dot{\beta} + 3\mathcal{H}\beta^2)\frac{\rho_c^2(\delta_c - 3\alpha\mathcal{H})}{(k^2 + a^2m^2)}, \tag{B.14}$$

where we have used $w = 0$ and $\sigma = 0$ for CDM. We also have

$$\dot{\Gamma} = (\dot{\rho\Delta}) + C_\phi(\dot{\rho_c\Delta_c}) + \dot{C}_\phi\rho_c\Delta_c. \tag{B.15}$$

Using Eqs. (B.13) and (B.14) in (B.15), we have

$$
\begin{aligned}
\dot{\Gamma} = {} & -3\mathcal{H}\rho\Delta - \rho\theta(1+w)\left[1 + \frac{3}{k^2}\left(\mathcal{H}^2 - \dot{\mathcal{H}}\right)\right] \\
& - \rho(1+w)\left(k^2\alpha - 3\dot{\eta}\right) - 3\mathcal{H}\rho\left(1+w\right)\sigma \\
& + C_\phi\bigg\{ -3H\rho_c\Delta_c - \rho_c\theta_c\left[1 + \frac{3}{k^2}\left(\mathcal{H}^2 - \dot{\mathcal{H}}\right)\right] \\
& - \rho_c\left(k^2\alpha - 3\dot{\eta}\right) - (\beta\dot{\beta} + 3\mathcal{H}\beta^2)\frac{\rho_c^2(\delta_c - 3\alpha\mathcal{H})}{(k^2 + a^2m^2)}\bigg\} \\
& + \dot{C}_\phi\rho_c\Delta_c \; .
\end{aligned}
\tag{B.16}
$$

We then substitute Γ and $\dot{\Gamma}$ into the equation for $\dot{\eta}$, and solve for $\dot{\eta}$, to find

$$
\begin{aligned}
\dot{\eta} = {} & \frac{1}{2}\frac{a^2}{k^2 + \frac{3}{2}a^2[\rho(1+w) + C_\phi\rho_c]} \\
& \bigg\{ k\rho q\left[1 + \frac{3(\mathcal{H}^2 - \dot{\mathcal{H}})}{k^2}\right] \\
& - \rho_c\Delta_c\dot{C}_\phi + k^2\alpha\Big[C_\phi\rho_c - \rho_{\rm DE}\left(1 + w_{\rm DE}\right)\Big] \\
& + (1 + C_\phi)(\beta\dot{\beta} + 3\mathcal{H}\beta^2)\frac{\rho_c^2(\delta_c - 3\alpha\mathcal{H})}{k^2/a^2 + m^2}\bigg\} \; ,
\end{aligned}
\tag{B.17}
$$

with $kq = (1+w)\theta$. Finally, we can obtain $\mathcal{Z}$ used in the code from

$$
\mathcal{Z} = k\alpha - 3\frac{\dot{\eta}}{k} \; .
\tag{B.18}
$$

Appendix C

Generalized Brans-Dicke and coupled quintessence scenarios

Below we provide the relevant equations in the GBD and CQ models, following the notations and conventions of Ref. [121]. In particular, we work in the baryon frame, *i.e.* the frame where Standard Model (SM) particles follow the geodesics of the metric. The action for the GBD model is given by

$$S^{\text{GBD}} = \int d^4 \sqrt{-g} \left[\frac{A^{-2}(\phi)}{16\pi G} R - \frac{1}{2} \partial_\mu \phi \, \partial^\mu \phi - V(\phi) \right.$$
$$\left. + \mathcal{L}_{\text{m}}(\psi_{\text{CDM}}, \psi_{\text{SM}}, g_{\mu\nu}) \right],$$

where G is the Newton constant, g is the determinant of the baryon frame metric $g_{\mu\nu}$ and R is the associated Ricci scalar. The scalar field is denoted with ϕ, V is its potential and A is a generic function of ϕ. The contributions of SM and CDM particles, denoted by ψ_{SM} and ψ_{CDM} respectively, are included in the matter Lagrangian density $\mathcal{L}_{\text{m}}$. The scalar field is conformally coupled to all matter, such that also CDM follows the geodesics of the baryon frame metric $g_{\mu\nu}$.

On the other hand, in the CQ scenario, the scalar field is conformally coupled to CDM only. In the baryon frame, the action is given by

$$S^{\text{CQ}} = \int d^4 \sqrt{-g} \left[\frac{1}{16\pi G} R - \frac{1}{2} \partial_\mu \phi \, \partial^\mu \phi - V(\phi) \right.$$
$$\left. + \mathcal{L}_{\text{SM}}(\psi_{\text{SM}}, g_{\mu\nu}) + \mathcal{L}_{\text{CDM}}(\psi_{\text{CDM}}, A^2(\phi) g_{\mu\nu}) \right],$$

where the gravitational part of the action is not modified and CDM particles follow geodesics of $A^2(\phi) g_{\mu\nu}$.

We adopt the line element in Eq. (4.1) and work under the quasi-static approximation, neglecting time derivatives of the metric and the field perturbations over spatial ones [122].

For GBD, this leads to the following sets of equations in Fourier space on sub-horizon scales:

$$k^2\Phi = -4\pi Ga^2\left(\rho_b\delta_b + \rho_c\delta_c\right) - \beta_1 k^2\delta\phi, \tag{C.1}$$

$$k^2(\Phi - \Psi) = -2\beta_1 k^2\delta\phi, \tag{C.2}$$

$$\dot\delta_b + \theta_b = 0, \tag{C.3}$$

$$\dot\theta_b + \mathcal{H}\theta_b = k^2\Psi, \tag{C.4}$$

$$\dot\delta_c + \theta_c = 0, \tag{C.5}$$

$$\dot\theta_c + \mathcal{H}\theta_c = k^2\Psi, \tag{C.6}$$

$$\delta\phi = -\frac{\beta_1(\rho_c\delta_c + \rho_b\delta_b)}{m^2 + k^2/a^2}, \tag{C.7}$$

$$\Box\phi = V_{,\phi} + \beta_1(\rho_c + \rho_b) \equiv V^{\mathrm{eff}}{}_{,\phi}, \tag{C.8}$$

$$\ddot\delta + \mathcal{H}\dot\delta = 4\pi Ga^2\rho\delta\left[1 + \frac{2\tilde\beta_1^2 k^2}{a^2 m_1^2 + k^2}\right]. \tag{C.9}$$

Here, $\Box \equiv \nabla^\mu\nabla_\mu$, the scalar field coupling strength is given by $\beta_1 = A_{,\phi}/A$, where a comma indicates a derivative, and we have defined $\tilde\beta_1 \equiv \beta_1/\sqrt{8\pi G}$.

For CQ, the analogous set of equations is

$$k^2\Phi = -4\pi Ga^2\left(\rho_b\delta_b + \rho_c\delta_c\right), \tag{C.10}$$

$$k^2(\Phi - \Psi) = 0, \tag{C.11}$$

$$\dot\delta_b + \theta_b = 0, \tag{C.12}$$

$$\dot\theta_b + \mathcal{H}\theta_b = k^2\Psi, \tag{C.13}$$

$$\dot\delta_c + \theta_c = 0, \tag{C.14}$$

$$\dot\theta_c + (\mathcal{H} + \beta_2\dot\phi)\theta_c = k^2\Psi + k^2\beta_2\delta\phi, \tag{C.15}$$

$$\delta\phi = -\frac{\beta_2\rho_c\delta_c}{m_2^2 + k^2/a^2}, \tag{C.16}$$

$$\Box\phi = V_{,\phi} + \beta_2\rho_c \equiv V^{\mathrm{eff}}{}_{,\phi}, \tag{C.17}$$

$$\ddot\delta + \mathcal{H}\dot\delta = 4\pi Ga^2\rho\delta\left[1 + \frac{2\tilde\beta_2^2 k^2}{a^2 m^2 + k^2}\left(\frac{\rho_c}{\rho}\right)^2\left(\frac{\delta_c}{\delta}\right)\right], \tag{C.18}$$

where $\tilde\beta_2$ is defined in the same way as $\tilde\beta_1$. The effective potential V^{eff} is defined via Eqs. (C.8) and (C.17) for the two scenarios and related to the scalar field mass via $m^2 = V^{\mathrm{eff}}_{,\phi\phi}$.

Following Ref. [164], we assume $A^{-2} \approx 1$, with no impact on the arguments presented in our analysis. For GBD, this implies that the Newton constant G appearing in the equations always corresponds to the present-time value, which is a robust assumption since the redshift evolution of the gravitational coupling is constrained to be very small in screened GBD theories [182]. In the case of CQ, allowing for $A^{-2} \neq 1$ simply corresponds to a rescaling of the coupling β_2.

Appendix D

Galaxy clustering survey specifications

We adopt the SKA2 specifications from Ref. [144], assuming measurements of the clustering correlation function multipoles in 15 spectroscopic redshift bins centered at $z = 0.15, 0.25, \ldots, 1.55$, each with width $\Delta z = 0.1$. In each bin, we evaluate the multipoles at 35 separations from $d = 20\,h^{-1}\mathrm{Mpc}$ to $d = 160\,h^{-1}\mathrm{Mpc}$ in increments of $4\,h^{-1}\mathrm{Mpc}$.

We model the galaxy bias according to the fitting function from Ref. [144],

$$b_{\mathrm{P}}(z) = b_{\mathrm{P},1} \exp(b_{\mathrm{P},2} z) \pm \Delta b/2, \qquad\qquad (\mathrm{D.1})$$

where P indicates the bright (B) or faint (F) galaxy population. We let the parameters $b_{\mathrm{P},1}$ and $b_{\mathrm{P},2}$ free with fiducial values 0.554 and 0.873, respectively, and we set $\Delta b = 1$ in agreement with the bias difference measured in Ref. [153].

For the purpose of our forecasts, we fix the magnification bias according to Appendix B in Ref. [145] and set the evolution bias to 0. Both quantities will be directly measurable from the average number of galaxies once the data become available.

Appendix E

Constraints in polar coordinates

An alternative visualization of the constraints can be achieved by performing a change to polar coordinates,

$$R = \sqrt{\beta_{*1}^2 + \beta_{*2}^2} \,, \qquad \theta = \frac{\beta_{*2}}{R} \,. \tag{E.1}$$

We show in Fig. E.1 the 1σ confidence regions on R, θ for the same CQ fiducial model as in Fig. 4.1, *i.e.* with $\beta_{*2} = 1$, $\lambda_* = 10$ Mpc. For simplicity, these constraints were obtained by fixing all cosmological parameters to their fiducial values.
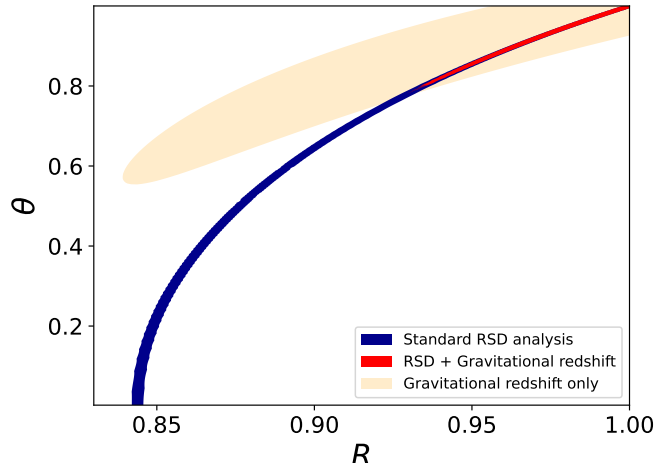

Figure E.1: The 1σ and confidence regions on the polar coordinates R and θ. Here, the fiducial model is CQ and is specified by $\beta_{*2} = 1$ and $\lambda_* = 10$ Mpc (with $\beta_{*1} = 0$).